

AN ABSTRACT OF THE DISSERTATION OF

Michael Raymond Dragowsky for the degree of Doctor of Philosophy in Physics
presented on 28 June 1999. Title: Sudbury Neutrino Observatory Energy
Calibration using Gamma-Ray Sources.

Redacted for privacy

Abstract approved: _____

Kenneth S. Krane

Redacted for privacy

Eric B. Norman

The long-standing Solar Neutrino Problem describes the disagreement between the observed and predicted solar neutrino flux. An extension to the electroweak model of particle physics predicts that neutrino flavor may change as a neutrino propagates from its source, and may account for the Solar Neutrino Problem. The Sudbury Neutrino Observatory will make two measurements of the ^8B neutrino flux from the Sun. The first is independent of neutrino flavor, allowing for the first time a definitive measurement of the total ^8B neutrino flux. The second measurement will be sensitive only to the ^8B electron-neutrino flux. Comparison of these two measurements will allow a determination of whether the electron-neutrinos produced in the Sun change their flavor as they propagate to the Earth. Precise energy calibration is required to ensure accurate measurements. Two energy calibration sources will be described that rely on the coincident emission of a β particle and a γ -ray. The sources make use of ^{16}N and ^{24}Na β -decay. In addition to energy calibration, the ^{24}Na source provides an assessment of the rate of photodissociation of deuterium that is important in understanding backgrounds for both solar neutrino measurements.

Sudbury Neutrino Observatory Energy Calibration
using Gamma-Ray Sources

by

Michael Raymond Dragowsky

A DISSERTATION

submitted to

Oregon State University

in partial fulfillment of
the requirements for the
degree of

Doctor of Philosophy

Presented 28 June 1999
Commencement June 2000

Doctor of Philosophy DISSERTATION of Michael Raymond Dragowsky presented
on 28 June 1999

APPROVED:

Redacted for privacy

Co-Major Professor, representing Physics

Redacted for privacy

Co-Major Professor, representing Physics

Redacted for privacy

Head of Department of Physics

Redacted for privacy

Dean of Graduate School

I understand that my dissertation will become part of the permanent collection of Oregon State University libraries. My signature below authorizes release of my dissertation to any reader upon request.

Redacted for privacy

Michael Raymond Dragowsky, Author

Acknowledgement

There are people in my life whom I could not do without. I thank my wife, Susan Booth, and our daughter, Sophie Louise Booth Dragowsky, for sharing their lives with me. Without Susan's encouragement and the motivation to provide for Sophia I would undoubtedly still be outlining this work, rather than completing it. I thank my parents, Raymond and Patricia, for their love and support, and my brother, David, for being my brother. I thank Vanessa and Chris Vostmyer, Ida Caskey, Doris Reddekopp and Laurel Holland for their faith and goodwill. I treasure my life-long friendships with Mike Hilton, Robert Reed, Chris Hamilton and Craig Griffis.

I thank Ken Krane for inviting me to return to graduate school and for his guidance and encouragement of my interest in nuclear astrophysics. The final year of my work was performed in Corvallis and Ken has made my transformation from student to colleague nearly painless and very rewarding. Ken taught the first physics course that I attended at OSU during Spring quarter 1989. He has seen me through a decade-long study of physics and I will always appreciate his efforts to keep me moving forward.

I thank the members of my committee for serving and also for taking an interest in me personally. Corinne Manogue has been an inspirational and steadying influence throughout our ten-year acquaintance and friendship. Phil Siemens, Dave Griffiths and Burt Fein have my respect and appreciation for their interest in my project, even as the scope of that project diminished over the course of my studies. And a final thank you to Glenn Evans, who was willing to join the committee at short notice.

I gratefully acknowledge the opportunity to participate in the experiment being conducted by the Sudbury Neutrino Observatory collaboration. In particular, I thank Rick Norman and Kevin Lesko for inviting me to join the effort at LBNL in support of SNO and providing a home away from home. Thanks to Yuen-dat Chan for sharing the ^{16}N source and his lunch pail. Special thanks to Anett Schülke for discussing her perceptions of SNO and its people, and for sharing her daughter, Sadia, and her

experiences in the DDR. Thanks to Colin Okada and Alan Poon for asking the right question and whom I will never confuse in name nor deed. To Yoichi Kajiyama who left his mark on the hardware and on my conscious as a result of many discussions not limited to physics and engineering. To Maria Isaac for help and understanding. To Ruth-Mary Larimer for her inexhaustable enthusiasm and knowledge of how to get things done at the 88. To Xin Chen and Bob Stokstad for their interest in this work. To Al Smith and Dick McDonald who gracefully shared their expertise and time. And to those who made me feel welcome during my stay at the Institute for Nuclear and Particle Astrophysics: Brian Fujikawa, Tim Culler, Susana Deustua, Hannah Pena, Jeanne Miller and Lisa Hammond.

Without the assistance of Graham Sillman, Hardy Siefert and the INCO Creighton Mine rescue squad this work would be lying in a muddy drift 6800 feet beneath the Earth's surface. My profound thanks go to those who helped me in my hours of need. To Art McDonald, thanks for calming my nerves prior to surgery. To Graham, Hardy, Chuck, Ilan, David, James, André, Yuen-dat and Chris for visiting during a very long week. And to Dr. Mitra, for placing more stainless steel in my body that I would ever have thought reasonable.

I am pleased to single out Lee Bernstein for his friendship and unflinching encouragement. I also appreciate those who encouraged my devotion to this field through their example as people as well as physicists: Bradley Matson, Robin Zagone, Shane and Michelle Larson, Richard Young, John Wood, Janet Tate and Allan Wasserman.

We must all eventually choose our own destiny. My choices have seldom been guided by the existence of a specific long-term goal and so the pursuit of a physics doctorate has been an unusual experience. The detailed steps to reach the goal were not clear to me when I began my studies. I was fortunate to find that I enjoyed the process. I do regret that I was unable to share my pleasure and joy for having finally found a pursuit that suited me with Keith.

Table of Contents

Page

1	The Solar Neutrino Problem	1
1.1	The Neutrino	1
1.2	Solar Neutrinos	4
1.2.1	The pp Chain	5
1.2.2	The CNO Cycle	6
1.3	Solar Neutrino Observation	7
1.3.1	Radiochemical Detectors	7
1.3.2	Čerenkov Detectors	12
1.4	Statement of the Solar Neutrino Problem	15
2	Resolution of the Solar Neutrino Problem	17
2.1	The Solar Interior	17
2.1.1	Standard Solar Model Input	18
2.1.2	Helioseismology	19
2.2	Nuclear Reaction Rates	21
2.2.1	Laboratory Measurements	22
2.2.2	Screening	24
2.2.3	The ${}^7\text{Be}(p,\gamma){}^8\text{B}$ Reaction	24
2.2.4	The ${}^3\text{He}({}^3\text{He},2p){}^4\text{He}$ and ${}^3\text{He}({}^4\text{He},\gamma){}^7\text{Be}$ Reactions	26
2.2.5	${}^7\text{Be}$ Electron Capture	28
2.2.6	Standard Solar Models and Solar Neutrinos	29
2.3	Neutrino Oscillations	30
2.3.1	Oscillations in Vacuum	31
2.3.2	Atmospheric Neutrinos at Super-Kamiokande	34
2.3.3	Matter-Enhanced Oscillations	36
2.4	Prospects for Resolving the Solar Neutrino Problem	38

Table of Contents (Continued)

	<u>Page</u>
3 The Sudbury Neutrino Observatory	39
3.1 The Physical Structure of SNO	40
3.1.1 Heavy Water Containment: The Acrylic Vessel	41
3.1.2 PMT Support Structure	43
3.1.3 Photomultiplier Tubes	43
3.1.4 Water Handling Facilities	46
3.1.5 Electronics and Data Acquisition	48
3.2 Production and Detection of Čerenkov Light	49
3.2.1 PMT Response to Čerenkov Light	50
3.2.2 Optical Transmission Properties of SNO	51
3.3 Backgrounds	52
3.3.1 Cosmic Rays	53
3.3.2 Radioactive Contamination	54
3.4 SNO Weak Interactions	57
3.4.1 Neutral-Current Detection	57
3.4.2 Charged-Current Detection	59
3.4.3 Elastic Scattering in SNO	60
3.4.4 Interpretation	61
3.5 Response of SNO to Solar Neutrinos	61
3.5.1 SNO Monte Carlo Simulation and Analysis	62
3.5.2 SNOMAN Simulated Response	63
3.5.3 Sensitivity to Oscillation Parameters	66
3.6 Energy Calibration	67
3.6.1 Energy Calibration Sources	68
3.6.2 Triggering and Signal Development	70
3.7 Summary	72
4 ^{16}N Energy Calibration Source	73
4.1 ^{16}N Production	73

Table of Contents (Continued)

	<u>Page</u>
4.2 ^{16}N Source Chamber Design	74
4.3 ^{16}N Source Chamber Operation	76
4.4 Experimental Results for γ -ray Attenuation	79
4.4.1 ^{54}Mn Results	80
4.4.2 $^9\text{Be}(\alpha, n)^{12}\text{C}$ Results	80
4.5 Simulation Results for γ -ray Attenuation	82
4.5.1 Stainless Steel Effect on γ -rays	82
4.5.2 Energy Deposition in D_2O	84
4.6 Beta Interactions in the Source Chamber	86
4.6.1 Direct Čerenkov Light Production	86
4.6.2 The 10.4-MeV β decay branch	87
4.6.3 Bremsstrahlung from the 4.3-MeV β Decay Branch	89
4.7 Spectrum of Phototube Hits	91
4.7.1 Nhit Spectrum Variation by Source Location	91
4.7.2 Geometric Anisotropy	93
4.7.3 Gamma Ray Emission Isotropy	96
4.8 Trigger Efficiency and Yield	98
4.9 Run Plan	100
4.10 Conclusions	102
5 Systematic Uncertainty of ^{16}N Energy Calibration	103
5.1 Unattenuated γ -rays	103
5.1.1 ^{17}N Neutron Source	104
5.1.2 ^{17}N Neutron-Capture γ -rays	105
5.1.3 Gamma Ray Peak Shape	109
5.1.4 Fitting ^{16}N Nhit Spectrum	110
5.1.5 Analysis Considerations	112

Table of Contents (Continued)

	<u>Page</u>
5.2 The 6.13- and 7.12-MeV γ -ray Relative Intensity	115
5.2.1 Experiment	115
5.2.2 Analysis	116
5.2.3 Results	122
5.3 Summary	123
6 Low Energy Calibration of SNO with ^{24}Na	124
6.1 Investigation of ^{24}Na in NaI	125
6.1.1 Theory	125
6.1.2 Procedure	127
6.1.3 Analysis	128
6.1.4 Additional considerations	131
6.2 Simulation of SNO Response to ^{24}Na Calibration	134
6.2.1 Calibration Source	134
6.2.2 Simulation Scheme	134
6.2.3 Simulation Results	135
6.3 Assessment	140
6.4 The ^{24}Na Source	141
6.4.1 NaI(Tl) Detector	141
6.4.2 D_2O Container	142
6.5 Source Preparation	143
6.6 Calibration Procedure	144
7 SNO Detector Commissioning	146
7.1 Air Fill	146
7.2 Anomalous PMT Performance	148
7.2.1 Flasher Analysis	148
7.2.2 Multiple Flasher Candidates	151
7.2.3 Blind Flashers	152

Table of Contents (Continued)

	<u>Page</u>
7.3 Backgrounds	153
7.4 Energy Scale	153
7.4.1 Calibration Measurement using ^{16}N in Air	154
7.4.2 γ -rays in the SNO Cavity	155
7.5 Water Fill	156
7.5.1 PGT Spectrum	157
7.5.2 Preliminary ^{16}N Energy Calibration	158
7.5.3 Comparison with Monte Carlo	160
7.6 Summary	161
8 Conclusions	162
Bibliography	164
Appendix: The Description of the ^{16}N and NaI Sources in SNOMAN	171
A.1 The ^{16}N Source Chamber Geometry	172
A.2 Verification of the Geometry	175
A.3 ^{24}Na Source Geometry	176

List of Figures

<u>Figure</u>	<u>Page</u>
1.1 Solar fusion proton-proton chain.	5
1.2 Solar fusion CNO cycle.	6
1.3 Data from the ^{37}Cl experiment. The average rate is well below the value predicted by Standard Solar Models.	9
1.4 Production rate of ^{71}Ge for each run conducted by the Gallex solar neutrino experiment. The mean rate appears at the end of each operating period.	11
1.5 Solar neutrino elastic scattering event direction relative to Sun. Peak at $\cos \theta_{\text{sun}}=1$ shows that these neutrinos come from the Sun.	13
1.6 Left: Electron energy spectrum from Super-Kamiokande. Points with error bars denote data. Solid histogram denotes Monte Carlo prediction. Right: Ratio of observed electron energy spectrum and expectation from the SSM. Data are from the first 504 days at Super-Kamiokande. Note that all events above 14 MeV are combined in the highest bin.	15
2.1 The δm^2 - $\sin^2(2\theta)$ parameter space. The region excluded by the NOMAD $\nu_\mu\nu_\tau$ appearance experiment (solid line) compared with exclusion results from previous experiments. The plot illustrates that incremental improvements in sensitivity may occur in either δm^2 , $\sin^2(2\theta)$ or both parameters simultaneously.	33
2.2 The δm^2 - $\sin^2(2\theta)$ parameter space for atmospheric neutrinos at Super-Kamiokande. The analysis fixes values for δm^2 and $\sin^2(2\theta)$ due to the suppression of the detector signal compared to Monte Carlo expectations. The result is compared to earlier analysis from the much smaller Kamiokande detector.	35
3.1 Diagram depicting the underground laboratory location within the Creighton mine. The shielding by 6800 feet of material reduces the cosmic ray induced muon flux to 100 per day.	41
3.2 Artists depiction of the detector cavity.	44
3.3 The SNO PMT reflector and hexagonal cell panels. Left: PMT reflector front view (top) and profile (bottom). Right: Panels composed of hexagonal reflector cells and their location on the PSUP.	46

List of Figures (Continued)

<u>Figure</u>	<u>Page</u>
3.4 The net γ -ray energy spectrum observed in the SNO cavity at the 6800-foot level and in the laboratory at the 4600-foot level.	55
3.5 The SNO weak neutral-current interaction on deuterium represented as a Feynman diagram.	57
3.6 The SNO charged-current weak interaction on deuterium.	59
3.7 Elastic scattering between electrons and neutrinos features neutral- and charged-current interactions for ν_e , and only neutral-current interactions for ν_μ and ν_τ	60
3.8 Simulated SNO response to 100,000 8-MeV electrons. Left: All events originate from the center of the D ₂ O volume. Right: Events originate uniformly throughout the D ₂ O volume.	64
3.9 Simulated SNO response to 10,000 charged-current interactions.	64
3.10 Simulated SNO response to 30,000 neutral-current interactions in D ₂ O and 2.5 metric tons MgCl ₂ in D ₂ O. The Nhit spectra appear in the top panel, while the radial distance where the neutron capture occurred is plotted separately below.	65
3.11 Simulated SNO response to charged-current spectrum for selected neutrino oscillation mechanisms and parameters (see Table 3.4).	66
3.12 Simulated SNO response to electrons and γ -rays in the energy range 2-14 MeV.	68
4.1 A schematic representation of the source chamber.	75
4.2 Major ¹⁶ N β decay branches. The γ -ray energies appear to the right of the energy levels. The β decay branch strengths are shown as percentages near the arrow depicting the transition.	77
4.3 Data for the attenuation of 4.4-MeV γ -rays from ⁹ Be(α ,n) ¹² C by the steel used for the outer container of the ¹⁶ N chamber. Top panel: Data and Background spectra without attenuation. Lower panels: Background subtracted spectra showing data without attenuation (left) and with attenuation (right).	81
4.4 The Nhit spectra due to the γ -rays of ¹⁶ N are shown in two cases. The solid line is with the full source chamber geometry. The dashed line spectra results from replacing the steel of the source chamber by D ₂ O.	84

List of Figures (Continued)

<u>Figure</u>	<u>Page</u>
4.5 The Nhit spectra due to 6.13-MeV monoenergetic γ -rays are shown in two cases. The solid line depicts the spectrum seen after replacing the media of the full source chamber geometry with D ₂ O. The dashed line spectra depicts the standard media of the source chamber geometry. .	85
4.6 Comparison of ¹⁶ N simulation featuring the full decay scheme and a simulation featuring only the β particles of the ¹⁶ N decay scheme. . .	87
4.7 The Nhit spectrum due to only the 10.4-MeV β decay branch of ¹⁶ N.	88
4.8 The top two panels feature a comparison of simulated Nhit spectra when (left) only 6.1-MeV γ -rays and (right) a 4.3-MeV β -spectrum in coincidence with 6.1-MeV γ -rays are generated within the ¹⁶ N chamber. The lower panel shows the result of dividing the $\beta + \gamma$ spectrum by the γ only spectrum.	90
4.9 Nhit spectrum from 10000 ¹⁶ N decays. An asymmetric range is used to fit the main feature to a Gaussian distribution, which is represented by the solid line.	92
4.10 Oppositely directed γ -ray beams were simulated to illustrate the effect of geometric anisotropy on Nhit spectra. The simulation parameters appear on the left. The Nhit spectra appear on the right.	94
4.11 The variation of Nhit with respect to displacement along the major axes of SNO. The +X axis points between two belly plates, while the +Y axis points directly at a belly plate.	95
4.12 The incident angle at the PMT face is plotted for several different displacements of the ¹⁶ N chamber along the axis defined by ¹⁶ N chamber position and the center of the PSUP.	96
4.13 Polar angle distributions resulting from 6.129-MeV γ -ray events. The Monte Carlo generation angle is plotted for simulations with and without the source chamber.	98
4.14 The γ -ray isotropy represented as a fractional deviation from the available solid angle. Results from simulations with and without the source chamber are depicted.	99
4.15 The ¹⁶ N source chamber calibration positions, based on a 1×1 meter grid. The dashed line indicates the source manipulator limit.	101

List of Figures (Continued)

<u>Figure</u>	<u>Page</u>
5.1 The total and capture cross-sections for neutrons by deuterium below 20 MeV.	106
5.2 The neutron-capture cross-sections are presented for deuterium (^2H), ^{16}O and ^{17}O below 20 MeV. All plots represent n,γ cross-sections, except for n,α on ^{17}O , that is designated with stars.	108
5.3 The results of a fit to the monoenergetic, unattenuated γ -ray from neutron-capture on deuterium, showing the number of events plotted against Nhit. Channels 30 and above are included in the fits, shown in the left panel. The corrected function is then plotted over the full Nhit range along with the data in the right panel.	110
5.4 The ^{16}N Nhit spectrum (solid line) decomposed for contributions from full energy 6.1- and 7.1-MeV γ -rays, and from γ -rays and β -particles that interact in the source chamber.	111
5.5 The ^{16}N Nhit spectrum corrected for γ -rays scattered by the source chamber. The fit is to two Gaussian distributions.	112
5.6 The simulated radial distribution of Čerenkov light vertices from ^{16}N and ^{17}N in pure D_2O . The source chamber is not present in the ^{17}N simulation.	113
5.7 The Ge detector efficiency relative to the 2598 keV γ -ray, as determined from the ^{56}Co and ^{16}N water cell sources.	119
5.8 Top panel: Relative efficiency as a function of energy from ^{56}Co data and GEANT simulation. Botton panel: Percent deviation of simulated efficiencies from data as a function of energy.	121
5.9 Percent deviation of simulated efficiency from data as a function of change of efficiency.	122
6.1 The decay scheme of ^{24}Na	126
6.2 Schematic of coincidence detection of ^{24}Na	126
6.3 Neutron activated NaI energy spectra. The peak at channel 112 is due to ^{40}K . Left panel: ^{241}Am - ^9Be neutrons thermalized by polyethylene beads. Right panel: ^{241}Am - ^9Be neutrons.	128
6.4 Spectrum of NaI Annulus in coincidence with Activated NaI detector.	129

List of Figures (Continued)

<u>Figure</u>	<u>Page</u>	
6.5	Escape peak spectra resulting from optimized gating. Channel number is displayed on the abscissa.	131
6.6	Comparison of spectra of NaI Annulus for gates of decreasing width. The designations GS*G# denote vector identifiers for the displayed spectra within PAW. Channel number is displayed on the abscissa. . .	132
6.7	Spectra resulting from SNOMAN simulation of 4"×4" NaI crystal. Energy cuts have been used to produce the three spectra which appear with dashed lines.	135
6.8	Individual spectra resulting from SNOMAN simulation of 4"×4" NaI crystal.	136
6.9	Simulated SNO response to four sizes of NaI crystal. The spectra appearing in each plot are the result of energy cuts on the activated NaI spectrum. As crystal size increases, the SNO response to the individual γ -rays grows.	137
6.10	Simulated SNO response to 3"×6" cylindrical NaI crystal.	138
6.11	Schematic drawing for the NaI(Tl) source D ₂ O cannister.	142
7.1	Nhit spectra resulting from Nhit, ESUM and PGT triggers. Data from the Nhit trigger appear in the top panel, while data from all three triggers appear in the bottom panel in a logarithmic scale.	147
7.2	Anomalous event timing. The timing is relative to the PMT with maximum charge in the event.	149
7.3	Geometric time and position method to identify flasher events.	150
7.4	Flasher relative time and angle relations. The PMT cluster at 75 ns and $\cos \theta = -1$ represents light emitted from the high-charge PMT that traverses the detector. The cluster between 25 and 50 ns and near $\cos \theta = 1$ is light reflecting from the acrylic vessel. Angles are measured with respect to the center of the detector. $\cos \theta = 1$ represents the high-charge PMT.	151
7.5	Air fill ¹⁶ N calibration spectra. External asynchronous trigger is depicted by the solid line, while pulsed global trigger spectrum is shown as a dashed line.	155
7.6	Simulated Nhit spectrum due to cavity γ -rays.	156

List of Figures (Continued)

<u>Figure</u>	<u>Page</u>
7.7 The Nhit spectrum from the Pulsed Global Trigger (PGT). The trigger rate is 5 Hz and no other triggers are associated with these events. The fit to a Poisson distribution for 2 events is included.	158
7.8 The effectiveness of the ^{16}N triggered source is demonstrated. Čerenkov light production vertices are reconstructed from the data. Left: All events - the umbilical is clearly imaged. Right: Triggered events - only source chamber decays are imaged.	159
7.9 The Nhit spectra from May 1999 is compared to the results of Monte Carlo simulation.	160

List of Tables

<u>Table</u>	<u>Page</u>
1.1 The Electroweak Standard Model lepton families.	3
1.2 The solar neutrino producing reactions.	6
1.3 Total neutrino flux predicted by Standard Solar Models for the Home- stake chlorine experiment.	10
2.1 Gamow energies for selected solar fusion reactions. The central core temperature 16×10^6 K is assumed, providing upper bounds.	23
2.2 Average ${}^3\text{He}(\alpha, \gamma){}^7\text{Be}$ cross section results for capture γ -ray and activ- ity determination methods.	27
2.3 Solar neutrino fluxes predicted by standard solar models prior to (BU (1988)) and following (BP (1998)) extensions arising in part from he- lioismology.	30
2.4 Values of the parameter δm_{\min}^2 which characterises the sensitivity re- gions of different neutrino oscillation experiments.	34
3.1 Criteria for D_2O acceptance at SNO.	47
3.2 Particles with distinct masses, unit charge, and their Čerenkov light production threshold.	50
3.3 The solar neutrino interactions in SNO and their expected detection rate.	62
3.4 Neutrino oscillation mechanisms with specific parameters which cor- respond to spectra plotted in Figure 3.11. The MSW Nonadiabatic solution has been ruled out by data obtained since the plot was gener- ated.	67
3.5 Calibration sources and energies. The end point energy is provided as E_β . The signal from the ${}^8\text{Li}$ source is due to the β^- , and the trigger results from two α particles which result from ${}^8\text{Be}$ decay.	69
4.1 γ attenuation due to stainless steel for 10000 ${}^{16}\text{N}$ decays.	83
4.2 Attenuation with full ${}^{16}\text{N}$ chamber geometry for 10^5 6.13-MeV mon- oenergetic γ -rays.	86

List of Tables (Continued)

<u>Table</u>	<u>Page</u>
4.3 The 10.4-MeV β spectrum of ^{16}N was simulated with 10000 β particles in the ^{16}N chamber geometry. Attenuation is reported as number of events which exceed the Nhit threshold and as a percentage. The percent contribution to the ^{16}N Nhit spectrum is reported in the column entitled " ^{16}N Flux".	88
4.4 The 10.4-MeV β spectrum of ^{16}N was simulated with 100000 β particles in the ^{16}N chamber geometry. Four different wall thicknesses are investigated. Data is displayed as follows: The number of events exceeding the threshold, number of γ -rays emitted into the D_2O , number of β particles emitted into the D_2O and attenuation as a percentage of simulated events are shown for the 10 (20) Nhit threshold.	89
4.5 Results for ^{16}N simulation points throughout the SNO D_2O volume. The Nhit value appears to the left and the standard deviation σ appears to the right. Each simulation featured approximately 7,000 events. The uncertainty in Nhit is \pm	93
4.6 Statistical uncertainty per direction resulting from calibration for one hour per source point with 150 s^{-1} 6.1-MeV γ -rays.	101
5.1 The ^{17}N β -decay neutron branch intensities and energies.	104
5.2 The percentage of neutrons emitted into the D_2O that capture on the isotopes present in pure D_2O	108
5.3 Source characteristics of the ^{16}N runs.	116
5.4 ^{56}Co γ -ray energies and intensities (given as the percentage of decays in which the γ -ray is observed). The observed peak area and detector efficiency relative to 2.598 MeV is shown for the 7" geometry. The intensities are known with less than 0.3% uncertainty, with the exception of the 3.253-MeV γ -ray, that has 3% uncertainty.	118
5.5 The relative uncertainty of the 7.1- and 6.1-MeV γ -rays from ^{16}N β -decay resulting from the GEANT Ge detector efficiency Monte Carlo.	121
6.1 Selection criteria results for energy gates.	130
6.2 Summary of simulation data for sum of ^{24}Na γ -rays. The mean,FWHM, the number of events per 10^5 ^{24}Na decays and the range of energies (MeV) in the activated NaI energy gate are presented.	138

List of Tables (Continued)

<u>Table</u>		<u>Page</u>
6.3	Summary of simulation data for ^{24}Na γ_{2754} . The mean, FWHM, the number of events per 10^5 ^{24}Na decays and the range of energies (MeV) in the activated NaI energy gate are presented.	139
6.4	Summary of simulation data for ^{24}Na γ_{1368} . The mean, FWHM and the number of events per 10^5 ^{24}Na decays are presented. The energy range of the gate in the activated NaI detector is 2.8-4.1 MeV.	139

List of Appendix Figures

<u>Figure</u>	<u>Page</u>
A.1 The geometry regions of the ^{16}N source chamber.	174
A.2 The ^{16}N source chamber geometry, as illuminated by photon bombs from CAN, SCINT, RING and PMT_E. Each point represents an intersection of a photon propagation path and the boundary of a detector element. By setting all detector elements to air, SNOMAN propagates the photons in straight lines, but it keeps track of all boundary crossings. Plotting the boundary crossings provides a “photon map” of structures within SNO.	175

Sudbury Neutrino Observatory Energy Calibration using Gamma-Ray Sources

1. The Solar Neutrino Problem

1.1 *The Neutrino*

Energy and momentum conservation are well-established physical principles. The consideration of nuclear beta decay as a final state two-body problem during the early 1930's brought these principles into question. A continuous electron energy spectrum was observed, in contradiction with the discrete spectrum required for a two-body decay. The preservation of energy and momentum conservation required a three-body final state, else these conservation laws required modification when applied to the subatomic regime.

Pauli staunchly supported the conservation laws, and offered a three-body final state featuring a newly proposed spin- $\frac{1}{2}$, neutral particle, with “mass...the same order of magnitude as the electron...” [1]. This neutral particle was later named “neutrino” by Fermi. Additional examination of beta decay electron spectra led to the determination by Fermi [2] and Perrin [3] that the mass of the neutrino was consistent with zero. Fermi then turned to the formalism developed by Dirac and, in analogy with the electromagnetic interaction, used a vector interaction to describe beta decay under conditions when the initial nuclear spin equaled the final nuclear spin [4]. Gamow and Teller treated the problem with unequal nuclear spins, introducing the axial vector current [5]. The revelation in 1957 that parity was maximally violated in nuclear beta decay [6, 7] (and later in all weak interactions [8, 9, 10]) led to the present V-A beta decay formalism [11, 12], and ultimately the unification of electromagnetism and weak interactions (electroweak theory [13]). The continued success of these subsequent theoretical improvements provided additional support for a massless neutrino.

Experimental confirmation for neutrino existence was found by observing the inverse beta decay (Eq. 1.1).



A detailed and accessible account of the series of experiments performed by Reines and Cowan from 1953 to 1957 is found here [14, 15]. An informal discussion concerning neutrino physics appears in the July 1957 *Physics Today* [16]. Antineutrinos emitted from a nuclear reactor exposed the target to a high flux ($10^{13} \text{ cm}^{-2}\text{s}^{-1}$). The target was a tall, narrow (3 inches wide) water tank loaded with a cadmium compound, (selected for its high neutron capture cross section) CdCl_2 . Two tanks holding liquid scintillator were placed on either side of the water tank. An antineutrino interacted with a proton in the water, and the resulting positron annihilated with an electron in the tank, releasing back-to-back γ -rays, producing coincident light signals in the scintillator tanks. In addition, the neutron is moderated in the water and captures on cadmium, emitting 9.1 MeV of γ -ray energy in a cascade, in delayed coincidence with the positron signal. Additional experiments were conducted to ensure that no other signals in the detector produced such delayed coincidence signals. Reines was awarded the Nobel prize in 1996 for this work.

The existence of three neutrino families to correspond with the three charged lepton families (Table 1.1) was established through experiments at particle accelerator facilities in Europe and the United States. Standard electroweak theory maintains conservation laws for each family separately. Leptons are assigned the value +1, antileptons -1. Thus a muon may decay by Eq. 1.2, but not by Eq. 1.3

$$\mu^+ \rightarrow e^+ + \nu_e + \bar{\nu}_\mu \quad (1.2)$$

$$\mu^+ \rightarrow e^+ + \nu_e + \bar{\nu}_e \quad (1.3)$$

charged lepton	neutral lepton	charged antilepton	neutral antilepton
e^-	ν_e	e^+	$\bar{\nu}_e$
μ^-	ν_μ	μ^+	$\bar{\nu}_\mu$
τ^-	ν_τ	τ^+	$\bar{\nu}_\tau$

Table 1.1: The Electroweak Standard Model lepton families.

because in the former, muon lepton number (-1) and electron lepton number (0) are the same in initial and final states, while not for the latter (-1,0:0,-1).

The adoption of a massless neutrino in the standard electroweak model was based on the lack of compelling evidence to the contrary. The determination by Goldhaber [17] from ^{152}Eu beta decay that the neutrino has spin antialigned with momentum¹ is consistent with a massless particle. Tritium endpoint experiments have only been able to establish upper limits on the electron antineutrino mass in the range of 10 eV. Even these experimental results are viewed with caution because the measured values of mass squared have been uniformly negative (imaginary mass!) [18, 19]. Finally, the lowest limits (~ 15 eV) have been established from observing $\bar{\nu}_e$ emitted by supernova 1987a [20, 21]. The electron antineutrino rest mass has certainly been established as small, if not zero.

The ν_μ mass limit is derived from kinematic analysis on the following reaction featuring pions at rest.

$$\pi^+ \rightarrow \mu^+ + \nu_\mu \quad (1.4)$$

Applying energy and momentum conservation to the two particle final state leads to Eq. 1.5, which can be solved for m_{ν_μ} , as shown in Eq. 1.6.

$$m_\pi = \sqrt{p^2 + m_\mu^2} + \sqrt{p^2 + m_{\nu_\mu}^2} \quad (1.5)$$

¹Alignment (antialignment) of spin and momentum directions is termed helicity, and assigned the value +1 (-1).

$$m_{\nu_\mu}^2 = m_\pi^2 + m_\mu^2 - 2m_\pi\sqrt{p^2 + m_\mu^2} \quad (1.6)$$

The result is $m_{\nu_\mu}^2 = -0.016 \pm 0.023 \text{ MeV}^2$, which requires delicate handling [22] to determine the upper limit on m_{ν_μ} as 0.17 MeV.

The mass for ν_τ is not well determined by experiment. The kinematic analysis of tauon decays is difficult, due to many-particle final states and due to the rare nature of these events. The Large Electron Positron Collider (LEP) collaboration collected more than four years of data between 1991-95. Analysis resulted in 2939 events from reaction 1.7 and 52 from reaction 1.8 which provide the current upper limit of 18.2 MeV.

$$\tau^- \rightarrow 2\pi^- + \pi^+ + \nu_\tau \quad (1.7)$$

$$\tau^- \rightarrow \pi^+ + \pi^+ + \pi^- + \pi^- + \pi^- + \nu_\tau \quad (1.8)$$

Solar neutrino observations during the last decade have irreversibly altered the neutrino mass landscape.

1.2 Solar Neutrinos

The Sun's mass and size have long been the object of scientific inquiry. Techniques to determine these properties rely on measurements which may be performed with great accuracy: those of the orbital motion of the planets, and the Sun's apparent size [23]. Only in the last few decades has it been possible to receive answers to questions relating to conditions in the Sun's core. Two complementary techniques have emerged: solar neutrino observation, and solar acoustic wave observation, or helioseismology. The former is concerned with elements of the microphysics (nuclear reactions) in the core, while the latter provides evidence for the macroscopic properties (equation of state) as a function of radial position.

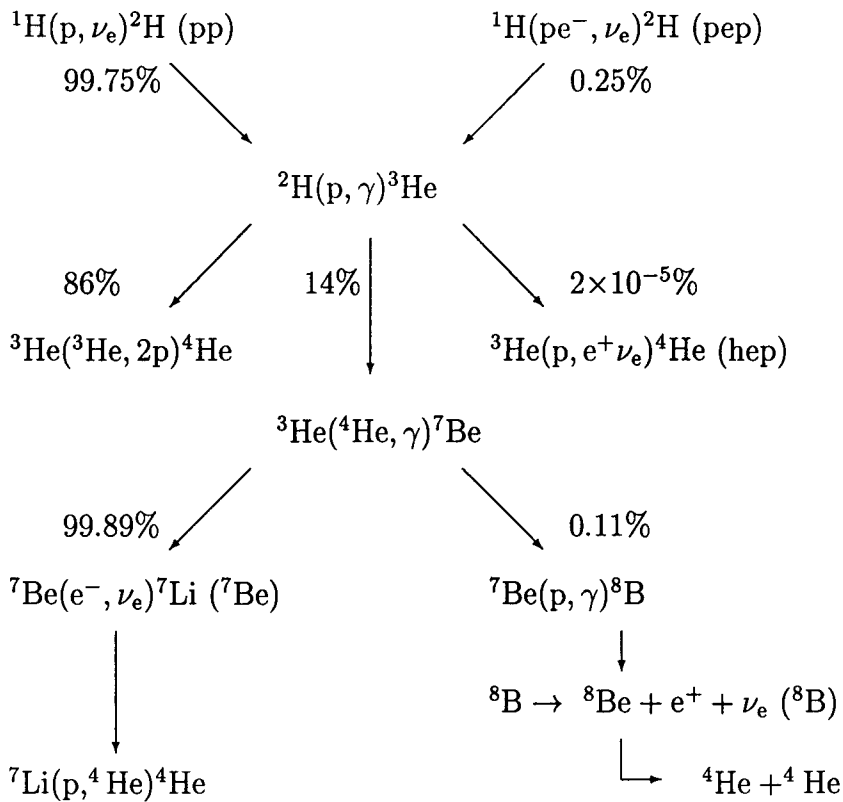


Figure 1.1: Solar fusion proton-proton chain.

1.2.1 The pp Chain

The thermonuclear energy in the Sun is generated primarily by fusion reactions associated with the conversion of hydrogen into helium. The processes are graphically depicted in Figure 1.1. The first reaction, proton-proton fusion, limits the overall rate. The Coulomb repulsion between the two protons is much greater than their kinetic energies. Fusion occurs only due to quantum mechanical tunneling, and is generally accomplished by protons in the high-energy tail of the kinetic energy distribution.

Five processes result in neutrino emission. The dominant flux is due to hydrogen fusion to form deuterium. Note that ${}^7\text{Be}$ electron capture and the pep reaction produce monoenergetic lines in the solar neutrino energy spectrum. All other reactions lead to β decay features.

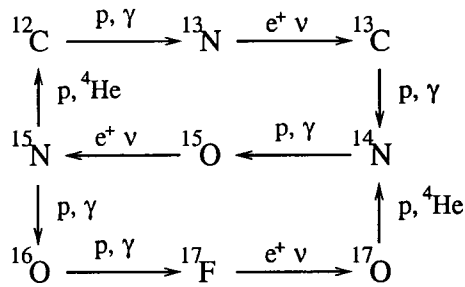


Figure 1.2: Solar fusion CNO cycle.

1.2.2 The CNO Cycle

The other mechanism for producing ${}^4\text{He}$ from protons depends on the initial solar ${}^{12}\text{C}$ abundance. A cycle involving a series of radiative proton capture, alpha and positron decays arises from the catalytic action of ${}^{12}\text{C}$. The isotopic abundances from ${}^{13}\text{C}$ through ${}^{18}\text{O}$ are enhanced from their primordial values. Neutrinos with endpoint energies between 1 and 2 MeV are produced from ${}^{13}\text{N}$, ${}^{15}\text{O}$ and ${}^{17}\text{F}$ beta decay. Very few neutrinos result from ${}^{18}\text{F}$ beta-decay. The CNO cycle is depicted in figure 1.2. Approximately 2% of the Sun's energy derives from the CNO cycle. A summary of solar neutrino reactions is provided in Table 1.2.

Reaction	Energy (MeV)
$p + p \rightarrow {}^2\text{H} + e^+ + \nu_e$	≤ 0.420
$p + e^- + p \rightarrow {}^2\text{H} + \nu_e$	1.552
${}^3\text{He} + p \rightarrow {}^4\text{He} + e^+ + \nu_e$	≤ 18.77
${}^8\text{B} \rightarrow {}^8\text{Be}^* + e^+ + \nu_e$	≤ 14.02
${}^7\text{Be} + e^- \rightarrow {}^7\text{Li} + \nu_e$	0.862 (90%)
	0.384 (10%)
${}^{13}\text{N} \rightarrow {}^{13}\text{C} + e^+ + \nu_e$	≤ 1.119
${}^{15}\text{O} \rightarrow {}^{15}\text{N} + e^+ + \nu_e$	≤ 1.732
${}^{17}\text{F} \rightarrow {}^{17}\text{O} + e^+ + \nu_e$	≤ 1.740

Table 1.2: The solar neutrino producing reactions.

Two-particle fusion in the solar environment is not able to overcome the instabilities at masses 5 and 8 that lead to dissociation into one or two α particles and unbound nucleons. The creation of nuclei with mass greater than 8 may occur by the coincident fusion of three ${}^4\text{He}$ nuclei, producing ${}^{12}\text{C}$. The rate for this triple α process is very low until pressures of 10^6 g/cm³ and temperatures of 10^8 K are achieved [24]. These higher temperatures are expected to occur after the star's core is depleted in hydrogen. As the radiation pressure from hydrogen fusion decreases, gravity contracts the star causing increased density and temperature. Contraction will continue until the triple alpha fusion rate is high enough to restore the hydrostatic equilibrium. This process is negligible in the Sun at present.

1.3 Solar Neutrino Observation

All attempts to observe neutrinos confront the same difficulty: neutrinos interact weakly with matter. The low energies of solar neutrinos compound the problem, since the interaction cross sections for neutrinos fall precipitously with decreasing energy. Solar neutrino experiments contend with cross sections on the order of 10^{-44} cm², or 10^{-20} barns. The technique of choice in many experiments is straightforward: identify a target with a relatively large cross section, a distinctive reaction signature, and gather as much of the target material as practical in an underground laboratory. These are necessary characteristics of a successful solar neutrino experiment, but they are not sufficient to ensure success. The issues of extracting the signal from the target and distinguishing signal from background are equally important.

1.3.1 Radiochemical Detectors

The first successful detection of solar neutrinos was performed using radiochemical detectors. Evidence of neutrinos is based on the chemical separation of atoms created by neutrino interactions from a large quantity of target atoms. The general reaction

is described in eq. 1.9.



The signal is the appearance of the ${}^A_{Z+1} Y$ atom. In the absence of other handles on the signal (time, energy, incident neutrino direction) the task of separating background from signal requires heroic efforts. The environment in which the detector is located must be very well understood for any background which could cause the reaction in Eq. 1.9. Additionally, the difficulty in separating a handful of ${}^A_{Z+1} Y$ atoms from $10^{30} {}^A_Z X$ atoms places a severe constraint on suitable target materials.

1.3.1.1 Homestake Chlorine Detector

The radiochemical technique was first successfully demonstrated in the Homestake gold mine in Lead, South Dakota [26]. The detector target is 100,000 liters of C_2Cl_4 (perchloroethylene), or dry cleaning fluid. The specific reaction occurs on ${}^{37}Cl$, as shown in eq. 1.10:



The reaction is accessible only to ν_e , and has a threshold energy of 814 keV, therefore, the reaction samples mainly 8B and 7Be ν_e .

The experiment saw the first solar ν data in 1968 and operated continuously until 1995. A proposal to resume operations is awaiting funding (March 1999). The typical run for the experiment lasts three months, and is limited by the 35-day half-life of ${}^{37}Ar$. The ${}^{37}Ar$ atoms are extracted from the C_2Cl_4 by means of percolation. Helium gas is introduced at the bottom of the tank through an array of pipes. The inert ${}^{37}Ar$ atoms are encouraged to move to the top of the tank through many collisions with helium atoms. The ${}^{37}Ar$ atoms are extracted from the helium using activated charcoal. The argon is desorbed from the charcoal. Counting is performed in a small proportional counter for three times the ${}^{37}Ar$ half-life. A complete description of the program at Homestake is provided in [27].

Results from the Homestake experiment appear in Figure 1.3. The data show large fluctuations about the mean of $2.56 \pm 0.16 \pm 0.16$ SNU², where the first error is statistical and the second is systematic. Attribution of the entire Homestake flux to ⁸B neutrinos allows an upper limit on the ⁸B neutrino flux to be established. This value is $2.25 \pm 0.21 \times 10^6$ cm² s⁻¹. The trend over thirty years is clearly well below that predicted by Standard Solar Models (SSM) (see Table 1.3). The recent model by Bahcall and Pinnsonneault includes the affects of heavy element settling and its associated influence on the radiative opacity of the Sun.

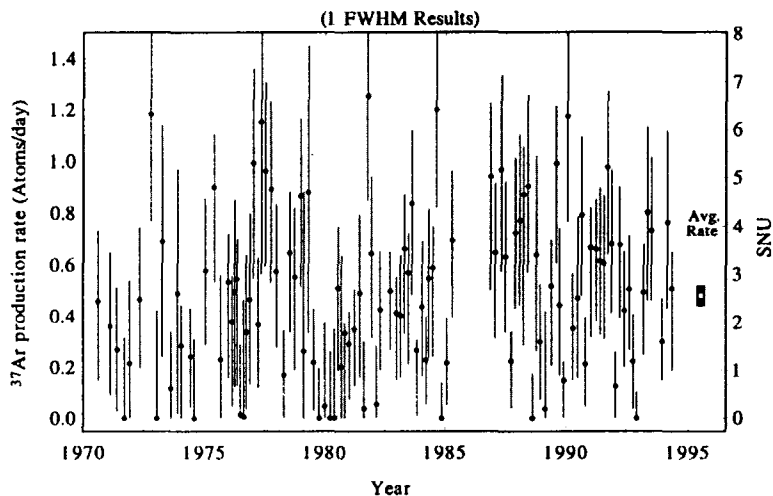


Figure 1.3: Data from the ³⁷Cl experiment. The average rate is well below the value predicted by Standard Solar Models.

1.3.1.2 Gallex

The Gallium Experiment (Gallex) has been observing neutrinos at the Gran Sasso Laboratory since May 1991. The inverse β -decay reaction ${}^{71}\text{Ga}(\nu_e, e^-){}^{71}\text{Ge}$ has a threshold energy of 233 keV, low enough to allow detection of p-p neutrinos. The detector contains 30 tons of natural abundance gallium, composed of 12 tons ⁷¹Ga and 18 tons ⁶⁹Ga. The half-life of ⁷¹Ge is 11.43 days, while $t_{1/2}$ for ⁶⁹Ge is 39 hours.

²SNU = Solar Neutrino Unit = 1 capture per 10^{36} target atoms per second

Model	Flux (SNU)
Bahcall and Pinsonneault (1998)	9.3
Bahcall and Pinsonneault (1995)	9.3
Turck-Chieze and Lopes (1993)	6.36
Sackman, Boothroyd and Fowler (1990)	7.64

Table 1.3: Total neutrino flux predicted by Standard Solar Models for the Homestake chlorine experiment.

The use of ^{69}Ga as a solar neutrino target is not practical because of the short half life.

The ^{71}Ge extraction is very efficient because it involves separation of GeCl_4 from GaCl_3 . The former is highly volatile, while the latter is not. Nitrogen is used as a percolating agent. Additional chemistry to separate Ge is required, and is described in [37]. The Gallex collaboration measured efficiencies greater than 99% for obtaining ^{71}Ge from the detector.

In addition to measuring the chemical extraction efficiency, Gallex was exposed to a neutrino calibration source [38]. The isotope ^{51}Cr is unstable by electron capture to ^{51}V , and produces 1.264-MeV (90%) and 0.944-MeV (10%) neutrinos. These energies are similar to those of the ^7Be solar neutrinos. The ^{51}Cr source activity was an astonishing 62.5 PBq (1.7 MCi). The detector was continually exposed to the source between 23 June and 10 October 1994. Eleven different extractions were made during this period, with the time between extractions intended to expose the detector to the same total neutrino flux. The results are presented as a ratio of counted activity over expected activity: 0.97 ± 0.11 . This experimental verification of the Gallex detector provides strong evidence that the issues of neutrino cross sections and extraction efficiency are well accounted for in this experiment.

The observed neutrino flux is reported at 76 ± 8 SNU [39], while the predicted flux is in the range 120-140 SNU. The result can account for the predicted p-p neutrino

signal, but it cannot also account for the ${}^7\text{Be}$ or ${}^8\text{B}$ predictions. The data from Gallex covering the period 1991 through 1997 are shown in Figure 1.4. Four major operating periods are defined:

- Gallex I – Initial operation (324 days)
- Gallex II – Change of target tanks (648 days)
- Gallex III – Following first ${}^{51}\text{Cr}$ calibration (353 days)
- Gallex IV – Following second ${}^{51}\text{Cr}$ calibration (268 days)

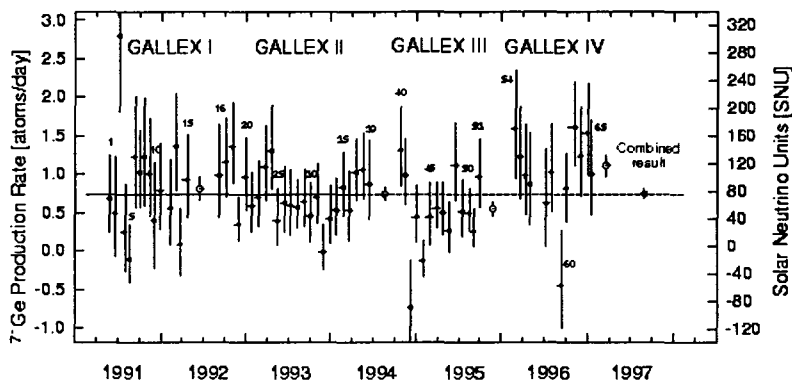


Figure 1.4: Production rate of ${}^{71}\text{Ge}$ for each run conducted by the Gallex solar neutrino experiment. The mean rate appears at the end of each operating period.

1.3.1.3 SAGE

The Soviet-American Gallium Experiment (SAGE) also used ${}^{71}\text{Ga}$ as a solar neutrino target. The observatory is located in Baksan, Russia and is currently inactive. The experiment used 55 tons of liquid Gallium metal, which required different chemical separation techniques [35] than used at Gallex. However, SAGE also conducted neutrino calibration studies as well as extensive extraction efficiency studies [36]. The results from SAGE ($69 \pm 10_{-8}^{+5}$ SNU) are in excellent agreement with those from Gallex,

but therefore also significantly disagree with standard solar model predictions. The interpretation of these results is deferred until section 1.4.

1.3.2 Čerenkov Detectors

The radiochemical experiments cannot prove that their signal is due to solar neutrinos. The number of product atoms which appear during a measurement period is available, but one must believe that backgrounds are understood to extraordinary levels, and then accept that only solar neutrinos are responsible for the signal which exceeds background. In fact, each radiochemical experiment indicates a negative flux for some measurement periods. The Homestake experiment, with an expected rate less than one ^{37}Ar atom per day, is particularly prone to measuring a negative net signal.

Direct evidence for solar neutrino observation requires correlating the neutrino direction with the direction of the Sun. The Čerenkov effect [28, 29] describes a process which allows real-time solar neutrino observation. A charged particle may have sufficient energy to move at speeds greater than the speed of light in a medium with a refractive index greater than unity. The particle's passage causes coherent polarization and relaxation of molecules and atoms in the media, leading to light emission (predominantly at 350-500 nm) in a cone along the particle's path.

A solar neutrino detector based on the Čerenkov effect requires a material that:

- is transparent at optical and ultraviolet wavelengths;
- has a refractive index allowing Čerenkov production for solar neutrino energies; and,
- may be collected in quantities large enough to satisfy the general conditions for solar neutrino detection.

These conditions have been satisfied by the Kamiokande and Super Kamiokande collaborations.

1.3.2.1 Kamiokande

The first water Čerenkov solar neutrino detector was successfully operated near Kamioka, Japan, during the period 1987-1995. A cylindrical cavity was filled with 2140 tonnes of high purity H_2O . Elastic scattering of electrons by solar neutrinos provided electrons moving in the same direction as the incident neutrino. The Čerenkov light was detected by 948 20" Hamamatsu photomultiplier tubes (PMTs) placed in the H_2O volume. The PMTs were mounted with their longitudinal axis normal to the detector outer surface. The time and charge associated with each PMT were recorded based on triggers for charge and number of PMTs (Nhits) exceeding threshold. The number of events is plotted in Figure 1.5 against direction from the Sun [32]. The clear peak at $\cos \theta_{\text{sun}}=1$ was the first direct observation of solar neutrinos.

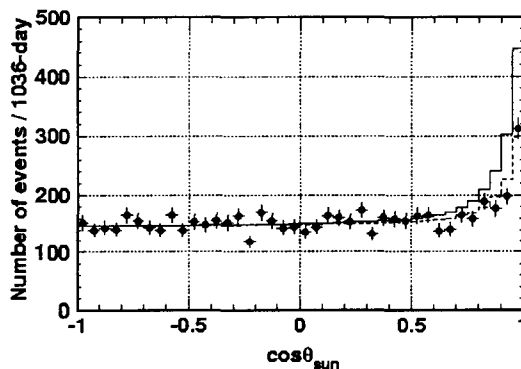


Figure 1.5: Solar neutrino elastic scattering event direction relative to Sun. Peak at $\cos \theta_{\text{sun}}=1$ shows that these neutrinos come from the Sun.

A number of issues limited the effectiveness of the Kamiokande detector. High background rates resulted in a detector threshold greater than 7.5 MeV. Thus, observations were limited to the higher energy ^8B and hep neutrinos. The backgrounds

were from radioactive materials in the detector and also cosmic ray induced muons. The latter affected the volume uniformly, and were identified using an external PMT array to provide a coincidence signal. The former were concentrated near the detector walls and PMTs. The interaction volume had to be reduced from 2140 to 680 tonnes to exclude the radioactive background influence.

The final result from Kamiokande for the ${}^8\text{B}$ neutrino flux represents between 49% and 64% of the predicted flux, and is $2.80 \pm 0.19 \pm 0.33 \times 10^6 \text{ cm}^{-2}\text{s}^{-1}$. The first uncertainty is statistical, and the second denotes the systematic uncertainties.

The Kamiokande measurement confirmed the order of magnitude measurement at Homestake. It was soon realized, however, that the Homestake and Kamiokande results were inconsistent with each other if the standard model description of neutrinos was correct. A comparison of the two experiments shows that Kamiokande, which is sensitive to high-energy ${}^8\text{B}$ neutrinos only, reports a higher ratio of observed flux compared to predicted flux than Homestake, where the ${}^{37}\text{Cl}$ detector is sensitive to more of the solar neutrino flux due to the lower detector threshold. This discrepancy suggested an energy dependent depletion of the observed solar neutrino flux.

1.3.2.2 *Super-Kamiokande*

The successful measurements at Kamiokande led to development of a detector intended to overcome its limitations. Super-Kamiokande [33] has 25 times the volume that was used at Kamiokande. An electron linac was obtained and modified to inject single electrons straight down into the water cavity for energy calibration. The Super-Kamiokande detector saw first data in May of 1996.

The energy spectrum for the first 504 days of data [34] is shown in Figure 1.6. The observed rate is compared to the rate predicted by the Bahcall-Pinsonneault 1998 SSM. The ratio of data to SSM prediction generally increases with energy. The final bin represents all data above 14 MeV. The differences between the shapes of the

measured and predicted spectra is evidence that the solar neutrino deficit may have an energy dependence.

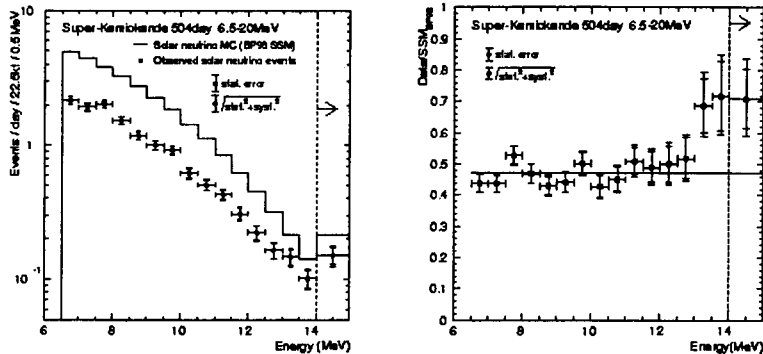


Figure 1.6: Left: Electron energy spectrum from Super-Kamiokande. Points with error bars denote data. Solid histogram denotes Monte Carlo prediction. Right: Ratio of observed electron energy spectrum and expectation from the SSM. Data are from the first 504 days at Super-Kamiokande. Note that all events above 14 MeV are combined in the highest bin.

1.4 Statement of the Solar Neutrino Problem

The Solar Neutrino Problem (SNP) may be stated very simply: Standard Solar Model predictions for solar neutrino flux are higher than the observed neutrino flux. The simple statement, however, fails to convey important information about the wealth of experimental data obtained during the past 30 years. In fact, many authors [40, 43] have described three solar neutrino problems, based on the unique results obtained from the three major observation techniques (chlorine, gallium, water).

The water Čerenkov results most closely reflect the simple SNP depiction. These experiments measure the ${}^8\text{B}$ flux above 6.5 MeV to be about half the value predicted by SSMs. The hep neutrinos are also observable in these experiments, and indications from Super Kamiokande are that this flux may be much higher than predicted. The calculated cross section for ${}^3\text{He}(p, e^+ + \nu_e){}^4\text{He}$ is not assigned an estimated uncer-

tainty in the recent review of solar fusion cross sections [41]. Analysis considering a greatly enhanced cross section for this reaction is shown to improve fits to the Super-Kamiokande data [42].

Chlorine detector results sample a much larger neutrino flux than the water Čerenkov detectors due to the lower reaction threshold. All neutrino reactions except for p-p contribute to this flux, though the high energy ${}^8\text{B}$ flux provides the major contribution. The measured flux is, however, only 36% of that predicted by SSMs. In fact, if the entire observed flux were due to only ${}^8\text{B}$, the chlorine experiment sees fewer neutrinos than the water Čerenkov detectors. Why does the detector with the lower energy threshold see fewer neutrinos than that with the higher threshold? It is shown in the next chapter that the answer to this question helps to discriminate amongst various proposed solutions to the SNP.

The gallium detectors have the advantage of being calibrated by intense neutrino sources. They also have the lowest thresholds and therefore the highest flux. The measurements are tied to the solar luminosity because of the contributions from p-p fusion. Both experiments report fluxes approximately 60% of the SSM predictions. The results may be attributed to observing essentially the full p-p flux, thus validating the general theory that p-p fusion powers the Sun, but in this case the flux expected from higher energy neutrinos is undetected.

Model independent analyses [43, 44] have been performed to account for these discrepant results. The practice is to attribute the flux to the three major components: p-p (Gallium), ${}^7\text{Be}$ (Gallium, Chlorine) and ${}^8\text{B}$ (Gallium, Chlorine, Water). In this case, the composite solar neutrino signal is attributed to 100% p-p prediction, 0% ${}^7\text{Be}$ prediction and 40% ${}^8\text{B}$ prediction. This description displays a dependence on energy which is hard to account for by varying inputs to Standard Solar Models, but is well described by matter-enhanced neutrino oscillations, as described in the next chapter.

2. Resolution of the Solar Neutrino Problem

The description of the Solar Neutrino Problem has evolved over the three decades during which it has been known. Solar neutrino observation capabilities have expanded to provide compelling evidence that the disagreement between theory and observation is robust. In this chapter we examine the inputs to the Standard Solar Models. This survey will include reviewing the helioseismology technique, solar interior modeling and nuclear reaction rate determination at solar energies. Consideration will be given to nonstandard neutrino physics. Neutrino flavor oscillation will be presented including the atmospheric neutrino results from Super-Kamiokande. A general description for neutrino oscillation modes directly relevant to the Solar Neutrino Problem will be presented. Finally, the prospects for resolution of the Solar Neutrino Problem will be considered.

2.1 *The Solar Interior*

The Sun's core is hot by terrestrial standards. The temperature has been determined to be in the range of $8-16 \times 10^6$ K in the core by inferences from helioseismic data [51, 50]. Hydrogen and helium are fully ionized at these temperatures. Elements such as lithium, beryllium and boron may be at times partly ionized, particularly in outer regions of the core. Heavier elements, especially iron, are partly ionized even at the upper range of temperatures.

Standard solar models (SSM) provide a means to calculate properties pertaining to solar structure (mass, radius, luminosity) and dynamics (rotation and solar neutrino fluxes). Conservative estimates concerning initial conditions are modified through a series of equilibrium states to recreate the presently observed solar properties. Observations are used to deduce modifications to the input parameters to bring SSMs into better agreement with data. The simplest assumptions consistent with data are used to provide input to standard solar models.

- Hydrostatic equilibrium is assumed throughout the solar evolution, in which the force due to gravity is balanced by the pressure resulting from energy released by nuclear fusion.
- Energy transport is well described by photon diffusion (radiative transfer) and convective motions. The Sun is considered to be divided into two regions: the innermost, in which radiative transfer is the dominant energy transport mechanism, and the outermost, in which convection dominates.
- Energy generation is due solely to nuclear reactions. While gravitational energy release contributes to the luminosity of young stars, the condition of hydrostatic equilibrium implies this condition.
- Abundance changes are caused solely by nuclear reactions. This condition neglects changes due to cosmic ray or meteoritic in-fall as well as losses due to solar wind particle emission.

2.1.1 Standard Solar Model Input

Four input parameters arise from these assumptions: chemical abundance, nuclear reaction rates, radiative opacity and the equation of state. The chemical abundance for elements above carbon is taken to match the meteoritic abundances which we date to the early solar system. The additional assumption is made that solar composition is uniform in these abundances at the time when hydrostatic equilibrium first applies.

Fusion reactions in the Sun occur at very low energy (~ 10 keV). Nuclear reaction rates have primarily been determined through laboratory measurements for energies of a few MeV down to about 100 keV. The practice has been to extrapolate the laboratory results to solar energies. Application of experimental results to the solar interior is not always straightforward. The screening by atomic or molecular electrons in the laboratory targets must be accounted for accurately. Screening effects must also be considered for the solar plasma.

The radiative opacity, or photon diffusion rate, is influenced by photon interactions with nuclei and ions. Nuclei provide free-free and free-bound electron interactions, which refer to the initial and final electron states. In addition, ions provide for bound-bound interactions, in which an electron bound to a nucleus experiences a change in the bound state due to interactions with a free electron. The largest uncertainties for radiative opacity calculations result from uncertainties in the heavy element abundances and their degree of ionization. The temperature-density profile of the solar interior requires an accurate radiative opacity profile.

The equation of state relates pressure to density and temperature. The classical plasma equation of state for an ideal gas of noninteracting ions and electrons is applied to the solar core. The expected ratio of the specific heats at constant temperature and pressure is $5/3$. The radial profile for this ratio may be deduced from helioseismology. Deviations from the expected value guide modifications to the solar model.

2.1.2 Helioseismology

The Sun may be treated as a spherical resonant cavity when considering internal pressure wave propagation. The waves are thought to result from stochastic fluctuations due to turbulence just below the photosphere. The Sun is transparent to these seismic waves, so that the waves persist for long periods, reflecting between inner regions and the surface. These waves impart velocities up to 20 cm s^{-1} to atoms and molecules at the Sun's surface. While many factors contribute to motion at the Sun's surface, Doppler-shifted spectral lines may be studied over long periods to deduce the pressure wave frequencies. By collecting data concerning many pressure wave modes over long continuous periods, it is possible to determine the sound speed as a function of solar radius. The density and pressure may then be deduced from the sound speed data through the relation defined by an equation of state used to describe the thermodynamic properties of the solar interior.

The study of solar pressure waves is known as helioseismology [45, 46, 47, 48]. A variety of complementary techniques is currently employed to obtain data. The first features a network of ground-based temporally-synchronized observatories located to provide constant solar monitoring. The second is an instrument flown on a satellite. The former instrument may be conveniently upgraded and calibrated and is exemplified by the Global Oscillation Network Group (GONG) [50]. The latter may pursue constant observation free of atmospheric turbulence and immune from terrestrial weather conditions. The present satellite observatory is the Solar and Heliospheric Observatory (SOHO) [51]. Additional ground-based instruments which observe different heights of the solar atmosphere also contribute to the study of helioseismology [52, 53].

The radial sound speed gradient in the Sun leads to reflection of downward traveling waves back toward the surface. Those with initial directions nearly direct to the Sun's center penetrate deeply before being reflected, while those traveling at large initial angles from the center undergo shallow reflections. The waves therefore are influenced by the material properties at different regions in the solar interior. One analysis technique [48] features decomposing the observed surface wave field by projecting onto theoretical eigenfunctions, which have spatial variations proportional to spherical harmonics. The temporal variation of the projection coefficients is Fourier analyzed to provide the frequency contributions to specific spherical harmonic modes.

The challenge is to clearly separate the effect of pressure waves from artifacts induced by the observational irregularities. These irregularities arise from the inability of instruments to observe the complete solar half-disk. There are difficulties acquiring data that are continuous in time. Additionally, changes in the Sun itself due to differential rotations of the surface as a function of latitude affect the surface velocity field. Mixing of amplitudes from neighboring spherical harmonics results from these observational influences.

Helioseismology results have been used to validate solar models. The direct measurement of sound speeds has been invaluable in constraining the helium abundance at the convection zone base and identifying errors in opacity calculations. The role of helioseismology has been to guide physics input in the models rather than changing parameters specific to individual processes. The deviation between model calculation of sound speed and helioseismic data just below the convection zone was resolved by the inclusion of gravitational settling of helium and heavier elements, rather than by adjusting parameters already in the model.

Helioseismology also provides constraints on the solar equation of state and opacity. It is important to recall that helioseismology does not directly determine temperature and elemental abundance. Present solar models continue to treat the solar core in the simplest way consistent with data. Refined helioseismology data and, ultimately, data from solar neutrino observation will be used to further constrain the models.

2.2 Nuclear Reaction Rates

Solar fusion rates are clearly of great importance in determining the solar neutrino flux. The process by which these rates are determined is complicated by differences between the stellar environment in which they occur and the terrestrial environment in which they are measured. Screening effects must be considered in the laboratory and in the Sun. The low energies and long time scales associated with the reactions make direct measurements difficult (${}^3\text{He}$ - ${}^3\text{He}$, ${}^3\text{He}$ - ${}^4\text{He}$, hep) if not impossible (pp, pep, ${}^7\text{Be}$ electron capture in a fully ionized plasma).

There exists a symbiotic relationship between solar neutrino experiments and experimental solar fusion reaction determination and isotopic abundances in the Sun's core provided the issue of neutrino propagation is settled. Accurate fusion reaction rates will allow low uncertainty predictions for solar neutrino fluxes. Flux measure-

ments (taken together with helioseismic bounds) will allow abundances to be verified. The adjusted abundances may then be used as input for a new round of predicted fluxes.

The reader is referred to the recent work by Adelberger *et al.* [41], for a comprehensive review of solar fusion reaction rates. A summary of the parameters measured in the laboratory and those matters that influence their determination and application to the solar environment is presented here. Attention is given to results concerning those reactions with major influence and/or uncertainties affecting solar neutrino experiments.

2.2.1 Laboratory Measurements

Quantum mechanical tunneling allows nuclear fusion to occur in the Sun's core. Nuclear reactions take place between specific particles in the plasma. The most probable energy for a reaction to occur, E_0 , is given by Gamow as:

$$\begin{aligned} E_0 &= [(\pi\alpha Z_1 Z_2 kT)^2 (mAc^2/2)]^{\frac{1}{3}} \\ &= 1.2204(Z_1^2 Z_2^2 AT_6^2)^{\frac{1}{3}} \text{keV}. \end{aligned} \tag{2.1}$$

The reduced mass, $A = A_1 A_2 / (A_1 + A_2)$, the atomic-mass unit, m , and the charge numbers (atomic mass numbers) of the colliding nuclei are Z_1 and Z_2 and (A_1 and A_2), and the temperature, T , is given in units of 10^6 K. The Gamow energies are calculated for selected reactions at the central core temperature 16×10^6 K in Table 2.1. These energies are far below the Coulomb barriers (few hundred keV) making clear the requirement for tunneling.

E_0 (keV)	Reaction
5.0	pp
9.2	hep
18.3	${}^3\text{He}-{}^3\text{He}$
19.2	${}^3\text{He}-{}^4\text{He}$
15.3	${}^7\text{Be}-\text{p}$
20.4	${}^{12}\text{C}-\text{p}$

Table 2.1: Gamow energies for selected solar fusion reactions. The central core temperature 16×10^6 K is assumed, providing upper bounds.

Measurements in the laboratory seek to determine the nonresonant fusion cross section described by

$$\sigma(E) = \frac{S(E)}{E} \exp(-2\pi\eta(E)). \quad (2.2)$$

The Sommerfeld parameter, $\eta(E) = \frac{Z_1 Z_2 e^2}{\hbar \nu}$, describes the Coulomb force between the two nuclei, where the center-of-mass energy is E , and the relative velocity in the entrance channel is $\nu = (2E/\mu)^{1/2}$ ($\mu = mA$ is the reduced mass of the system).

The factor $S(E)$ is slowly varying and may be approximated by

$$S(E) = S(0) + S'(0)E + \frac{1}{2}S''(0)E^2. \quad (2.3)$$

It is the parameters $S(0)$, $S'(0)$ and $S''(0)$ that are determined from experiment. This is accomplished by obtaining data in the energy range below 2 MeV and fitting the data to the function $S(E)$. In practice, making measurements below 100 keV has been very difficult because of the small reaction cross sections. Intense beams are necessary to compensate for limited quantities of target nuclei. High purity targets and beams are required to reduce backgrounds. In fact, there has been only one experiment to measure the S -factors at the Gamow energy, and is described below in section 2.2.4. Once obtained at the higher energies, the cross section $\sigma(E)$ is then extrapolated to the lower energies applicable to solar fusion.

2.2.2 Screening

Low energy nuclear reaction rates are mainly determined by the Coulomb interactions between the nuclei, and are therefore affected by the screening of the nuclear charge by electrons in the target. The electrons are bound to target atoms in laboratory experiments, while they occupy mainly continuum states in the solar plasma. Screening increases the observed rates in both cases. The effects of screening must be known to determine the unscreened laboratory S -factors. The stellar screening is deduced independently, and applied to unscreened S -factors to determine the solar reaction rates.

The resulting enhancement in laboratory experiments is dependent on energy (Eq. 2.4),

$$f(E) = \frac{\sigma_{exp}(E)}{\sigma(E)} \sim \exp \left\{ \pi \eta(E) \frac{U_e}{E} \right\} \quad (2.4)$$

where the approximation is good for electron screening energy, U_e , much less than scattering energy, E . Solar screening is well described using Debye-Hückel screening through the relation [55],

$$f = \exp \left\{ \frac{Z_1 Z_2 e^2}{k T R_D} \right\} \quad (2.5)$$

where R_D is the Debye radius and T is temperature in Kelvin. This relation considers the effect due to electron degeneracy and is valid in the weak-screening limit defined by $k T R_D \geq Z_1 Z_2 e^2$. The effects due to screening are considered to produce uncertainties in the corresponding reaction rates of order a few percent.

2.2.3 The ${}^7\text{Be}(p,\gamma){}^8\text{B}$ Reaction

The determination of observation rates for all Čerenkov experiments and the chlorine experiment depend directly on the reaction ${}^7\text{Be}(p,\gamma){}^8\text{B}$. Direct experiments have been conducted and the experimental difficulties are numerous, chiefly arising from the issue of using the radioactive ${}^7\text{Be}$ target. The direct measurement

of the ${}^7\text{Be}(p, \gamma){}^8\text{B}$ S -factors is accomplished by detecting the ${}^8\text{B}$ β^+ -decay activity ($t_{1/2} = 0.7$ s) in coincidence with the β -delayed α 's. The radioactive target material has made it very difficult to establish the absolute normalization of the cross section as a function of energy, however, the experiments measure the same shape for the cross section.

Indirect techniques include dissociation of ${}^8\text{B}$ in the Coulomb field of heavy nuclei and measurement of the nuclear vertex constant for ${}^8\text{B} \rightarrow {}^7\text{Be} + p$. These techniques are promising due to the completely different set of associated systematic uncertainties. This same point is at present the greatest drawback to the successful extraction of the cross sections.

The Adelberger review paper recommends the value

$$S_{17}(0) = 19_{-2}^{+4} \text{ eV b} \quad (2.6)$$

which is based entirely on the work of Phillipone *et al.* [56, 57, 58] and is 15% smaller than the previous, widely used value of 22.4 eV barn, which was based on a weighted average of all available experiments. The error estimates refer to combined statistical and systematic uncertainties, but reflect only a 1σ value.

The reviewers note that relying on one experiment for the recommended $S_{17}(0)$ value demonstrates the unsatisfactory state of our present knowledge. Several laboratories are engaged in experiments with radioactive beams, which offer promise for improving the current situation, although presenting unique systematic effects which must be well understood. The high degree of interest in this measurement guarantees continued efforts to verify the existing $S_{17}(0)$ value and reduce the uncertainty to 5% or less.

2.2.4 The ${}^3\text{He}({}^3\text{He},2\text{p}){}^4\text{He}$ and ${}^3\text{He}({}^4\text{He},\gamma){}^7\text{Be}$ Reactions

The total ${}^7\text{Be}$ and ${}^8\text{B}$ neutrino flux depends on the production of ${}^7\text{Be}$, which is in turn determined by the competing reactions ${}^3\text{He}({}^3\text{He},2\text{p}){}^4\text{He}$ and ${}^3\text{He}({}^4\text{He},\gamma){}^7\text{Be}$ (the reaction ${}^3\text{He}(\text{p},\text{e}^+\nu_{\text{e}}){}^4\text{He}$ is known to be at least 4 orders of magnitude weaker). The flux depends on the ratio of these two reaction rates. The uncertainty in the flux then is

$$\delta = \sqrt{\left(\frac{\delta S_{33}}{S_{33}}\right)^2 + \left(\frac{\delta S_{34}}{S_{34}}\right)^2}. \quad (2.7)$$

The methods to determine these rates are summarized and results are discussed below.

Only the ${}^3\text{He}({}^3\text{He},2\text{p}){}^4\text{He}$ fusion cross section has been measured directly at solar energies. The experiment was performed by the Laboratory for Underground Nuclear Astrophysics (LUNA) Collaboration [59] at the Gran Sasso Laboratory in central Italy. The success of the experiment is due to a high intensity, low energy ${}^3\text{He}$ beam (500 microamps at 40 keV) and a high purity ${}^3\text{He}$ gas target. Alpha and proton events are distinguished using $\Delta E - E$ coincident detection of the final state protons. Silicon surface barrier detectors are used, 140 microns for ΔE and 1000 microns for E detection. The α will be stopped in the ΔE detector, while the protons produce $\Delta E - E$ coincidence signals. This type of coincidence detection also provides suppression of γ -ray backgrounds from the underground laboratory. Additionally, background due to deuterium impurities from HD^+ ions, mainly in the beam, arises from ${}^3\text{He}(\text{d},\text{p}){}^4\text{He}$. The two-particle final state leads to monoenergetic protons (14.9 MeV) which are clearly distinguished from the signal protons (0-10.7 MeV).

The measurement has been conducted for center-of-mass energies in the range of 24.80-20.76 keV. This data, together with data obtained at higher energies, was used to obtain the S -factors, leading to the determination of $S_{33}(0)=5.4\pm 0.05$ MeV b. The experiment continues with an enhanced target cell and refined detector geometries.

Source	S -factor $S_{34}(0)$ (keV b)
in-beam capture γ -ray	0.507 ± 0.016
activity	0.572 ± 0.026
average	0.53 ± 0.05

Table 2.2: Average ${}^3\text{He}(\alpha, \gamma){}^7\text{Be}$ cross section results for capture γ -ray and activity determination methods.

The LUNA Collaboration expect to measure the S -factor to below 15 keV in the center of mass frame.

The ${}^3\text{He}(\alpha, \gamma){}^7\text{Be}$ reaction has been studied by two methods. The in-beam capture γ -rays from the production of ${}^7\text{Be}$ are used to deduce the cross section. Alternatively, the resulting radioactivity may be determined offline, providing the cross section directly. Results from these techniques disagree by about 2.5σ . Adelberger *et al.* choose to resolve the disagreement by recommending a weighted average of the two groups of results, which are shown in Table 2.2.

The solar fusion cross sections vary with energy, and each reaction has a different Gamow temperature, making broad comparisons between results somewhat awkward. However, cross section ratios are directly proportional to the S -factor ratios. For σ_{33}/σ_{34} the ratio is given in Eq. 2.8

$$\frac{\sigma_{33}}{\sigma_{34}} = \frac{\exp(-3\pi)S_{33}}{\exp(-\frac{24}{7}\pi)S_{34}} = 3.8 \times 10^3. \quad (2.8)$$

The reaction rate ratio is given by the product of the cross section and abundance ratios. The ${}^3\text{He}/{}^4\text{He}$ abundance ratio is 1.7×10^{-4} (adapted from [60]). Thus ${}^3\text{He}$ will have far more interactions with ${}^4\text{He}$ than other ${}^3\text{He}$. The large cross section ratio is tempered by the abundance ratio to result in the reaction rate ratio of about 6:1.

The major contributions to the reaction rate ratio uncertainty are the uncertainties in the S_{34} measurement (10%) and the ${}^3\text{He}/{}^4\text{He}$ abundance ratio ($O(10\%)$). The

reaction rate ratio uncertainty is estimated using Eq. 2.7 to be approximately 14%. Clearly, improved neutrino flux calculations will result from improved determinations of S_{34} and ${}^3\text{He}/{}^4\text{He}$.

2.2.5 ${}^7\text{Be}$ Electron Capture

The electron capture process is a form of β decay in which a bound electron is captured by the nucleus, converts a proton in the nucleus into a neutron and results in emission of a neutrino. Electrons in the K- and L- shells primarily participate in this process (approximately 90% and 10%, respectively), because these orbitals have the highest probabilities for overlapping the nucleus. The reaction rate also depends on the overlap between initial and final nuclear state matrix elements and the weak interaction coupling constant.

The decay of ${}^7\text{Be}$ is exclusively by electron capture and the half-life is measured to be 53.12 ± 0.07 days [61]. Ionization conditions must be considered when determining the ${}^7\text{Be}$ half-life in the Sun's core. Since the ${}^7\text{Be}$ production and destruction are in equilibrium, the ${}^7\text{Be}$ flux is insensitive to the electron capture lifetime. However, a significantly longer half-life than presently calculated would increase the equilibrium concentration of ${}^7\text{Be}$ in the Sun, therefore increasing the ${}^8\text{B}$ flux by providing more targets for the ${}^7\text{Be}(p,\gamma){}^8\text{B}$ reaction.

Solar conditions are such that ${}^7\text{Be}$ is completely ionized, although the dynamic conditions allow continuum electrons to be temporarily captured into bound states. Bahcall [63] first considered the continuum state contribution and Iben, Kalata, and Schwartz [64] that from bound states. The current calculation for the ${}^7\text{Be}$ electron capture rate, $R_{7\text{Be}}$, gives

$$R_{7\text{Be}} = 5.60 \times 10^{-9} (\rho/\mu_e) T_6^{-1/2} \times [1 + 0.004(T_6 - 16)] \text{s}^{-1} \quad (2.9)$$

where μ_e is the electron mean molecular weight. Selecting representative values at the solar core for $\mu_e = 1.14$, $\rho = 150\text{g/cm}^3$, and temperature (in units of 10^6 K) $= 16$, the maximum rate is $1.84 \times 10^{-7} \text{ s}^{-1}$. The ${}^7\text{Be}$ half-life in the solar plasma is therefore $R_{7\text{Be}}^{-1} = 5.43 \times 10^6 \text{ s}$ or 62.8 days, an enhancement of 18% compared to the terrestrial half-life.

An alternate technique that does not rely on electron states, but rather uses a density matrix [65] to describe the plasma, recently has been employed by Gruzinov and Bahcall [55]. The two results agree to within 1%.

2.2.6 Standard Solar Models and Solar Neutrinos

Helioseismology has led to numerous extensions to the standard solar model described in Section 2.1. How has this effected the predictions for solar neutrino fluxes? A comparison is made in Table 2.3 between the Bahcall and Ulrich (1988) and Bahcall and Pinsonneault (1998) models. The results show no appreciable difference in the flux except for hep neutrinos, which is decreased by a factor of 4. The major change has been to decrease the associated uncertainties. Does this result mean that solar neutrino fluxes are insensitive to solar model details? Yes and no. The preponderance of data leads to great confidence in solar neutrino fluxes at the 10% level. In particular, the validity of predictions for the pp flux seems well verified by the luminosity constraint. Improved accuracy in the ${}^7\text{Be}$ and ${}^8\text{B}$ neutrino flux predictions requires improved nuclear reaction rate measurements for ${}^3\text{He}(\alpha, \gamma){}^7\text{Be}$ and ${}^7\text{Be}(p, \gamma){}^8\text{B}$ [80]. It is true that the solar neutrino branch for ${}^8\text{B}$ has no influence on the solar structure properties predicted by solar models.

The jury remains out on several issues concerning the solar structure and possible influences on the solar core. The solar interior is now believed to rotate with a rate different from that of the Sun's exterior. The exterior itself displays non-uniform rotation rates, with the polar material rotating at 25 days per revolution, while the

Source	Flux ($10^{10}\text{cm}^{-2}\text{s}^{-1}$)	
	BU (1988)	BP (1998)
pp	$6.0 (1\pm 0.02)$	$5.94 (1.00\pm 0.01)$
pep	$1.4\times 10^{-2}(1\pm 0.05)$	$0.014 (1.00\pm 0.01)$
hep	8×10^{-7}	2.1×10^{-7}
${}^7\text{Be}$	$0.47 (1\pm 0.15)$	$0.48 (1.00\pm 0.09)$
${}^8\text{B}$	$5.8\times 10^{-4} (1\pm 0.37)$	$5.15\times 10^{-4} (1.00^{+0.19}_{-0.14})$
${}^{13}\text{N}$	$6.0\times 10^{-2}(1\pm 0.50)$	$6.05\times 10^{-2} (1.00^{+0.19}_{-0.13})$
${}^{15}\text{O}$	$5.0\times 10^{-2}(1\pm 0.58)$	$5.32\times 10^{-2} (1.00^{+0.22}_{-0.15})$
${}^{17}\text{F}$	$5.2\times 10^{-4} (1\pm 0.46)$	$6.33\times 10^{-4} (1.00^{+0.12}_{-0.11})$

Table 2.3: Solar neutrino fluxes predicted by standard solar models prior to (BU (1988)) and following (BP (1998)) extensions arising in part from helioseismology.

equatorial rate is 35 days per revolution. There exists a discontinuity in the radial sound speed gradient associated with the boundary between convection zone and radiative interior. Solar models treat the boundary as discrete, while a continuous treatment may be appropriate. There is a need to explore the differential rotation dynamics for implications on abundance mixing, which is an area largely unaddressed in solar models.

Solar models are in good agreement with helioseismic oscillation frequency data. The models do not agree well with the observed solar neutrino flux. Extensive efforts to vary solar model parameters have been conducted [66], and none have proved suitable for solving the solar neutrino problem. An alternative explanation concerns modification to neutrino physics in the Standard Model of weak interactions. Neutrino oscillations stand out as the most elegant and applicable modification.

2.3 Neutrino Oscillations

Experimental evidence has predominantly supported the belief that the number of leptons of the same family are conserved in weak interactions. Beta decay (electron), muon and pion decay (muon) and tauon decay (tauon) are interpreted in this manner.

Therefore it is natural to assume that neutrino flavor eigenstates are appropriate to describe neutrino evolution. Solar neutrino analysis has suggested that neutrino flavor eigenstates may evolve in time [67, 68, 69]. Recent experimental results from atmospheric neutrino study at Super-Kamiokande strongly support this idea. The proposed solution to the solar neutrino problem which best fits all existing data features matter-enhanced oscillations in the Sun's core.

The theory for neutrino flavor oscillation will be reviewed. The case of two-flavor vacuum oscillations will be presented. The enhancement of oscillations by propagation through high electron density regions, named the Mikheyev-Smirnov-Wolfenstein (MSW) effect, will be considered and applied to the solar neutrino problem.

2.3.1 Oscillations in Vacuum

There is no theoretic basis to assume that neutrinos are massless. There is also no *a priori* reason to assume concordance between mass and flavor eigenstates. If mixing is allowed between mass eigenstates, it is possible for the neutrino flavor eigenstate to vary with time. In this case, the flavor and mass eigenstates may be connected through a unitary transformation, described by

$$\nu_\alpha(x) = \sum_{m=1,2,3} U_{\alpha m} \nu_m(x). \quad (2.10)$$

The flavor eigenstate $\nu_\alpha(x)$ is composed of a mixture of mass eigenstates $\nu_m(x)$. The neutrino mass eigenstate mixture will evolve with time as any quantum mechanical eigenstate:

$$\psi(t) = e^{-iE_m t} \psi(t=0). \quad (2.11)$$

The relative mass eigenstate proportions change with time, causing the flavor eigenstate to oscillate. In the standard presentation [70], two-flavor oscillations are considered. (Three-flavor neutrino oscillation has been considered by many authors [71].)

The unitary mixing matrix $U_{\alpha m}$ becomes

$$U_{\alpha m} = \begin{pmatrix} \cos\theta & \sin\theta \\ -\sin\theta & \cos\theta \end{pmatrix} \quad (2.12)$$

where θ is the mass mixing angle. The flavor eigenstates ($\nu_{e,\mu,\tau}$) are expressed as mass eigenstate ($\nu_{1,2,3}$) mixtures, as seen in 2.13:

$$\begin{aligned} |\nu_e\rangle &= \cos\theta|\nu_1\rangle + \sin\theta|\nu_2\rangle \\ |\nu_\mu\rangle &= \sin\theta|\nu_1\rangle - \cos\theta|\nu_2\rangle \end{aligned} \quad (2.13)$$

The probability that ν_e oscillates to ν_μ (remains ν_e) is given by 2.14 (2.15).

$$P_{\nu_e \rightarrow \nu_\mu} = \sin^2(2\theta)\sin^2\frac{\delta m^2 x}{4E} \quad (2.14)$$

$$P_{\nu_e \rightarrow \nu_e} = 1 - \sin^2(2\theta)\sin^2\frac{\delta m^2 x}{4E} \quad (2.15)$$

where $\delta m^2 = |m_1^2 - m_2^2|$, x is the distance from the neutrino source and E is the neutrino energy. The probabilities oscillate with a characteristic length $L_V = 4\pi E/\delta m^2$, so that a distance $L_V(n + 1/2)$ from the point of origin, the ν_e (ν_μ) content is maximally suppressed (enhanced). The probability for transformation is proportional to the mixing angle. Maximal mixing occurs for $\theta = \pi/4$.

The oscillation length defines the scale over which oscillations occur. For distances much less than L_V , the probability for oscillation is small. For distances much greater than L_V , the probability goes to 50%. This is because the oscillations require coherence between the mass eigenstates. Since these eigenstates propagate with different velocity due to their different momentum, the eigenstates will separate, with 50% of the initial flux going into each flavor eigenstate. The oscillation length must be much less than the coherence length for oscillations to occur.

Neutrino oscillation experiments have been conducted with sources covering many energies and oscillation lengths. The interpretation generally seeks to define the parameters δm^2 and $\sin^2(2\theta)$. A list of experiments and their parameter limits is shown in Table 2.4. It is customary to produce plots which define excluded regions of this two dimensional parameter space due to the lack of success associated with observing neutrino oscillations. An example is shown in Figure 2.1, taken from results published by the NOMAD collaboration [72]

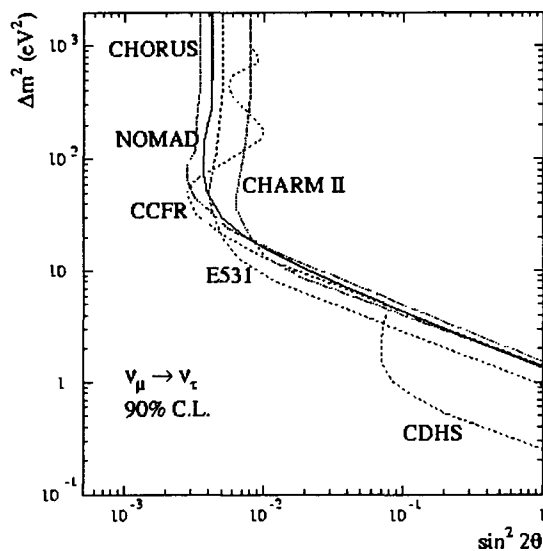


Figure 2.1: The δm^2 - $\sin^2(2\theta)$ parameter space. The region excluded by the NOMAD $\nu_\mu \nu_\tau$ appearance experiment (solid line) compared with exclusion results from previous experiments. The plot illustrates that incremental improvements in sensitivity may occur in either δm^2 , $\sin^2(2\theta)$ or both parameters simultaneously.

The plot concerns an experiment concerned with the appearance of ν_τ in the NOMAD detector at CERN. Protons (450 GeV/nucleon) impinge on a beryllium target to produce a nearly pure ν_μ beam at CERN in the NOMAD. The detector is composed of drift-chambers, transition radiation detectors and calorimeters to provide sensitivity for charged particles arising from τ^- decay. The ν_μ energy (26 GeV)

Experiment	$E_{\nu_{\min}}$ (MeV)	x_{\max} (m)	δm_{\min}^2 (eV ²)
reactor	1	10 ²	10 ⁻²
meson factory	10	10 ²	10 ⁻¹
high energy accelerator	10 ³	10 ⁴	10 ⁻¹
Sun	2×10 ⁻¹	10 ¹¹	10 ⁻¹²

Table 2.4: Values of the parameter δm_{\min}^2 which characterises the sensitivity regions of different neutrino oscillation experiments.

and distance to the detector (625 m) were well known. The experiment provided fewer candidate events than expected from backgrounds, and thus represents a null result. The probability for appearance was determined to be $< 2.1 \times 10^{-3}$, with $\sin^2(2\theta) < 4.2 \times 10^{-3}$ for large δm^2 .

The accelerator experiments are concerned with neutrino beams having well known energy and flavor. This leads to a straightforward determination of oscillation parameters. Analysis to consider vacuum oscillations as a solution for the solar neutrino problem must consider the solar neutrino energy spectrum and fluxes. Results from a best-fit to the data performed by Fogli, Lisi and Montanino [75] yield $\sin^2(2\theta) = 0.96$ and $\delta m^2 = 6.0 \times 10^{-11} \text{eV}^2$ with a $\chi_{\min}^2 = 2.5$. This result does not rule out vacuum oscillations as providing a solution consistent with all experiments, but does suggest that it is somewhat unlikely.

2.3.2 Atmospheric Neutrinos at Super-Kamiokande

Cosmic ray interactions in the atmosphere produce pions which create neutrinos when they decay. Both ν_{μ} and ν_{τ} are produced, in a ratio 2:1 at energy below 2.5 GeV and rising with E_{ν} . These interactions provide a powerful tool to search for neutrino oscillations, since the range of distances between neutrino source and detector varies between a few kilometers (production overhead) and 10,000 kilometers (production on the opposite side of the Earth).

In July 1998, the Super-Kamiokande Collaboration released an atmospheric neutrino analysis which describes a ν_μ deficit which depends on zenith angle when compared with Monte Carlo predictions [77]. The observed ν_e spectrum matches the Monte Carlo prediction. The interpretation offered is that $\nu_\mu \leftrightarrow \nu_\tau$ vacuum oscillations occur. The parameters for mixing are $|\delta m^2| = 2 \times 10^{-3}$ and $\sin^2(2\theta_V) = 1.0$. The vacuum mixing angle is therefore $\theta_V = \pi/4$, satisfying the condition for maximal mixing. The ν_τ mass is 1.8 GeV, which is large enough to greatly suppress tauon production. Additional analysis to extract evidence for tauon events continues. (The NOMAD accelerator experiment, sensitive to $\delta m^2 \sim 1$ for maximal mixing, used a baseline 3 orders of magnitude too small to observe ν_μ - ν_τ oscillations.)

The atmospheric neutrino analysis is strong evidence for neutrino vacuum oscillations as a general principle. It does not provide direct evidence concerning the solar neutrino situation, because the oscillation mode does not include ν_e .

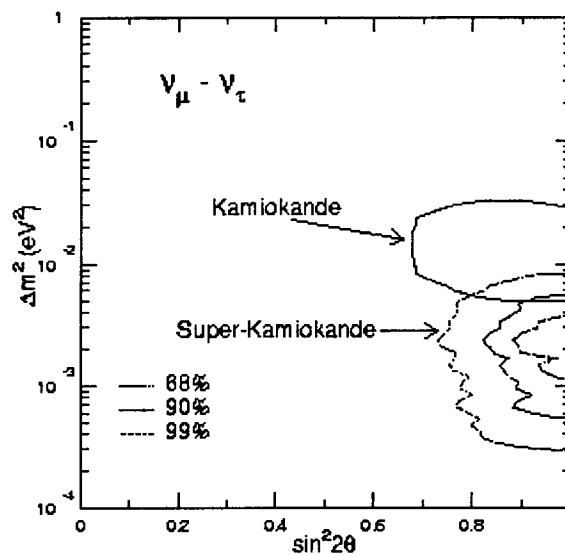


Figure 2.2: The δm^2 - $\sin^2(2\theta)$ parameter space for atmospheric neutrinos at Super-Kamiokande. The analysis fixes values for δm^2 and $\sin^2(2\theta)$ due to the suppression of the detector signal compared to Monte Carlo expectations. The result is compared to earlier analysis from the much smaller Kamiokande detector.

2.3.3 Matter-Enhanced Oscillations

Neutrino interactions in matter are influenced by the electron density in such a way that a resonance condition may exist which greatly enhances the oscillation probability. Mikheyev and Smirnov [78] developed this theory based on earlier work by Wolfenstein [79]. The result is known as the MSW effect, or matter-enhanced oscillations. The original result has been discussed and applied to solar neutrino analysis by many authors [73, 74, 43, 75, 76]. A brief summary is provided of the MSW effect and the resulting oscillation parameters for solar neutrinos.

The electrons in matter interact with ν_e via charged- and neutral-current interactions, but only by neutral interactions for ν_μ and ν_τ . Electron neutrinos then may acquire a higher effective mass in matter than ν_μ or ν_τ . The neutral current interaction probabilities are equal for all three neutrino flavors, therefore only the charged current for ν_e need be considered in the calculations. The discussion below follows that from Bahcall [73] Chapter 9.

Consider neutrino three-flavor mixing and an arbitrary eigenstate

$$|\nu \rangle_t = c_e(t)|\nu_e \rangle + c_\mu(t)|\nu_\mu \rangle + c_\tau(t)|\nu_\tau \rangle \quad (2.16)$$

featuring time-dependent coefficients. The time evolution of the eigenstate may be described using a mass matrix $M = M_0 + M_{matter}$:

$$i \frac{d}{dt} \begin{pmatrix} c_e(t) \\ c_\mu(t) \\ c_\tau(t) \end{pmatrix} = M \begin{pmatrix} c_e(t) \\ c_\mu(t) \\ c_\tau(t) \end{pmatrix}. \quad (2.17)$$

It has been shown [79] that the matter matrix, M_{matter} , contains a term which reflects the additional interaction available to ν_e . The term represents the contribution to the neutrino index of refraction in matter from electron- ν_e scattering.

Turning to two-flavor mixing for illustration, and inserting appropriate values for M , Eq. 2.17 becomes

$$i \frac{d}{dt} \begin{pmatrix} c_e(t) \\ c_\mu(t) \end{pmatrix} = \pm \frac{\Delta_M}{2} \begin{pmatrix} -\cos(2\theta_M) & \sin(2\theta_M) \\ \sin(2\theta_M) & \cos(2\theta_M) \end{pmatrix} \begin{pmatrix} c_e(t) \\ c_\mu(t) \end{pmatrix} \quad (2.18)$$

where the difference in energy between the two eigenstates $|\nu_e\rangle$ and $|\nu_\mu\rangle$, Δ_M , is given by

$$\Delta_M = \left[(\pm\Delta_V \cos(2\theta_V) - \sqrt{2}G_F n_e)^2 + (\Delta_V \sin(2\theta_V))^2 \right]^{1/2}. \quad (2.19)$$

The mixing angle in matter is related to the vacuum mixing angle by the relation

$$\tan(2\theta_M) = \frac{\tan(2\theta_V)}{1 \pm (L_V/L_e)\sec(2\theta_V)}. \quad (2.20)$$

The electron interaction length, L_e , is independent of energy, unlike the vacuum oscillation length.

The resonant condition arising from matter enhanced oscillations may be illustrated through Eq. 2.20. The maximal value occurs when $(L_V/L_e) = \cos(2\theta_V)$, giving $\theta_M = \pi/4$. The electron interaction length is inversely proportional to electron density. Therefore, large matter mixing angles may occur for small vacuum mixing angles if the electron density is sufficient to satisfy the resonance condition. The resonant electron density

$$n_{e,\text{res}} = \frac{|\delta m^2| \cos(2\theta_V)}{2\sqrt{2}G_F E} \quad (2.21)$$

then determines whether or not resonant oscillations occur. This relation is dependent on the splitting between mass eigenstates, the vacuum mixing angle and neutrino energy. Bahcall considers the case of small vacuum mixing ($\cos(2\theta_V) \sim 1$) and assumes mass eigenstate splitting ($\sim 10^{-4}\text{eV}^2$) to find the minimum energy required for achieving resonance to be 6.6 MeV at solar core electron densities. The condition

for a minimum energy is removed if the mixing between ν_e and other neutrino flavors is maximal.

2.4 Prospects for Resolving the Solar Neutrino Problem

Resolution to the Solar Neutrino Problem may be sought through corrections to standard solar model input. Constraints from helioseismic measurements have been applied to models that have resulted in improved agreement between model predictions and measurements. Topics which merit additional investigation remain, including helium and heavy element transport through the Sun, and the role played by differential rotation between interior and exterior regions, as well as between polar and equatorial regions of the exterior. The evidence is strong, however, that the factor of two disagreement between theoretical and measured neutrino fluxes cannot be overcome through modifications to the standard solar model.

Solar neutrino measurements have been primarily sensitive to ν_e . The evidence from atmospheric neutrino observations indicates that neutrino flavor may change with time, according to a simple quantum mechanical treatment, vacuum oscillations. The possibility that neutrino oscillations play a significant role in the solar neutrino problem requires measurements of all solar neutrino flavors. The first facility to provide a model-independent measurement will be the Sudbury Neutrino Observatory.

3. The Sudbury Neutrino Observatory

Deuterium provides two interactions for solar neutrino observation:

$$\nu_x + d \rightarrow \nu'_x + p + n \quad (3.1)$$

$$\nu_e + d \rightarrow e^- + p + p. \quad (3.2)$$

The Sudbury Neutrino Observatory (SNO) will measure the total flux of ν_e , ν_μ and ν_τ arriving at the Earth from the Sun. The neutral-current resulting from the dissociation of deuterium, shown schematically in Eq. 3.1, provides a signal which is equally sensitive to all three neutrino flavors. The charged-current, Eq. 3.2, occurs only for ν_e . The ratio of neutral and charged-current fluxes is therefore a sensitive indicator of neutrino oscillations. A value of unity for the normalized fluxes would rule out oscillations as the solution for the solar neutrino problem, while a value clearly different from unity presents strong evidence for oscillations.

The elastic scattering of ν from e^- provides an additional signal, but the cross section is lower than those involving deuterium by more than an order of magnitude.

$$\nu_{e,\mu,\tau} + e^- \rightarrow \nu'_{e,\mu,\tau} + e^- \quad (3.3)$$

All three neutrino flavors may undergo elastic scattering from e^- , but not with equal contributions, which complicates the analysis.

The solar neutrino signal is so feeble (10–20 events per day) that every systematic uncertainty must be considered and minimized. The physical production, propagation and detection of Čerenkov light must be understood and correctly modelled by Monte Carlo. The interplay between electronics and data acquisition software must be scrutinized with the goal of achieving harmonious integration of these two systems. Backgrounds in the detector must be identified, quantified, verified, and finally, re-

moved during the analysis. Our goal is to perform an analysis of the solar neutrino data that will be compelling to expert and non-expert alike.

The Sudbury Neutrino Observatory is simply described as a heavy water (deuterium oxide, or D_2O) Čerenkov detector. It is also a complex assembly of interconnected laboratories. Technical issues related to the specific SNO sub-systems (light water, heavy water, electronics, *etc.*) are addressed in a paper to be published in Nuclear Instruments and Methods and the references contained therein [81]. This work provides a general detector overview. Specific consideration of Čerenkov light production and detection in SNO is made, followed by a description and discussion of steps taken to minimize backgrounds. The SNO weak interactions are presented and the anticipated detector response to solar neutrinos is described. An overview of coincidence energy calibration techniques are presented to close the chapter.

3.1 *The Physical Structure of SNO*

The process of constructing SNO is comparable to building a ship in a bottle. The bottle in question is located 2 kilometers beneath the surface of the Earth, in the Creighton Nickel mine operated by INCO, Ltd of Sudbury, Ontario, Canada. The experimental site was excavated by INCO in the shape of a barrel, 33 m in height and 22 m in width at the waist. All materials used to build the detector were delivered to that depth through the Creighton #9 mine shaft. The lift cage is approximately $4 \times 2 \times 3$ meters (length \times width \times height), therefore great care was required in the planning of construction to allow the assembly of structures many meters in size.

The laboratory is at the extreme end of the SNO drift¹ on the 6800 foot level (Figure 3.1). A steel bulkhead seals the laboratory from the drift. Three drifts exist inside the laboratory. The first includes showers and changing rooms to ensure that

¹Drift is the technical mining term for a level tunnel.

those who enter the laboratory do not track mine dust into the experimental area. The second contains the water handling facilities. The third provides access to the detector cavity, and serves as a detector control room. The cavity is divided into upper and lower regions by a deck suspended on girders. The vast lower region houses the D_2O and components to detect Čerenkov light, while all equipment to operate the detector is housed either on deck or in the adjoining underground lab. Redundant equipment for running the detector is located above ground at the Creighton mine site.

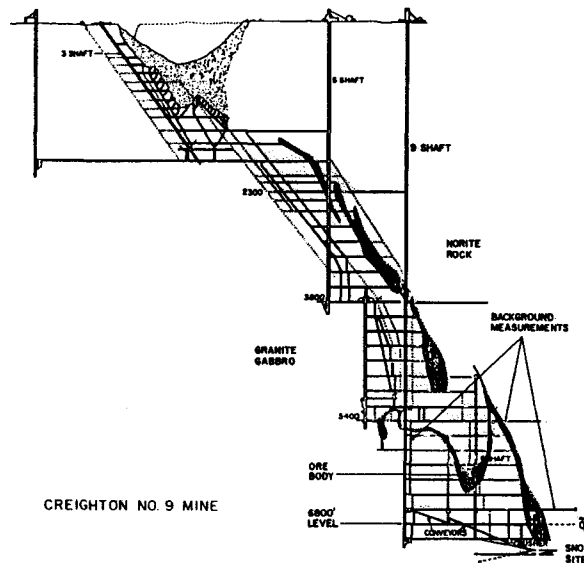


Figure 3.1: Diagram depicting the underground laboratory location within the Creighton mine. The shielding by 6800 feet of material reduces the cosmic ray induced muon flux to 100 per day.

3.1.1 Heavy Water Containment: The Acrylic Vessel

The lifeblood of SNO is heavy water. One thousand forty-six metric tons of deuterium oxide, loaned to SNO by the Canadian Federal government, were delivered from the Bruce Nuclear Generating Station operated by Ontario Hydro. The D_2O is

99.92%-enriched in deuterium. Forty-three shipments by tractor-trailer were required. The D_2O was pumped from trucks into a holding tank on the surface, where the mass was verified and where samples were assayed for ions, particulates, radioactive contaminants and isotopic enrichment. Only with these assurances was the D_2O deemed fit to be introduced to the detector. Six 3-ton rail cars were used to ferry the D_2O to the underground laboratory. Nearly 350 rail car loads were necessary to complete the transfer.

In other water Čerenkov detectors, the light water region is physically continuous, but in the analysis it is separated into two regions: the fiducial and shielding volumes. The former is defined as the region with the minimum radioactive backgrounds. D_2O is not appropriate for shielding due to the low threshold energy for deuterium dissociation and the subsequent background events due to neutron capture. These factors, as well as the extremely high cost of D_2O , necessitate the use of light water for radiation shielding.

An artist's depiction of the SNO laboratory is shown in Figure 3.2. A spherical acrylic vessel (AV) separates the heavy and light water. The AV has a 6-meter radius, and the wall is 5 cm thick. It is supported from the deck by ten fiber ropes which pass through grooves in acrylic panels affixed at the AV equator. Ropes were selected as the material with lowest possible radioactive contamination suitable for supporting the AV. A long vertical cylinder of acrylic (chimney) allows access from the deck to the D_2O inside the AV. This is essential for deployment of calibration sources, and for future deployment of neutron detection instrumentation into the D_2O volume.

The acrylic vessel was constructed using 122 preformed panels. The ultraviolet transmitting (UVT) acrylic was selected to match both the Čerenkov light production spectrum and the PMT spectral response. In addition, the acrylic may be produced with a low content of radioactive impurities. The panels were bonded in the underground laboratory, initially to form horizontal ring segments of the sphere. The

horizontal segments were then aligned and joined. The bonding process involved a liquid monomer which was poured into narrow spaces between adjacent panels. The process is exothermic, resulting from the breaking of the monomer chemical bonds, with the released heat fusing the two acrylic polymer panels. The completed acrylic vessel, including chimney, is a contiguous polymeric structure weighing 32.5 metric tons.

3.1.2 PMT Support Structure

A stainless steel geodesic (a three-frequency icosahedron) PMT support structure (PSUP) surrounds the AV. The PSUP was designed by the SNO group at Lawrence Berkeley National Laboratory and manufactured in the San Francisco Bay area by Donal Machine of Petaluma, California. The PSUP diameter is 17 meters. Stainless steel tubing was selected to minimize leaching of radioactive contaminants into the light water. The tube wall thickness was selected to minimize mass while also providing a rigid structure. The upper hemisphere was assembled on a platform, lifted into place, suspended from the deck and then PMT panels were installed. This structure remained incomplete for two years while the acrylic vessel was assembled. Construction resumed in a step-wise fashion, extending the framework toward the south pole and backfilling with PMT panels. The rigidity of the design was critical to allow the geodesic to be closed 30 months after assembly began. Engineering and design details concerning the PSUP may be found in [82].

3.1.3 Photomultiplier Tubes

SNO uses 9455 8" Hamamatsu R1408 PMTs [83] to monitor the D_2O volume. The majority of solar neutrino events will result in single photons impinging on individual PMTs. Single photon detection is a very demanding operating mode for large PMTs. All PMTs exhibit a dark current, or a signal in the absence of light. The main

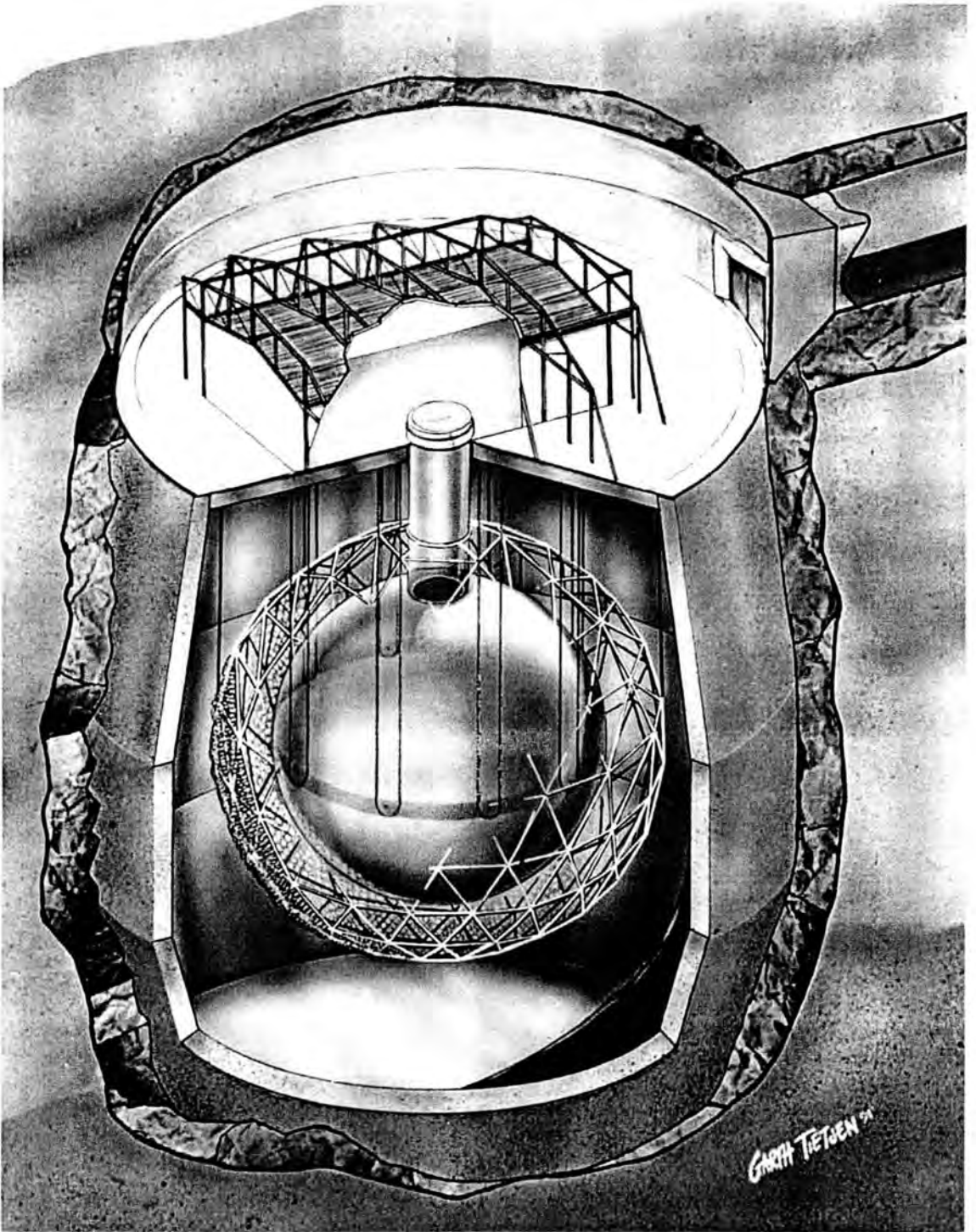


Figure 3.2: Artists depiction of the detector cavity.

contributions are thermal noise, leakage currents through the electrode supports, radioactive contamination, and ionization and light phenomenon. The ultrapure light water is cooled below 10°C to reduce thermal noise. The other four contributions are minimized through selection of materials and design.

The glass was produced by Schott Glaswerke in a melt dedicated to meet SNO's radioactivity requirements. These efforts reduced the radioactive uranium and thorium by nearly a factor of 10 compared to standard PMT glass. The photocathode provides 29% quantum efficiency. The anode stack is composed of 10 stages, providing 10^7 gain when operated in the range 1800-2300 volts. The PMTs are grouped in the high voltage racks according to common nominal operating voltage (see 3.2.1).

The PMTs provide 31% coverage by area of the 4π solid angle enclosing the D_2O . Each PMT is therefore housed in a hexagonal reflective cell, shown in Figure 3.3, both to increase the effective solid angle to 64%, and also to limit collection of light arriving at large angles relative to the longitudinal axis of the tube [112]. Flexible plastic strips coated with aluminium are used to enhance light collection at the PMT. The hexagonal cells are assembled into panels comprised of 7, 10, 14, 19 or 21 members. The set of panel configurations was determined to maximize the total number of PMTs in the PSUP (an example region is depicted in Figure 3.3).

The panels are mounted on the PSUP steel with a combination of fixed and telescoping mounts, which allow for panel alignment with the center of the detector. A diode laser was temporarily affixed normal to the panel face. Telescoping mounts were lengthened or shortened until the laser dot fell on a 3" spherical target suspended at the center of the PSUP. Again, it was essential that the incomplete PSUP be a very rigid structure to allow for upper hemisphere panel alignment.

Finally, there are 91 outward looking (OWL) PMTs that are used to veto high-energy events which produce light outside as well as inside the PMT array. Such high-energy events are due to cosmic ray induced muons. These tubes are not placed in cells

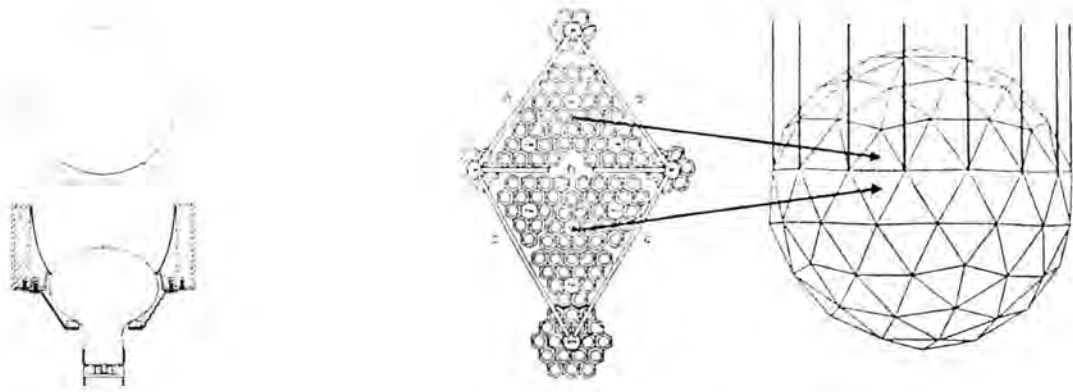


Figure 3.3: The SNO PMT reflector and hexagonal cell panels. Left: PMT reflector front view (top) and profile (bottom). Right: Panels composed of hexagonal reflector cells and their location on the PSUP.

to enhance sensitivity to all available light. The veto signal allows for discrimination between muons that pass through the detector and those that stop inside the PMT array.

3.1.4 Water Handling Facilities

Two separate systems are required for handling water at SNO: heavy water and ultrapure light water. The D_2O handling systems are designed to maintain the high isotopic purity and to establish the low radioactive content which is required for SNO. Each shipment is assayed upon initial receipt to ensure it meets the criteria listed in Table 3.1. These criteria are to avoid degrading heavy water already on site. For instance, there is no facility for improving the isotopic purity on site, therefore any delivery below 99.93% enrichment dilutes the entire SNO D_2O volume irreversibly. The final shipment was received in early March 1999.

A suite of intensive assay measurements for radioactive content is performed in the underground laboratory. Filtering is accomplished using ion exchange and reverse osmosis techniques. Unique methods have been developed to detect decay products

Criteria	Limits
D ₂ O Enrichment	≥ 99.93%
pH	6.0-8.0
Particulates	ppb

Table 3.1: Criteria for D₂O acceptance at SNO.

from these chains in quantities at the 10^{-14} g/g level². More detail will be provided in the discussion on backgrounds in Section 3.3.2.3.

The H₂O arrives at the laboratory directly from the local water supply, albeit following a 6800-foot free fall within the Creighton Mine underground water main. Degassing takes place in an initial holding tank, to allow gases which mixed with the water to be eliminated. Charcoal and sand filtration removes additional adsorbed gases. Many techniques from D₂O radioactive assay carry over to the H₂O system. While tolerances for impurities are higher due to the ability to remove H₂O backgrounds in the analysis, the techniques for removing uranium and thorium decay chain products have been demonstrated to exceed the design goals (10^{-13} g/g) by nearly a factor of ten. Radon removal has been tested on small samples (100 liters) and will be tested in earnest when the fill is complete and the deck is sealed against air exchange with the laboratory.

Eliminating biological activity in both H₂O and D₂O is a priority goal for water treatment. Preventing biologic growth will keep the PMTs free of material which would decrease light collection. In addition, transmission lengths for optical photons in water are very sensitive to the presence of microbes. Four techniques are employed to mitigate against creating biology:

- The molecular and atomic oxygen content is reduced through the degassing process.

²The designation g/g refers to grams of contaminant per gram bulk material

- The water is cooled below 10°C.
- Water is removed from the cavity and sterilized by application of ultraviolet light prior to reintroduction to the cavity.
- The cavity will be sealed against air from the laboratory. Nitrogen gas will be used to flush air from the area between the deck bottom and water surface to further reduce the biologic risk to the experiment.

It is believed that these techniques will mitigate optical degradation for the ten-year expected experimental lifetime.

3.1.5 Electronics and Data Acquisition

The tasks of providing a stable high voltage supply and reading out the signal from the PMTs are accomplished using distinct circuit board sets. They are collectively referred to as the high voltage and readout electronics, respectively. Their components are also identified using separate nomenclatures, so that one may refer to a particular PMT by either noting the crate/slot/paddlecard (high voltage) or by a unique crate/card/channel (readout). The top level of high voltage control is the crate, which supports up to 512 PMTs. The lowest level is the paddlecard, which provides power to eight PMTs. Readout is accomplished for each PMT individually.

Electronics hardware is located on the perimeter of the deck, and is distributed amongst 19 crates. Each crate holds 16 cards, and each card supports 32 channels. There are 9728 primary channels available. In addition to the 9637 channels required for the PMTs (primary and OWLs), 49 are used to monitor the low gain output on dual port PMTs, 8 are devoted to calibration sources and 33 are spare channels.

Data acquisition involves sequential readout of SNO crates and the channels therein. The binary data is then sorted into events and translated into the proper format for offline analysis. Low-level monitoring provides information concerning read and write

errors and the means to intervene in response. High-level monitoring is available for on-site and remote clients from a process called the Dispatcher. Data may be considered in raw, pre-event or event form. If the data stream output is too high, as may be the case during calibrations, the Dispatcher converts to a sampling mode. A variety of tools has been developed to allow analysis on both UNIX and Macintosh machines, including graphical event displays.

3.2 Production and Detection of Čerenkov Light

The emission of light caused by the passage of high-energy charged particles through a medium with a velocity greater than that of light in the medium is known as the Čerenkov effect [28, 29, 30, 25]. In the case of SNO, the medium is water (H₂O and D₂O) or acrylic and the light predominantly ultraviolet. Rearranging the formula for relativistic energy provides the minimum kinetic energy, KE_{min} , required for a particle's velocity, v , to exceed the speed of light in water, we find

$$KE_{min} = mc^2 \left(\sqrt{\frac{1}{1 - v^2/c^2}} - 1 \right). \quad (3.4)$$

Substitute $v = c/n$, where n is the material's index of refraction, to establish the condition for minimum kinetic energy.

The minimum kinetic energy increases with particle mass, m . The particle speed and speed of light in vacuo are v and c , respectively. The value for an e^- , a μ^+ , a p^+ , a d^+ and an $^{16}\text{O}^+$ nucleus are given in Table 3.2. Solar neutrino energies can lead to Čerenkov light production only by electrons. Cosmic ray muons, however, will arrive in the SNO cavity at the rate of a few per hour and a typical energy is 1-10 GeV. There is no effective upper limit to this energy spectrum that limits Čerenkov light production. It is therefore prudent to study the Čerenkov light production by more massive charged particles than e^- , to be well equipped for their identification and removal through analysis.

Particle	KE_{min} (MeV)
e^-	0.262
μ^+	53.23
p^+	480.3
d^\pm	960.0
$^{16}\text{O}^+$	7626

Table 3.2: Particles with distinct masses, unit charge, and their Čerenkov light production threshold.

The number of photons produced due to the Čerenkov effect depends on particle charge Z , speed $\beta = v/c$, and linear distance travelled above the Čerenkov threshold L . Eq. 3.5 displays the wavelength dependence of Čerenkov light production.

$$\frac{dN_\gamma}{dL} = 2\pi\alpha Z^2 \int_{\lambda_1}^{\lambda_2} \left(1 - \frac{1}{\beta^2 n^2}\right) d\lambda/\lambda^2 \quad (3.5)$$

The number of Čerenkov photons, dN_γ , produced per unit path length, dL , by the particles listed in Table 3.2 is about 280 photons per cm. The electric charge of the particle is Z , the integral is calculated for optical wavelengths ($\lambda_1 = 350$ nm and $\lambda_2 = 650$ nm) and the index of refraction for water is n . A 0.5-GeV μ and a 5.0-MeV e^- will create an equal number of photons *per centimeter path length*. Therefore, if a μ enters SNO, it will generate much more light than an e^- due to the longer path length (meters vs. centimeters) and it will be clearly distinguished from the e^- event. Any shower particles in prompt (high-energy e^-) or delayed (neutron capture) coincidence with the μ will also be distinguished from solar neutrino events.

3.2.1 PMT Response to Čerenkov Light

The number of photons per unit path length of the radiating particle is described by Eq. 3.5. Čerenkov light is produced preferentially with short wavelengths. The PMT frequency response was selected for enhanced sensitivity to Čerenkov light.

PMT acceptance testing was performed at Queen's University [84]. The PMTs were individually checked using a calibrated Čerenkov light source to verify the frequency response, the quantum efficiency and the high voltage required to achieve 10^7 gain. These tests accepted about 2/3 of PMTs produced for consideration by SNO, and established five nominal high voltage classifications used to group PMTs into common high voltage supply crates (3.1.2).

3.2.2 Optical Transmission Properties of SNO

Ideally, the acrylic vessel, D_2O and H_2O would be perfectly transmitting for ultraviolet photons. As this is not the case, it is important to quantify the transmission probability, and to determine if there are spatial variations. Spatial variation will be due to the presence of bonds between panels and the ten anchor panels³ spaced around the equator which are used to suspend the acrylic vessel. Three optical calibration sources are intended to directly measure these effects.

A nitrogen dye laser is coupled to a small diffusion sphere via an optical fiber [87]. The sphere is lowered into the acrylic vessel, where laser pulses illuminate all PMTs. The laser pulse has a 2 nsec width. The beam is split above deck and the pulse intensity is monitored to study pulse to pulse intensity variations. The light emission uniformity into 4π is well characterised. Non-uniformity in the PMT illumination pattern will be studied to indicate AV non-uniformities.

The relative times of PMT signals within an individual event are used to study light reflected from detector surfaces. The ideal source would emit light on a time scale short compared to the PMT time resolution. The sonoluminescence process provides such a source for SNO [88]. Emission occurs on a picosecond time scale, much shorter than the nanosecond uncertainty in PMT timing based on the variable transit time from photocathode to first dynode segment. The major uncertainties for

³Colloquially known as belly plates

analyzing sonoluminescence data arise from the stability of the light intensity from the source and in characterising the light emission uniformity. Both characteristics were studied during the dry detector runs conducted in 1998. This analysis is ongoing.

Six light emitting diodes (LEDS) enclosed in stainless steel tubes are mounted on the PSUP and directed toward the center of the AV [89]. They produce a spectrum with 480 nm average wavelength. These sources are very simple to operate, and will be used to monitor changes in optical conditions. The pulse widths are ~ 4 ns, which allows for some study of reflections from optical boundaries at the AV. These sources are directional in nature and are therefore not ideally suited to assessing AV optical non-uniformities. They have proved useful in determining the PSUP and AV relative location.

Calibrations using these sources have been performed in air and will be performed in water. The data in air provide another handle to distinguish effects due to the AV, which are enhanced by the larger change in refractive index between air and acrylic. The sonoluminescence source provides the timing required to separate AV reflection effects from transmission and absorption properties. Measurements with both sources in the D_2O and in the H_2O outside the AV also enhance our capabilities for optical calibration analysis.

3.3 Backgrounds

Understanding the background events is crucial to the success of SNO. Radioactivity intrinsic to the SNO cavity, radioactive contamination of detector components and muons from cosmic ray interactions in the atmosphere account for all significant background events. The background has two effects: The low-energy threshold is dependent on the background rate, and, some background events will have the same characteristics as solar neutrino events. The latter effect emphasizes the importance of minimizing radioactivity in the heavy water and acrylic vessel.

The effort to reduce the radioactive content of every component of the detector has been extraordinary. Sample materials were counted for levels of ^{238}U , ^{232}Th and ^{40}K and strict guidelines were enforced regulating the final choice of materials. Clean room protocols have been adhered to for component subassembly off-site. The underground laboratory itself has operated as a class 10000 clean room⁴ since 1995.

Additional background reduction will result from data analysis. Individual events and classes of events may be identified due to PMT hit pattern and timing studies. The Čerenkov cone vertex location may be identified and used to remove events originating outside the acrylic vessel. The ultimate test of our efforts lie ahead: demonstrating the low backgrounds relative to the solar neutrino data.

3.3.1 Cosmic Rays

The relativistic nuclear debris of stellar death continually collide with ions and atoms high in the Earth's atmosphere. These cosmic ray particles, which are primarily protons, result in showers of charged particles and electromagnetic radiation that rain down upon the surface of the Earth. Many shower particles are sufficiently energetic to penetrate meters of concrete, water or soil. A particularly penetrating constituent of the showers is muons. Scientists seeking faint neutrino signals must retreat far beneath the Earth's surface to sufficiently reduce the muon flux.

SNO is very well shielded from muons by a minimum overburden ≥ 5000 meters water equivalent⁵. The expected muon rate is a few per hour, and this figure was confirmed by experiments for the empty detector during 1998. A muon which penetrates to this depth has very large energy and is unlikely to stop inside the SNO D_2O volume. The outward looking PMT array on the PSUP will observe Čerenkov light in the outer detector volume caused by the passage of muons. This signal will

⁴Clean room designations denote the number of particles per cubic foot of air exceeding 0.3 micron in size.

⁵For comparison, the overburden for an underground laboratory is determined as an equivalent depth of water. The composition of local materials is assessed for the comparison.

be coincident with a large signal from the main SNO array in the event that a muon passes through the detector. The coincident signals will clearly identify muon events. In the unlikely event that a muon stops inside the detector, the light output will be high and well described by a cone due to the small deflections of the muon by electrons in the D_2O .

3.3.2 Radioactive Contamination

There are two mechanisms by which radioactive contaminants create signals in SNO. First is the Čerenkov light produced by β -particle and/or γ -ray interactions in the light water and heavy water. Secondly, γ -rays with sufficient energy to photodisintegrate deuterium (greater than 2.224 MeV) lead to free neutrons in the heavy water. These neutrons are then indistinguishable from neutrons produced via the neutral-current reaction, because there is no means to determine neutron energy or direction. Therefore maximum acceptable levels of ^{238}U and ^{232}Th have been established to keep backgrounds from neutrons at or below 10% of the expected neutral-current, or fewer than one each day.

3.3.2.1 SNO Cavity

The underground cavity housing SNO was created by INCO, Ltd. expressly for the purpose of this experiment. The natural abundance of ^{238}U and ^{232}Th in the rock was measured to be 1.5×10^{-6} g/g and 4×10^{-6} g/g, respectively. There is no possibility of reducing the radioactive abundance of the rock; however, the flux of γ -rays can be reduced through shielding. The bare rock cavity walls were covered with a reduced activity concrete to keep dust from the walls out of the water. A urylon lining to block radon diffusion through the concrete was applied to the wall surface. The radon flux will be reduced to approximately 2×10^{-7} of the unshielded value. Additionally, the light water in the outer detector attenuates most of the γ -ray

and neutron flux. Those which penetrate the PSUP are very unlikely to also enter the AV, therefore if our analysis tools locate these events to occur outside of the AV, these background events will be eliminated.

A series of measurements to determine the γ -ray and neutron flux near the floor of the cavity was performed during 1995 and 1996 by Isaac *et al.* [90]. A large-volume, cylindrical NaI(Tl) detector (15 cm height by 19 cm diameter) was placed on the cavity floor after the concrete layer had been put in place. Data were accumulated for 62 days. The NaI detector was moved to another laboratory in the 4600 level of the mine for a series of calibration measurements to aid determination of the neutron flux at the 6800 level laboratory. This data is used with the SNOMAN simulation to assess the success of the light water shielding. Plots representing the net γ -ray flux at the 4600- and 6800-foot levels are shown in Figure 3.4. The uncertainty in the net measurement at the 6800-foot level is very poor for γ -ray energy above 8 MeV.

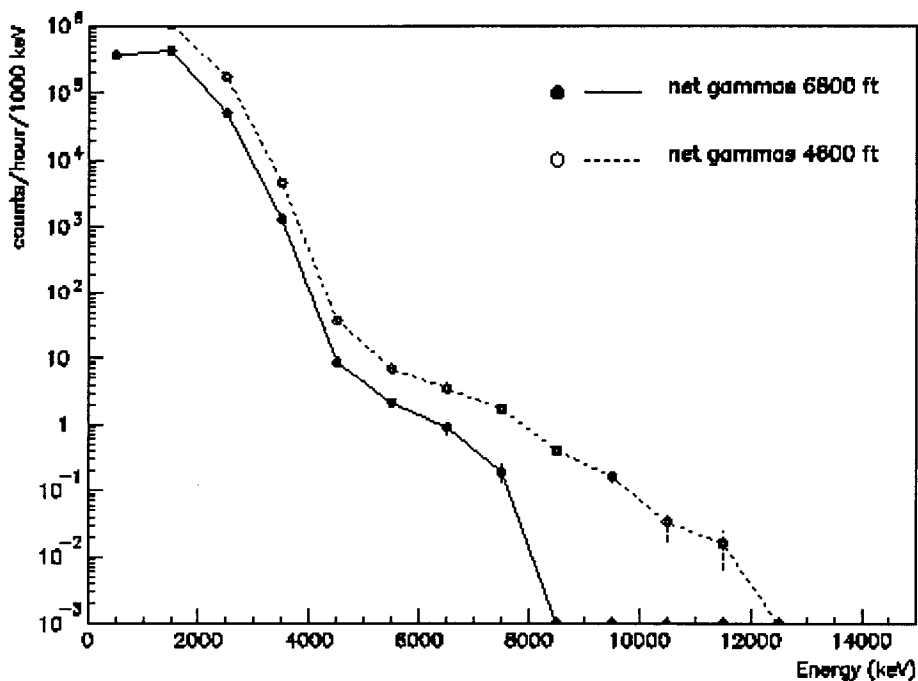


Figure 3.4: The net γ -ray energy spectrum observed in the SNO cavity at the 6800-foot level and in the laboratory at the 4600-foot level.

Additionally, Isaac *et al.* report on analysis that compared the data obtained with the NaI(Tl) detector with data taken prior to lining the cavity walls with low-radioactivity shotcrete. The purpose was to quantify the reduction of the γ -ray flux below 3 MeV due to the application of the 20-cm thick shotcrete shielding. Their result showed a reduction in the flux by a factor of two.

3.3.2.2 PMT Support Structure

The PSUP is a major source of background due to radioactive contamination by uranium and thorium. The radioactive content of the stainless steel components was counted at the Low Background Counting Facility at Lawrence Berkeley National Laboratory (LBNL). All samples were below the 15 ppb⁶ allowable upper limit. The effect of the PSUP background γ -rays is enhanced by their proximity to the PMTs. The light water shielding will not eliminate light from this class of background, but will greatly reduce events producing Čerenkov light within the AV. Analysis techniques will be useful, but cannot be applied to the lower energy events. The low-energy threshold is determined in part by the PSUP backgrounds.

Analysis efforts to employ neural network pattern recognition seek to reduce the energy threshold by distinguishing the PSUP backgrounds from solar neutrino signals [91]. The PSUP background events will produce Čerenkov light outside of the AV. While not applicable on an event by event basis, this technique shows promise to lower the energy threshold to 4 MeV [92].

3.3.2.3 The Acrylic Vessel and Heavy Water

The heavy water region is the most sensitive to radioactive contamination. The criteria for impurities are therefore the most stringent: 3×10^{-15} g/g thorium and 4.5×10^{-14} g/g uranium. There is no shielding benefit for background events in this

⁶ppb = parts per 10⁹.

region. The low-energy threshold is largely determined by the radioactivity in the heavy water. Analysis techniques which can distinguish low-energy background from low-energy neutrino events are being explored, but the expected low-energy threshold for SNO is 5 MeV recoil-electron energy.

3.4 SNO Weak Interactions

H. Chen was the first to suggest that solar neutrino interactions in D_2O could address the solar neutrino problem [93]. Chen proposed measuring the photodisintegration rate of deuterium to obtain the total neutrino flux from the Sun. The charged-current interaction would provide an unambiguous measure of the ν_e flux without the uncertainties associated with extracting such a measurement from ν - e^- elastic scattering. The challenge is to identify the few solar neutrino events from amongst the vast background seen by a D_2O detector.

3.4.1 Neutral-Current Detection

The neutral-current interaction has a 2.2-MeV threshold, equal to the deuteron binding energy. The interaction is mediated by exchange of the neutral gauge boson, Z^0 , allowing all three neutrino flavors to participate. Detecting the neutral-current

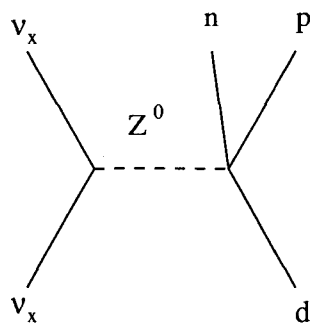


Figure 3.5: The SNO weak neutral-current interaction on deuterium represented as a Feynman diagram.

is complicated by the lack of relativistic charged particles in the final state. In pure D_2O , the signal arises from thermal neutron capture on deuterium. As a result no information about the neutrino energy or direction is accessible. Additionally, the high energy of the final-state neutron leads to a mean time before neutron capture of 32 msec. A 6.25-MeV γ -ray will generate one or more e^- that will produce Čerenkov light⁷. The efficiency for neutron detection is poor because neutrons travel large distances in D_2O prior to becoming captured. In fact, over 50% of neutrons generated isotropically in the D_2O volume will migrate outside the AV and be captured on protons in the H_2O . Finally, the Nhit distribution resulting from these γ -rays will significantly overlap the 5-MeV threshold, reducing the detection efficiency below 20%. Other methods to detect the neutral-current have been developed to overcome these difficulties.

3.4.1.1 Salty D_2O

The addition of the inorganic salt $MgCl_2$ to the heavy water to enhance neutral-current detection efficiency [96] is planned. Neutron capture on ^{35}Cl releases 8.6 MeV in a γ -ray cascade, increasing the amount of Čerenkov light released per neutron capture event above the 5-MeV threshold in most cases. The much higher cross section for neutron capture and the reduced neutron range leads to an expected detection efficiency of 89%. High efficiency removal of $MgCl_2$ from heavy water has been demonstrated using the same reverse osmosis processes employed in the initial heavy water preparation.

⁷Thermal neutron capture on ^{16}O is lower by a factor of ten (abundance and cross-section) and results in 4.1 MeV of γ -ray energy, below the expected low-energy threshold.

3.4.1.2 Neutral-Current Detectors

An independent measurement will be made using an array of segmented ${}^3\text{He}$ proportional counters [97]. The neutron capture reaction is shown in Eq. 3.6.



Pulse shape discrimination on the final state charged particles will be used to identify individual events. The 5.08-cm diameter tubes are made of nickel produced by chemical vapor deposition to minimize radioactive backgrounds. The total counter length will be 750 meters spread amongst 96 strings arranged on a one-meter grid. The efficiency from this strategy is expected to be 45%. The array is expected to decrease the Čerenkov light yield for charged-current detection by 11%.

3.4.2 Charged-Current Detection

The goal of the charged-current detection is to measure the ν_e energy spectrum from ${}^8\text{B}$ decay. The identification of charged-current events relies on observing PMT patterns consistent with Čerenkov light creation within the D_2O . The interaction, which is displayed as a Feynman diagram in Figure 3.6, has a 1.44-MeV threshold,

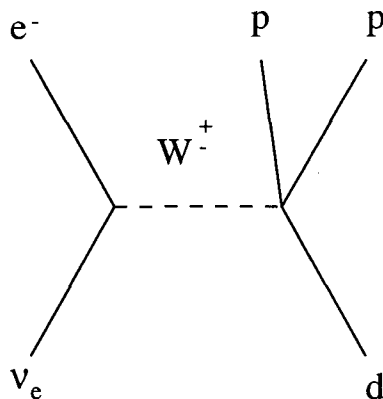


Figure 3.6: The SNO charged-current weak interaction on deuterium.

and the e^- will carry most of the ν_e energy in the final state. The charged-current interaction is mediated by the charged gauge bosons, W^\pm , restricting participation to ν_e . The lowest energy ${}^8\text{B}$ neutrinos which SNO measures will be approximately 6.44 MeV, because it is the e^- kinetic energy which must exceed the detector threshold.

The reaction is a pure Gamow-Teller transition, which means that the e^- direction relative to that of the initial ν_e is well approximated by $1 - \frac{1}{3}\cos(\theta)$ [95]. While this relationship cannot be applied to individual events, it provides a check on the analysis results for the charged-current event class.

3.4.3 Elastic Scattering in SNO

Electron-neutrino elastic scattering is a third interaction available to SNO. There are both neutral- and charged-current interactions, which are depicted in Figure 3.7, involving all neutrino flavors and ν_e only, respectively.

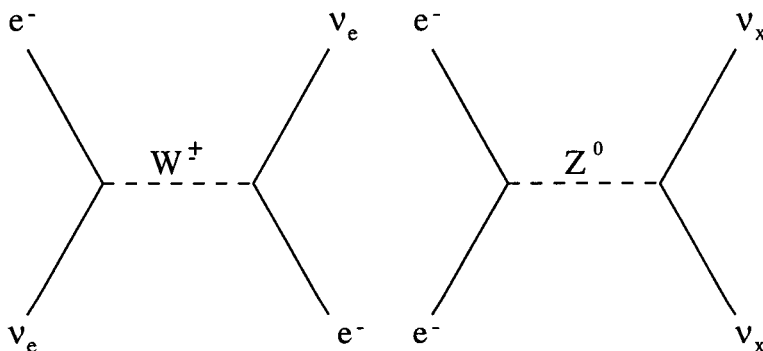


Figure 3.7: Elastic scattering between electrons and neutrinos features neutral- and charged-current interactions for ν_e , and only neutral-current interactions for ν_μ and ν_τ .

The anticipated event rate is one per day, suggesting the possibility of up to 80 ν_μ or ν_τ scattering events after one year. The difficulty will be to prove that any excess in the number of elastic scattering events is not exclusively due to ν_e .

3.4.4 Interpretation

The capability to measure the total solar neutrino flux, independent of neutrino flavor, is the unique characteristic of SNO. Therefore, the neutral-current measurement is of great interest to the physics community. The normalized charged- to neutral-current ratio (CC/NC) will provide an unambiguous determination for or against neutrino oscillations as a solution to the solar neutrino problem. Oscillations would lead to a ratio less than unity, while the ratio in the absence of oscillations would be unity. Further, two- and three-flavor maximal mixing would lead to different ratios, $\frac{1}{2}$ for the former, and $\frac{1}{3}$ for the latter.

The charged-current recoil-electron spectral shape will be of interest in the event that neutrino oscillations are indicated by the CC/NC ratio result. Neutrino oscillations are an energy dependent mechanism which will alter the charged-current spectral shape. Specific oscillation mechanisms may be deduced from comparing the observed shape with that predicted for the recoil electron from laboratory measurements.

The electron-neutrino elastic scattering interaction may prove useful for SNO in spite of anticipated poor statistics [98, 99, 100]. The primary importance is that it provides an estimate of the neutral-current during the pure D₂O run. Eq. 3.3 features ν_e , but also samples from the possible flux of ν_μ and ν_τ in the approximate ratio 7:1:1. These events will be strongly correlated with the Sun's location, and will be separable from the charged-current events. Each process allows an independent solar neutrino flux determination. The solar neutrino signals in SNO are summarized in Table 3.3, along with the expected event rate.

3.5 *Response of SNO to Solar Neutrinos*

Two categories of solar neutrino events have been identified for SNO. Charged-current and elastic scattering events are observed by detecting the Čerenkov light produced by scattered electrons. Neutral-current events produce free neutrons, which

Interaction		Rate (day ⁻¹)
Charged-current	$\nu_e + d \rightarrow e^- + p + p$	10
Neutral-current	$\nu_x + d \rightarrow \nu'_x + p + n$	10
Elastic Scattering	$\nu_{e,\mu,\tau} + e^- \rightarrow \nu'_{e,\mu,\tau} + e^-$	1

Table 3.3: The solar neutrino interactions in SNO and their expected detection rate.

may be detected either by γ -ray emission following capture on nuclei in the heavy water, or by detection using a neutron detector array. In either case, the simulation of the detector and its response to relativistic electrons and free neutrons plays a major role in understanding how to address data analysis issues. An overview of the SNO Monte Carlo program is provided along with sample responses to charged-current, neutral-current and background event classes. The reader is again referred to the SNO review paper [81] for additional detail and references.

3.5.1 SNO Monte Carlo Simulation and Analysis

Monte Carlo simulation and analysis for SNO is carried out using the FORTRAN code SNOMAN. This code simulates how the detector influences Čerenkov light production, propagation and detection. In addition, data from the detector may be analysed for PMT hit patterns arising from solar neutrino interactions and backgrounds. This analysis provides the position and direction from which the Čerenkov light was produced.

Three software packages developed at the European Center for Nuclear Research (CERN) for high-energy physics analysis have been incorporated into SNOMAN. Memory management is handled by ZEBRA to make up for the static memory allocation deficiencies of standard FORTRAN.

The accurate representation of electron interactions in matter is essential for a successful simulation. The Electron and Gamma-Ray Shower 4 (EGS4) package [85],

initially developed at the Stanford Linear Accelerator Center (SLAC) and now widely used to model low-energy radiation transport, is used to describe electron- γ -ray showers resulting from solar neutrino interactions. Neutron propagation and interactions are described by the Monte Carlo Neutron Program (MCNP) developed at Los Alamos National Laboratory and currently maintained by Oak Ridge National Laboratory [121].

3.5.2 SNOMAN Simulated Response

The simulated response to 8-MeV electrons is shown in the left panel of Figure 3.8 to illustrate the SNO energy resolution in terms of number of PMTs in an event (N_{hit}) at the approximate midpoint of the solar neutrino energy spectrum. The simulation features 100,000 electron events, generated at the center of the D_2O with randomly determined directions. The mean N_{hit} is 68.44 with a FWHM of 9.967. The N_{hit} resolution is 14.5%. Assuming a linear relation, this calculation predicts 8.5 N_{hit} per MeV electron energy. The relation between neutrino energy, E_ν , and recoil-electron energy, E_{e^-} , is well defined for charged-current events. Once the N_{hit} vs electron energy relation has been established, the association of N_{hit} for an event leads to an estimated E_ν which carries uncertainties related to the detector resolution and the energy calibration uncertainty.

A second simulation featuring 100,000 8-MeV electrons distributed uniformly in the D_2O volume is displayed in the right panel of Figure 3.8. This situation mimics the geometry that applies to solar neutrino events, which will be similarly distributed. The spectra are in very close agreement, suggesting that calibration using a source at the detector center may be applied to analyses considering data independent of Čerenkov light production position. Unfortunately, the result cannot be directly verified, as it would require mixing radioactive material into the D_2O . A reasonable approximation may be obtained by combining all the positional calibration data.

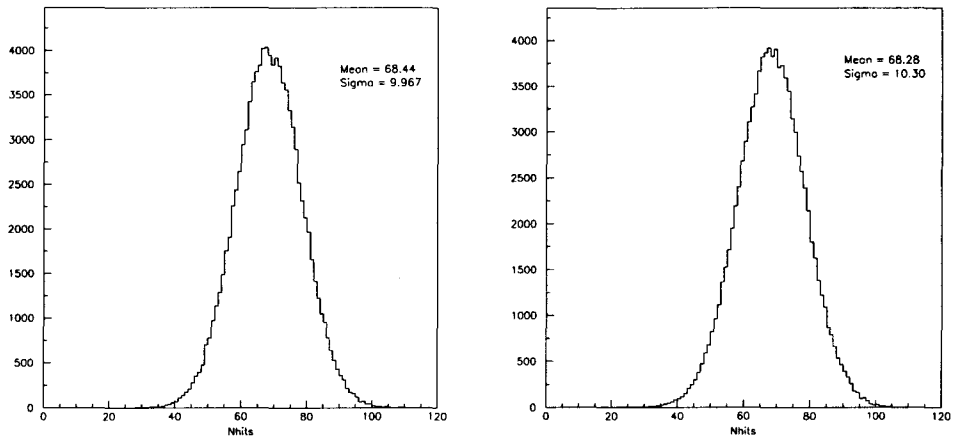


Figure 3.8: Simulated SNO response to 100,000 8-MeV electrons. Left: All events originate from the center of the D_2O volume. Right: Events originate uniformly throughout the D_2O volume.

The detector simulation will be refined as optical and energy calibrations are conducted. The simple parameterisation $E_{e^-} = f(Nhit)$ will be modified by placing cuts on the PMT timing, and considering the amount of charge collected by various PMTs in an event. Anisotropy in the optical response will lead to adjustments based on Čerenkov event vertex location and direction.

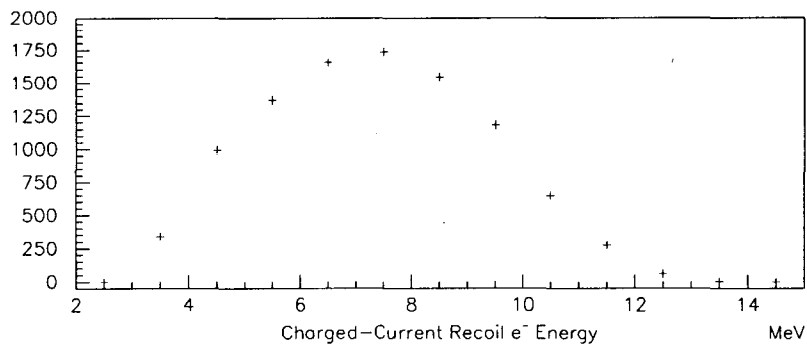


Figure 3.9: Simulated SNO response to 10,000 charged-current interactions.

The simulated Nhit spectrum from 10,000 charged-current interactions is shown in Figure 3.9. The neutrino interaction is not explicitly simulated. The recoil-electron energies are sampled from a weighted distribution appropriate for the SNO charged-current interaction. The minimum energy for simulated electrons was selected as 3.0 MeV, significantly below the low-energy threshold. The spectrum displays a shape consistent with an allowed β^+ decay.

Neutral-current simulations are compared for neutron capture signals arising from D_2O and $MgCl_2$ in D_2O . The neutrons are produced isotropically in the acrylic vessel according to the neutral-current energy spectrum. The top panel of Figure 3.10 shows the simulated Nhit spectra above a 10 Nhit cutoff, while the lower panels show the simulated radial distribution of the neutron capture events. The addition of $MgCl_2$ enhances the Nhit output per event, and leads to far more neutrons captured in the D_2O volume.

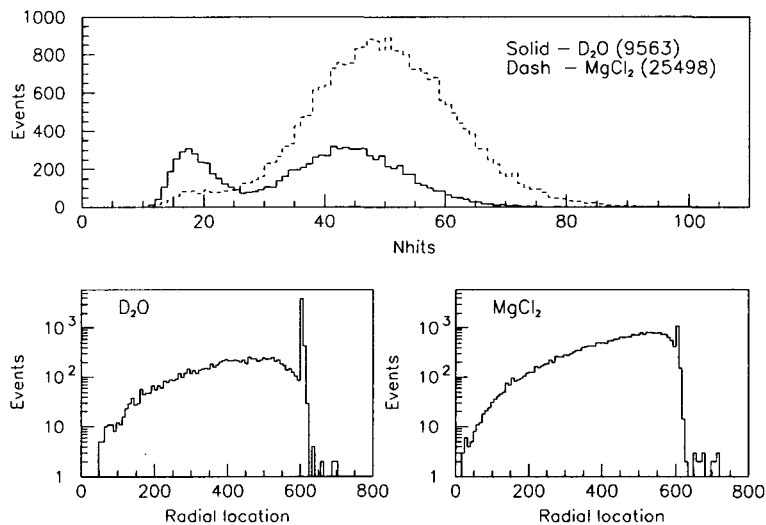


Figure 3.10: Simulated SNO response to 30,000 neutral-current interactions in D_2O and 2.5 metric tons $MgCl_2$ in D_2O . The Nhit spectra appear in the top panel, while the radial distance where the neutron capture occurred is plotted separately below.

3.5.3 Sensitivity to Oscillation Parameters

Neutrino oscillations were considered in Sections 2.3.1 and 2.3.3. The charged-current spectral shape will be analyzed to deduce the oscillation mechanism. The predicted recoil-electron energy spectra for SNO appear in Figure 3.11 for the mechanisms and oscillation parameters defined in Table 3.4 (from [94]).

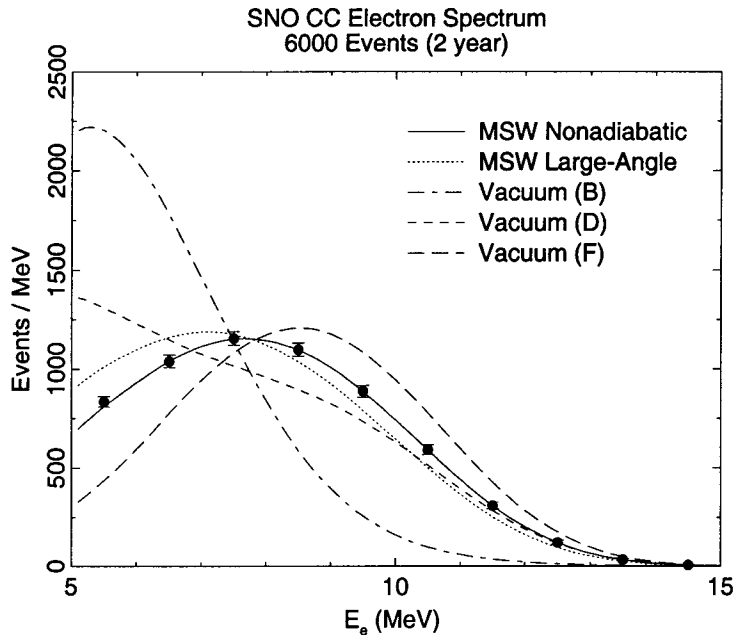


Figure 3.11: Simulated SNO response to charged-current spectrum for selected neutrino oscillation mechanisms and parameters (see Table 3.4).

The mechanisms and parameters selected are intended to illustrate the characteristics of the charged-current spectral shape. Consider the three vacuum oscillation spectra. The shapes vary greatly for small changes in the oscillation parameters. Consider next spectra F and the two MSW solutions. The spectral shape is similar. Deducing the spectral shape that best accounts for observed data providing this shape will clearly be dependant on the energy calibration uncertainties, and will be addressed in detail in later chapters.

Mechanism	$\delta m^2(\text{eV}^2)$	$\sin^2(2\theta)$
Vacuum B	1.0×10^{-10}	0.91
Vacuum D	7.8×10^{-11}	0.78
Vacuum F	5.2×10^{-11}	0.99
MSW Large Angle	1.6×10^{-5}	0.63
MSW Nonadiabatic	na	na

Table 3.4: Neutrino oscillation mechanisms with specific parameters which correspond to spectra plotted in Figure 3.11. The MSW Nonadiabatic solution has been ruled out by data obtained since the plot was generated.

3.6 Energy Calibration

It is essential that the relation between number of PMTs firing in an event and solar neutrino energy be well defined to minimize uncertainties in the analysis of charged-current and elastic scattering data. Neutral-current measurements will also benefit from a thorough energy calibration. SNO's high background threshold rules out the use of a high intensity neutrino source similar to those used by the gallium radiochemical experiments. The physical limitations of the SNO underground laboratory will not accommodate an electron linac. SNO will therefore be calibrated using sources which produce monoenergetic γ -rays.

The response of SNO to 8-MeV electrons was discussed in 3.5.2. The accuracy of the detector simulation will be crucial to apply the γ -ray calibration results to deduce the electron response of SNO. Figure 3.12 shows the simulated response for γ -rays and e^- in the range 2-14 MeV. The γ -ray response is clearly nonlinear below, and approximately linear above, 6 MeV. Calibration near the low-energy threshold is most effected by the non-linear response. Linear extrapolation in the region above 6 MeV will likely be reliable. Nevertheless, energy calibration must be performed over a range of γ -ray energies which encompasses the solar neutrino recoil-energy spectrum.

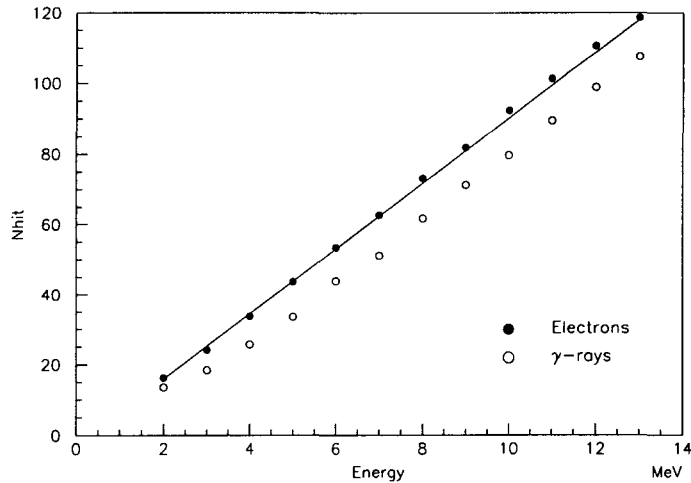


Figure 3.12: Simulated SNO response to electrons and γ -rays in the energy range 2-14 MeV.

3.6.1 Energy Calibration Sources

The energy calibration sources provide γ -rays with energies in the range from 1.4 to 19.9 MeV, and provide calibration at points throughout and beyond the solar neutrino energy region, as shown in Table 3.5. The common feature amongst these sources, with the exception of the p-t source, is that the γ -ray is produced in coincidence with one or more charged particles. A signal generated by the charged particle(s) will be used to produce an external trigger to record the SNO response to the γ -ray. Both the ^{16}N source, which provides the primary energy calibration with 6.1-MeV γ -rays, and the ^{24}Na source, which allows calibration below the expected low-energy threshold, feature β -decay. The ^{16}N and ^{24}Na sources will be described in detail in later chapters.

Low-energy calibration will be performed using 2.6-MeV γ -rays from the ^{208}Tl β -decay. The source is a proportional counter with a ^{228}Th plated central wire. The 2.6-MeV γ -ray is useful in the study of neutron backgrounds associated with deuterium photodissociation.

Source	E_γ (MeV)	E_β (MeV)
^{228}Th	2.614	1.8
^{24}Na	2.754	1.4
	1.368	
^{16}N	6.129	4.3
^8Li	n.a.	16.0
pt	19.82	n.a.

Table 3.5: Calibration sources and energies. The end point energy is provided as E_β . The signal from the ^8Li source is due to the β^- , and the trigger results from two α particles which result from ^8Be decay.

High-energy calibration will make use of 19.82-MeV γ -rays from the reaction $^3\text{H}(p, \gamma)^4\text{He}$ [101]. A small proton accelerator has been constructed and enclosed in a stainless steel housing. Protons are accelerated to 30 keV and impinge on a tritium target (scandium tritide evaporated onto a molybdenum substrate). The γ -ray production rate has been determined to be approximately 1 s^{-1} .

There is one energy calibration source which does not rely on a $\beta - \gamma$ coincidence. The beta-decay $^8\text{Li}(e^- \nu_e)^8\text{Be}$ ($Q_\beta^- = 16.0 \text{ MeV}$, $t_{1/2} = 0.838 \text{ s}$) is the isospin mirror process to ^8B decay, therefore the nuclear matrix elements that describes the two β -decay are nearly identical. The resulting electron energy spectra will be very similar, allowing a direct measurement of the SNO response to a beta spectrum covering the ^8B energy range. The reaction $^{11}\text{B}(n, \alpha)^8\text{Li}$ is used for production and an aerosol-laden gas is used to carry ^8Li to the source chamber in SNO. The source will provide an external trigger to SNO from scintillation light produced by the two alpha particles resulting from ^8Be decay. The source chamber will be a thin-walled acrylic sphere, coated on the inside to restrict scintillation light from emerging into the D_2O . The e^- will produce Čerenkov light in the acrylic and the D_2O that will provide the calibration signal. This source remains under development.

3.6.2 Triggering and Signal Development

The overview of the signal processing electronics provided here is intended to facilitate the understanding of tagged calibration source operations in SNO. An assessment of electronics performance is provided in [86].

The signal from the PMT is split and passed through two devices: a four-channel dual-range amplifier-shaper-integrator for the energy, and a four-channel discriminator for timing. If the signal exceeds the discriminator threshold, a timer begins counting. The energy signals and PMT event time are stored in analog memory on a CMOS chip. The timing signals are propagated from the daughter board to the mother board where a 32:1 sum is performed. The timing signal is again summed on the Crate Trigger Card (16:1) for the 512 channels associated with each crate. A 19:1 sum is performed on the Master Trigger Card/Analog. If the MTC/A discriminator threshold is exceeded, then a digital signal is output to the Master Trigger Card/Digital. The MTC/D issues a global trigger (incrementing a counter at each channel) and distributes information specific to the trigger (global trigger number and GPS time stamp) back to those channels having active timers. The registers may then be readout via DAQ control. Analog memory contents are reset if the timer for the channel times out prior to receiving a global trigger.

Timing and accumulated electric charge information are obtained from the readout of an individual PMT. The charge is proportional to the amount of light incident on the PMT. In most SNO events, this is a single ultraviolet photon. The PMT threshold is therefore very low: the expected mean noise rate for an individual PMT is ~ 1 kHz at 10C. The establishment of an Nhit or charge trigger threshold equal to approximately twenty Nhit, however, almost completely reduces PMT noise coincidence events in the 400 ns time window to zero.

Recording the time at which a PMT fires relative to other PMTs in an event is essential for data analysis more complex than simply counting Nhit. The position and

direction of the particle emitting Čerenkov light may be found through algorithms relying on the timing information to sort noise from data, and then to analyze the space-time distribution of N_{hit} to match the Čerenkov production geometry. Three measurements of integrated charge are made in each channel to provide additional data to separate a valid PMT hit from noise. The integrators are as follows:

- High gain, Long integration time (pmtihl): used to collect complete charge.
- High gain, Short integration time (pmtihs): to compare with long time, high gain. This allows a comparison of the early charge to the total charge.
- Low gain, Long or short integration time (pmtilx): A low gain measure in the event of excess charge in the high gain channel.

The use of three charge measurements also allows for internal consistency checks for each PMT.

The triggering method described above, in which the sum of all PMT signals exceed a threshold, may be applied to either N_{hit} or to the integrated charge from all PMTs (ESUM) with active timers. These two conditions describe broad trigger classes, and SNO may operate with various active N_{hit} and ESUM triggers. The sums may be performed over 20 or 100 nanosecond periods, and multiple thresholds may be tested simultaneously.

Calibration devices may be used to trigger SNO independent of the N_{hit} and ESUM triggers. These external triggers (EXT) allow calibration with sources which otherwise would not produce uniquely identifiable signals. For instance, calibrating below the low-energy threshold using γ -rays is possible if SNO can be triggered in time with the γ -ray production. Such signals would be undetectable due to the high background event rates if their observation relied on N_{hit} or ESUM triggers.

3.7 Summary

The Sudbury Neutrino Observatory will measure the ^8B solar neutrino spectrum with high precision. The charged-current signal will provide an energy spectrum for the ν_e flux, while the neutral-current measurement provides the first solar neutrino flux measurement unbiased by neutrino flavor. Backgrounds are a major concern, and will be carefully assessed throughout the life of the experiment. The charged-current spectral shape analysis will seek to determine neutrino oscillation parameters. This analysis requires a very accurate energy calibration. We now turn to an examination of the energy calibration source based on ^{16}N β -decay.

4. ^{16}N Energy Calibration Source

The β decay of the radioactive isotope ^{16}N provides the basis for the primary SNO energy calibration source [102], [103]. The β decay will occur within a source chamber which will produce a signal used to trigger SNO. Gamma rays emitted from excited states of the daughter nucleus (^{16}O) will be coincident with the β particle. Those γ -rays which escape the source chamber will interact in the D_2O to produce Čerenkov light. Detection of the Čerenkov light by the SNO photomultipliers (PMTs) in time with the source chamber trigger constitutes the calibration event.

The spectrum of PMT hits (Nhits) which results from the ^{16}N calibration events will be used to verify the accuracy of the SNO Monte Carlo simulation code (SNO-MAN). This type of calibration provides a check on the overall performance of the detector systems. It will follow calibration and assessment of the individual system components, such as the light attenuation by H_2O , D_2O and the acrylic vessel, the optical sensitivity of SNO PMTs and the performance and stability of the SNO electronics and data acquisition. The ^{16}N calibration source will be used repeatedly to monitor the stability of SNO.

4.1 ^{16}N Production

The physical characteristics of ^{16}N β -decay impose constraints on the means to produce and use it as a calibration source. The half-life is 7.13 seconds, requiring that it be produced as it is used. It is produced by the reaction $^{16}\text{O}(n,p)^{16}\text{N}$, which requires 14-MeV neutrons. The cross-section is 42 mb, therefore many neutrons are introduced into the environment. It is not useful to introduce neutrons into the D_2O during energy calibration, therefore ^{16}N is produced far from the D_2O .

A gas transport system [104] was developed to quickly move the ^{16}N into a chamber located in the D_2O . A neutron generator is used to produce the 14-MeV neutrons from the reaction $^3\text{H}(d,n)^4\text{He}$. The generator accelerates deuterium to 100 keV and

provides a maximum 100 mA current that results in up to 10^8 neutrons s^{-1} . The deuteron energy is below the Coulomb barrier (0.446 MeV) but high enough for the barrier penetration probability to allow the observed flux with the maximum current. The neutrons are produced in a beam that is directed through a target chamber. The target is CO_2 gas, which maximizes the number of target nuclei and minimizes the hazard of using pure oxygen in an underground facility. The ^{16}N nuclei will be subject to collisions with the CO_2 molecules that sweep through the target chamber and flow via a thin capillary to the source chamber located more than 30 m away. The source chamber will be attached to a motor-driven carriage and inserted into the D_2O region during calibration activities. The system will produce more than 300 ^{16}N decays per second in the source chamber.

4.2 ^{16}N Source Chamber Design

The ^{16}N source chamber design results from a compromise between two goals:

1. The β particles from ^{16}N decay must be confined within the chamber; and,
2. A high fraction of the γ -rays are to emerge unattenuated into the D_2O .

The main casing (CAN, as denoted in Fig. 4.1) is a tube of stainless steel which is $16\frac{1}{2}$ " long and has a wall thickness of $\frac{3}{16}$ ". Stainless steel top and bottom plates have grooves along the circumference to hold o-rings which seat on the inner surface of the tube. An annular plate with o-ring (RING) separates the chamber interior into upper and lower volumes. A thin sleeve ($\frac{1}{16}$ ") of stainless steel (aluminum) maintains a constant distance between the interior annular plate and the bottom (top) plate. The interior surfaces of the tube distal to the o-ring seals are threaded for a length of 1 cm. Threaded annular rings back up the top and bottom plates, so that the o-rings cannot move during source chamber operation at pressure near 60 psi.

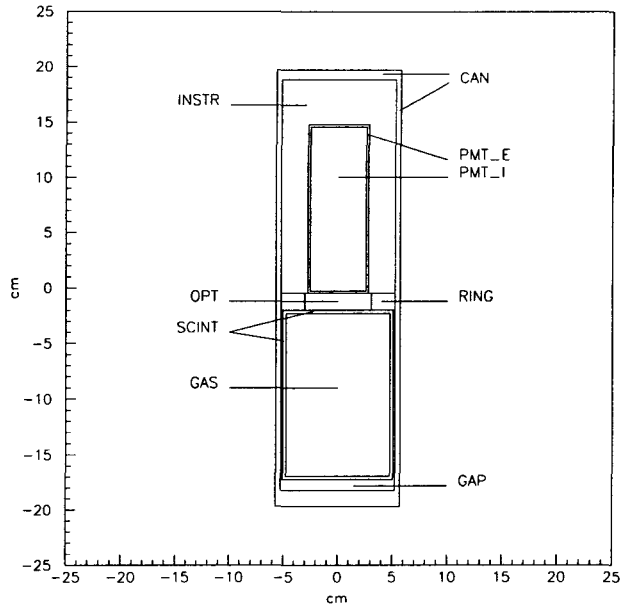


Figure 4.1: A schematic representation of the source chamber.

The ^{16}N decays occur within a cylindrical shell of plastic scintillator¹ (SCINT) located in the lower volume. Gas is introduced via a coaxial Teflon capillary (o.d. $\frac{1}{4}$ "). The capillary is secured to a fitting atop the inner annulus. The inner capillary (o.d. $\frac{1}{8}$ ") extends through the interior of the scintillator, causing ^{16}N gas to be introduced at the bottom of the gas volume (GAS). The outlet for the gas is the outer coaxial capillary. The uniform distribution of gas and a long dwell time in the scintillator are achieved by introducing gas to the bottom and removing it from the top of the scintillator.

A 2" photomultiplier tube (PMT), located in the upper volume (INSTR), monitors the scintillator for light (PMT_I and PMT_E). A high voltage converter with 12 V input produces a maximum output of 2,000 V and is also in the upper volume. The top plate has an aperture in the center to allow coupling to an umbilical cord. The umbilical-to-top plate connection is sealed with a sequence of three o-rings and

¹A material which emits light in the optical or ultraviolet range in response to ionizing radiation

pressure plates. The umbilical contains conducting wires, a signal cable and the coaxial gas capillary. Space is provided above the PMT in the upper volume for coupling of these items to their counterparts.

A rigid acrylic window (OPT) occupies the central portion of the stainless steel annulus which separates the upper and lower volumes. An aluminum plate which makes an o-ring seal with the annular plate is used to mount the acrylic window. Coupling of the window to the scintillator is via a $\frac{1}{8}$ " thick optical pad. The window is coupled to the PMT by another optical pad. This arrangement allows for the PMT or scintillator to be independently separated from the optical coupling window. It also maintains a consistent alignment of the relative positions of the PMT and scintillator.

4.3 ^{16}N Source Chamber Operation

A simplified ^{16}N decay scheme is presented in Figure 4.2. The branch of primary interest for calibration produces a β particle with end point energy 4.3 MeV and a 6.1-MeV γ -ray (66.2%). There are other branches which produce γ -rays in coincidence with β particles (6%). There is also a direct branch to the ground state, resulting in a 10.4-MeV endpoint β particle without an associated γ -ray (28%). Thus, each β particle will produce a trigger for SNO, but not all triggered events constitute a valid calibration event.

The scintillator inside the source chamber does not significantly affect the γ -ray energy spectrum. It has a wall thickness of 3 mm, therefore, fewer than 3% of ^{16}N 6.1- and 7.1-MeV γ -rays will deposit energy in the scintillator [106]. Energy deposition in the scintillator is predominantly due to ^{16}N β particles. The scintillator has a poor efficiency for stopping β particles with energy greater than 1 MeV [105]. The scintillator will not measure the energy spectrum of the ^{16}N β particles.

The ^{16}N γ -rays will predominantly interact in the stainless steel. This is due to the limited scintillator wall thickness and the greater Z of the steel. While the steel

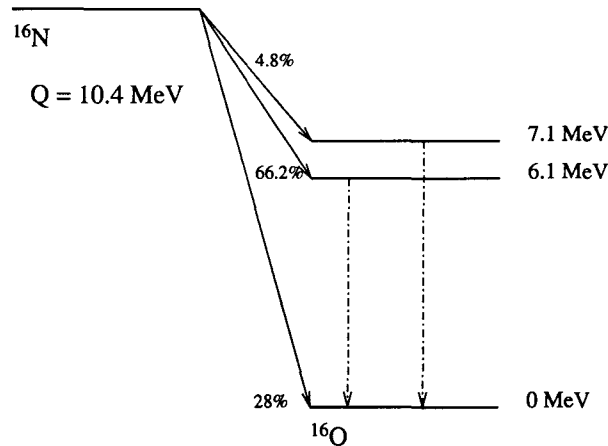


Figure 4.2: Major ^{16}N β decay branches. The γ -ray energies appear to the right of the energy levels. The β decay branch strengths are shown as percentages near the arrow depicting the transition.

allows many of the γ -rays to pass at full energy, there is significant attenuation, which has been estimated by experiment and simulation. These results are presented below in Sections 4.4 and 4.5, respectively.

The stainless steel wall of the ^{16}N chamber and insert sleeve provide $1/4''$ total thickness. This figure is selected to attenuate nearly all of the β particles from the 10.4-MeV branch [107] while minimizing the attenuation of ^{16}N γ -rays. This also leads to the generation of γ -rays via bremsstrahlung as the β particles interact with the scintillator and steel. The contribution to energy deposition in the D_2O from bremsstrahlung is small and is discussed in detail in Section 4.6.

It was noted in Section 3.6 that the γ -ray N_{hit} response is nonlinear. The γ -ray N_{hit} spectrum is subject to the following influences:

- Čerenkov radiation is produced by energetic e^- , therefore, the SNO response to γ -rays will be proportional to, but not equal to, the full γ -ray energy. The processes for the γ -ray to transfer energy to e^- in the D_2O are e^+e^- production and Compton scattering. The full γ -ray energy will not manifest as e^- kinetic energy due to the following causes:

1. The creation of mass in e^+e^- production.
 2. The energy carried by the Compton scattered final state γ -ray.
- Compton scattering or e^+e^- production from γ -ray interactions within the ^{16}N chamber represents energy lost to the calibration event. The energetic charged particles resulting from these interactions will lose energy within the chamber and will likely not emerge into the D_2O . The N_{hit} spectrum will thus be broadened toward low energy by γ interactions (attenuation) in the steel of the source chamber.
 - The N_{hit} spectrum may be broadened due to interactions between high-energy β particles and the ^{16}N chamber. The interaction of β particles in the chamber will lead to bremsstrahlung, some of which will escape into the D_2O . These photons will produce Čerenkov light. It is also possible for a 10.4-MeV β particle to penetrate the wall of the source chamber and directly produce Čerenkov photons in the D_2O . The source chamber has been designed to minimize such contributions to light within SNO. This issue has been examined through SNOMAN simulation and is reported below in Section 4.6.
 - The N_{hit} spectrum may be expected to vary with position throughout the D_2O volume. The acrylic vessel is not perfectly spherically symmetric due to the placement of belly plates for the support ropes, the aperture of the chimney, as well as numerous small internal features (NCD anchor blocks and water pipes). There are also irregularities in the arrangement of the photomultiplier tubes, to allow for the passage of piping for the H_2O supply and for the ropes which support the acrylic vessel. An investigation has been performed with the ^{16}N chamber position varied in one meter increments along the major axes of the detector. These results are reported in Sections 4.7.1 and 4.7.2.

4.4 Experimental Results for γ -ray Attenuation

Gamma ray attenuation was studied by direct measurement, comparison with calculations and by Monte Carlo simulation. The measurements were performed with ^{54}Mn and ^{241}Am - ^9Be sources. The ^{54}Mn source provides a single γ -ray at 835 keV. The ^{241}Am - ^9Be source produces a 4.44-MeV γ -ray from the reaction $^9\text{Be}(\alpha, n)^{12}\text{C}$ through the deexcitation of the corresponding excited state in ^{12}C . Attenuation was determined by the following measurements made with a 3" \times 3" NaI detector (item 2 was obtained only in the ^{54}Mn study):

1. Measurement of the bare source spectrum.
2. Attenuation of the spectrum using a stainless steel tube $\frac{1}{16}$ " in thickness.
3. Attenuation of the spectrum using a stainless steel tube $\frac{3}{16}$ " in thickness.
4. Background spectra for each of the above geometries.

The sources were placed radially in the center of each tube and positioned away from the tube ends. Lead bricks were used to shield the NaI detector from room background.

The attenuation of γ -rays by materials is well described by the cross sections (σ) for photoelectric absorption, Compton scattering and e^+e^- production. These σ have been measured by Storm and Israel [110]. The measurements are made using collimated beams of γ -rays incident on flat plates of material. Attenuation is defined in this work as a removal of flux from the incident beam. The following formulas are used to determine the expected attenuation, A , from these measured cross section values:

$$A = 1 - \frac{I}{I_0} = 1 - \exp(-\mu x) \quad (4.1)$$

$$\mu = N(\sigma_{pe} + \sigma_{cs} + \sigma_{pp}) \quad (4.2)$$

The beam intensity at depth x is $I(x)$, the initial intensity is I_0 and the density of target nuclei in the plane normal to the beam is N . The comparison of the expected and observed attenuation is complicated by differences in experimental geometries. Our source emitted γ -rays isotropically and the attenuation material is a cylindrical tube. The longitudinal axis of the NaI detector was aligned to the source, and positioned in the plane normal to the vertical attenuation tubes. This arrangement minimized the geometrical differences with the assumption of a γ -ray beam incident on a flat plate. Applying the flat plate formula to ^{16}N decays in the source chamber is further complicated by the geometry of source and absorber. The ^{16}N decays may occur anywhere within the volume enclosed by the scintillator. Additionally, the γ -rays will be emitted isotropically. Then most γ -rays will see a path length through stainless steel greater than the wall thickness. Therefore, these calculations represent a minimum value for the attenuation.

4.4.1 ^{54}Mn Results

The attenuation of an 835 keV γ -ray calculated by means of Eq. 4.1 was found to be 7.3% and 27.4% for the thin and thick steel attenuator tubes, respectively. These values were determined by subtracting the number of counts in the background-corrected full-energy peak of the attenuated spectrum from those in the unattenuated spectrum. The predictions for attenuation by a flat plate on a γ -ray beam are 7.96% and 22.0%, respectively.

4.4.2 $^9\text{Be}(\alpha,n)^{12}\text{C}$ Results

Two spectra (one with and one without attenuation by the steel tubes) were obtained with the source in place over a 6-day period. Background spectra with and without attenuation were also obtained over six days and background subtraction was performed. The full energy peaks were subtracted to find 13.5% attenuation.

Additionally, the region from above the full energy peak to below the double escape peak was similarly subtracted to find 12.4% attenuation. The calculation for a 4.4-MeV γ -ray is 11.3% attenuation.

Figure 4.3 shows the data and background spectra without attenuation in the region of 2.5 to 5 MeV. The top panel shows the data and background spectra. The lower panels show the background subtracted spectra in the region of the full energy peak through the double escape peak for the unattenuated (left) and attenuated (right) runs. The peak at 3.25 MeV in the background spectrum is due to ^{56}Co and was part of our room background.

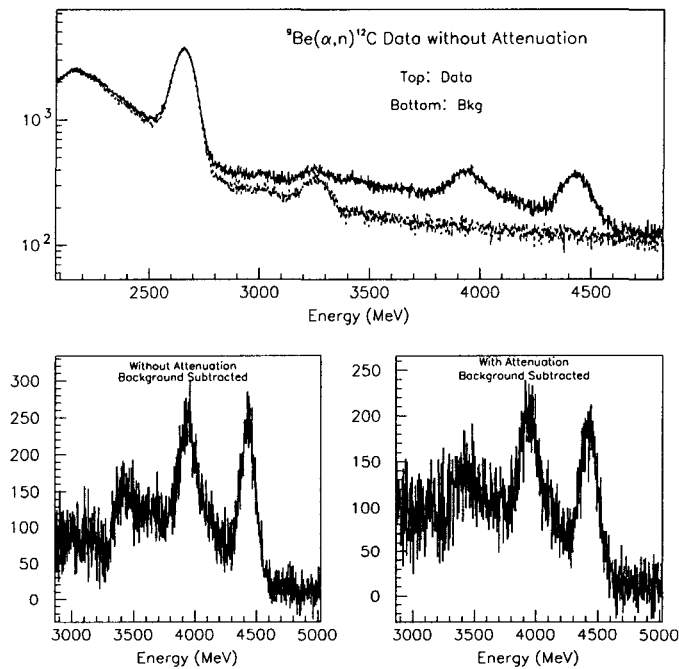


Figure 4.3: Data for the attenuation of 4.4-MeV γ -rays from $^9\text{Be}(\alpha,n)^{12}\text{C}$ by the steel used for the outer container of the ^{16}N chamber. Top panel: Data and Background spectra without attenuation. Lower panels: Background subtracted spectra showing data without attenuation (left) and with attenuation (right).

4.5 Simulation Results for γ -ray Attenuation

Monte Carlo simulation provides nearly unlimited flexibility to investigate particle interactions. Substitution of D₂O for stainless steel, for instance, is not yet a technique available in the laboratory, but is achieved within the Monte Carlo studies reported here.

SNOMAN has been used to simulate the detector response to the ¹⁶N source. Code describing the source geometry was written and incorporated into SNOMAN. Details concerning this code are included in Appendix A.

SNOMAN is intended to simulate the detector response to light. Events featuring particle interactions which do not produce sufficient light to exceed the simulation threshold will not appear in the simulated data. As a result, SNOMAN has limitations for testing the effects of the source chamber on the emerging spectra of β particles and γ -rays. The focus of γ -ray attenuation simulations therefore concerns comparing the results for simulations with and without the source chamber.

4.5.1 Stainless Steel Effect on γ -rays

The design of the ¹⁶N chamber was dictated by the conflicting criteria that complete attenuation of the ¹⁶N β particles is desired, while also achieving minimal attenuation of the ¹⁶N γ -rays. The stainless steel outer container is intended to attenuate the β particles. Isolating the effect of the steel on the γ -rays is investigated by eliminating β particles from the ¹⁶N simulation decay scheme. An estimation of γ attenuation is then obtained from comparing simulations with and without the presence of stainless steel. In the first case, the simulation is with the complete source chamber geometry. In the second, the D₂O media is substituted for those detector elements which consist of stainless steel.

The number of events and the position of the centroid and width of the main Nhit peak are presented in Table 4.1. The number of events exceeding the hardware

threshold of 10 Nhit is reduced by 14.6%. This agrees with the expected 11% attenuation of a 6-MeV γ -ray beam incident normal to a $\frac{1}{4}$ " layer of steel [109]. Most of the γ -rays will not be normally incident on the ^{16}N chamber walls, due to the uniform distribution of ^{16}N atoms within the scintillator together with the isotropic direction distribution of the emitted γ -rays so the mean path length will be greater than $\frac{1}{4}$ ". Additionally, many γ -rays will traverse paths greater than $\frac{1}{4}$ " by moving through the instrumentation volume or through the end caps of the source chamber. The peak centroid is decreased 2.3%, while the width is increased 5.5% by the presence of steel. The uncertainty in the position of the centroids is approximately 0.24%, so this shift is significant and should be considered in the actual calibration analysis. This spectrum is compared to that of the full decay scheme in Fig. 4.4.

	No β or steel	No β	% change
Events	7409	6310	-14.6%
Nhit	47.43	46.33	-2.3%
σ	9.86	10.40	+5.5%

Table 4.1: γ attenuation due to stainless steel for 10000 ^{16}N decays.

The effect of the attenuation is two-fold. The shift of the Nhit centroid to lower values introduces a systematic uncertainty into the measurement of Nhit response to γ -ray energy. The magnitude of the shift is significant compared to the statistical uncertainty ($< 1\%$) that will be achieved with ^{16}N calibration. Monte Carlo simulation of this effect provides for a correction to the centroid, but the Monte Carlo uncertainties will need to be evaluated independently. Additionally, the broadening of the distribution is asymmetric, making the approximation to a Gaussian distribution poorer, and decreasing our statistical uncertainty for a fixed number of calibration events.

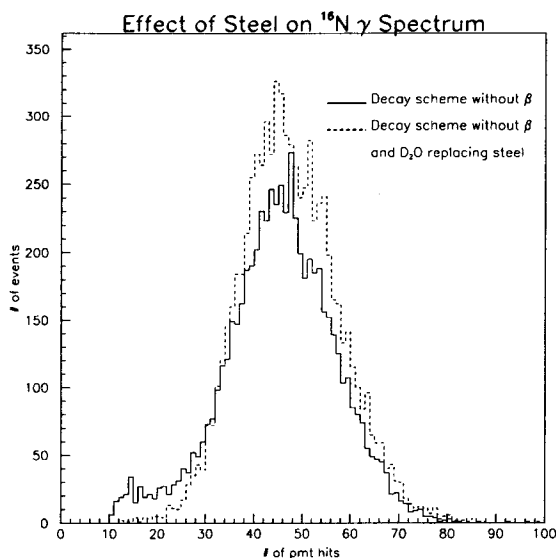


Figure 4.4: The Nhit spectra due to the γ -rays of ^{16}N are shown in two cases. The solid line is with the full source chamber geometry. The dashed line spectra is the result of replacing the steel of the source chamber by D_2O .

4.5.2 Energy Deposition in D_2O

The attenuation of γ -rays may also be studied through the energy deposition in the D_2O . Two simulations were performed featuring the release of 10^5 monoenergetic γ -rays (6.13 MeV) from the gas volume enclosed by the scintillator. In one case the full geometry of the source chamber was included, while in the other all of the source chamber media, including that of the gas volume, was replaced by D_2O . The resulting spectra were analyzed to find the number of events depositing full or partial energy in the D_2O and the total number of events exceeding a threshold of 10 Nhit. The results appear in Table 4.2.

In the case without the source chamber present, 488 γ -rays (0.488%) did not generate more than 10 Nhit. These events are mainly due to photodisintegration of deuterium. Of those events which do exceed the Nhit threshold, 0.15% are partially attenuated from the full energy. When the source chamber is present 12.5% of γ -rays fail to generate enough light to exceed the 10 Nhit threshold. There are an additional

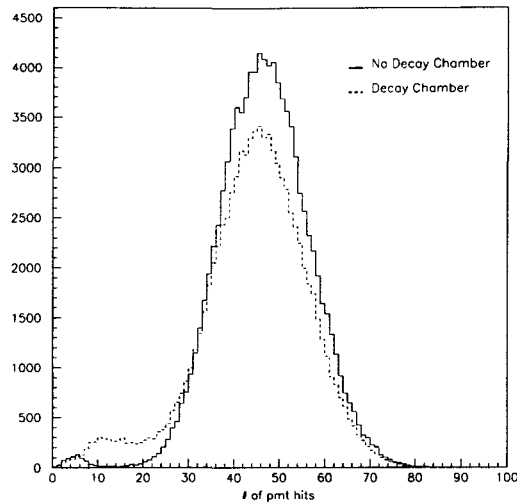


Figure 4.5: The N_{hit} spectra due to 6.13-MeV monoenergetic γ -rays are shown in two cases. The solid line depicts the spectrum seen after replacing the media of the full source chamber geometry with D_2O . The dashed line spectra depicts the standard media of the source chamber geometry.

11.2% of events which are attenuated from full energy. This is consistent with results in Section 4.5.1 and quantifies the change in the shape of the N_{hit} spectrum seen in Figure 4.4.

The effect of γ -ray attenuation on the N_{hit} spectrum is considered. The simulation with the ^{16}N chamber shows that 24% of 6.13-MeV γ -rays will be attenuated from their full energy. Approximately half of the attenuated γ -rays do not contribute to the N_{hit} spectrum. The mean value of a Gaussian fit to the plot of N_{hit} for each case is included in Table 4.2. The effect of the source chamber is to decrease the mean value and broaden the distribution toward low numbers of N_{hit} . A plot comparing the N_{hit} spectra with and without the source chamber is shown in Figure 4.5.

The yield of 6.13-MeV γ -rays from a run of ^{16}N may be inferred from the simulation results. The strength of the 4.3-MeV β decay branch strength is 66.2%. The simulation of the monoenergetic 6.13-MeV γ -rays reveals 24% attenuation from full

	Events	Full Energy Events	Nhit	σ
No source chamber	99512	99366	46.84	9.50
source chamber	87074	75761	45.71	10.07

Table 4.2: Attenuation with full ^{16}N chamber geometry for 10^5 6.13-MeV monoenergetic γ -rays.

energy. Taken together, this suggests that 50% of ^{16}N decays will lead to the deposition of 6.13 MeV in the SNO D_2O .

4.6 Beta Interactions in the Source Chamber

Electrons lose energy in a medium through collisions with atomic electrons and through the emission of radiation due to accelerations imposed by interactions in the media, or bremsstrahlung [111]. The former energy loss mode is completely benign for SNO provided the electron is contained within the medium. The later mode is capable of transferring energy into the D_2O independent of containment medium thickness. Both modes are investigated for their influence on the Nhit spectrum. Two distinct event classes are considered: those resulting only from β particle interactions, and those for which a β particle and a γ -ray both create light seen by SNO.

Bremsstrahlung interaction in the ^{16}N source chamber was studied using SNO-MAN simulation. The EGS4 package was set to perform bremsstrahlung calculations using a detailed description of angular variation provided by the Shiff equation, which is discussed in reference [85].

4.6.1 Direct Čerenkov Light Production

A simulation of ^{16}N was performed without γ -rays to assess the Nhit spectrum arising solely from β particle interactions. Either β particles escaping the source chamber or those emitting bremsstrahlung photons contribute to this Nhit spectrum. A low energy feature is observed and compared with the Nhit spectrum resulting from

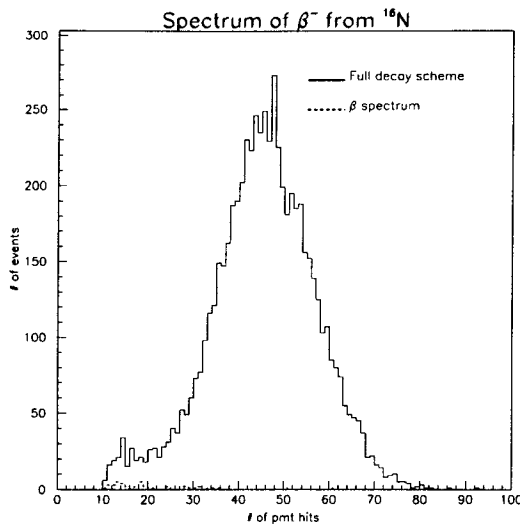


Figure 4.6: Comparison of ^{16}N simulation featuring the full decay scheme and a simulation featuring only the β particles of the ^{16}N decay scheme.

the full decay scheme (Fig. 4.6), demonstrating that β particles will make a direct contribution to the SNO response above a threshold of 10 Nhit in fewer than 1% of ^{16}N decays.

4.6.2 The 10.4-MeV β decay branch

Further assessment of the influence of the 10.4-MeV β decay branch on the Nhit spectrum was carried out through additional SNOMAN simulations. A beta energy spectrum was defined with an endpoint of 10.4 MeV and 10000 β particles were generated with an isotropic direction distribution. The SNOMAN hardware threshold was set to 2 Nhit and noise was suppressed.

The Nhit spectrum appears in Figure 4.7 and the analysis is summarized in Table 4.3. Approximately 4% of decays lead to Nhit of 2 or greater. The influence on the ^{16}N Nhit spectrum is obtained from applying the strength of the 10.4-MeV β decay branch to this percentage. The branch strength is 28%, so that one expects 1% of the Nhit spectrum from ^{16}N decays will be due to this branch. The contribution clearly drops with Nhit, and is reduced to 0.1% when considering Nhit of 20 or greater.

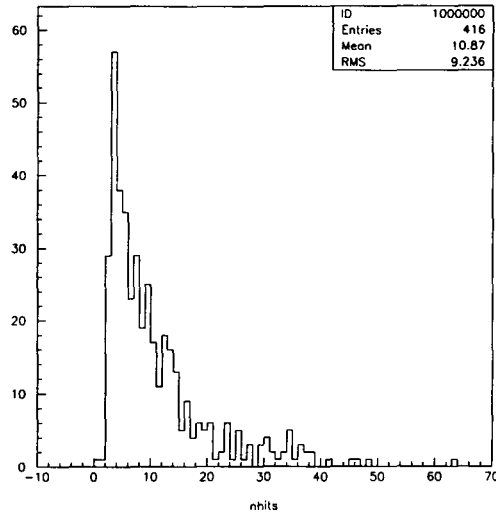


Figure 4.7: The Nhit spectrum due to only the 10.4-MeV β decay branch of ^{16}N .

Systematic uncertainties in the simulation related to 10.4-MeV β particle bremsstrahlung were studied by varying the thickness of the ^{16}N chamber exterior steel wall. The thickness was varied in $\frac{1}{16}$ " steps, from the standard $\frac{1}{4}$ " to $\frac{7}{16}$ ". Each simulation featured 100,000 events. Nhit thresholds of 10 and 20 were considered. The results are summarized in Table 4.4.

The number of β particles which emerge from the chamber is very small. The influence of the 10.4-MeV branch on the Nhit spectrum is almost entirely due to bremsstrahlung. Considering the standard wall thickness of $\frac{1}{4}$ ", 0.665% of β particles led to Nhit greater than 20. Apply the branching ratio (28%) and this contribution

Threshold	Events	Attenuation	^{16}N Flux
2	416	95.8%	1.05 %
10	159	98.4%	0.4 %
20	55	99.4%	0.1 %

Table 4.3: The 10.4-MeV β spectrum of ^{16}N was simulated with 10000 β particles in the ^{16}N chamber geometry. Attenuation is reported as number of events which exceed the Nhit threshold and as a percentage. The percent contribution to the ^{16}N Nhit spectrum is reported in the column entitled " ^{16}N Flux".

Thickness	Nhit Events	Brems. γ -rays	Escape β s	Attenuation
1/4"	1650 (665)	2004	22	98.35% (99.35%)
5/16"	1505 (607)	1800	18	98.49% (99.39%)
3/8"	1454 (555)	1738	19	98.55% (99.45%)
7/16"	1390 (539)	1668	12	98.61% (99.46%)

Table 4.4: The 10.4-MeV β spectrum of ^{16}N was simulated with 100000 β particles in the ^{16}N chamber geometry. Four different wall thicknesses are investigated. Data is displayed as follows: The number of events exceeding the threshold, number of γ -rays emitted into the D_2O , number of β particles emitted into the D_2O and attenuation as a percentage of simulated events are shown for the 10 (20) Nhit threshold.

is reduced to 0.18%. Increasing the wall thickness to $\frac{7}{16}$ " reduces the contribution to 0.15%, while it would greatly increase the attenuation of 6.1-MeV γ -rays. Therefore, the present source chamber wall thickness represents a good compromise between the design goals. The Monte Carlo results provide the means to estimate the pull exerted on the Nhit centroid by events resulting from the 10.4-MeV β -branch. An independent assessment of the number of bremsstrahlung photons and e^- emerging from the ^{16}N source chamber is needed to assess the uncertainties of the SNOMAN simulations.

4.6.3 Bremsstrahlung from the 4.3-MeV β Decay Branch

A second consideration is the indirect influence of bremsstrahlung on the shape of the Nhit spectrum. It is possible for a 4.3-MeV β particle to create a trigger in the source chamber, and also interact in the scintillator or steel to produce bremsstrahlung γ -rays which then enter the D_2O . In this case, the bremsstrahlung photon will be in time with the 6.1-MeV calibration γ , potentially increasing the Čerenkov light associated with the calibration event.

The top two panels of Figure 4.8 compare two simulated Nhit spectra. On the left, the Nhit spectrum is due to 6.1-MeV γ -rays generated within the ^{16}N chamber. On the right, a 4.3-MeV β -spectrum is generated in coincidence with 6.1-MeV γ -rays, again within the ^{16}N chamber. The number of events in the two spectra is the same within 0.03%. The means of the spectra are identical within 0.1%. The centroid of the main peak in each spectrum was determined through a Gaussian fit. The centroid values agree within 0.04%. Comparison of the widths of the central peaks shows no significant change, as the width of the central peak for the $\beta + \gamma$ simulation is actually narrower by 1%.

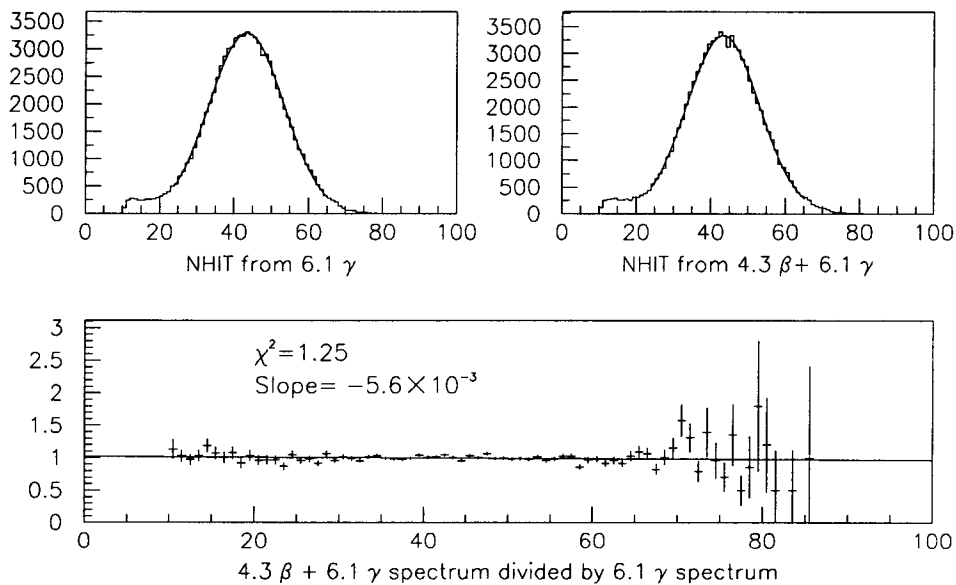


Figure 4.8: The top two panels feature a comparison of simulated Nhit spectra when (left) only 6.1-MeV γ -rays and (right) a 4.3-MeV β -spectrum in coincidence with 6.1-MeV γ -rays are generated within the ^{16}N chamber. The lower panel shows the result of dividing the $\beta + \gamma$ spectrum by the γ only spectrum.

Another comparison of these spectra involves dividing the β - γ coincidence spectrum by the γ -only spectrum. This is shown in the lower panel of Figure 4.8. In the absence of Nhit contributions from bremsstrahlung interactions, the divided data

should fit to a straight line. The results of such a fit show a slope of -5.6×10^{-4} and an intercept of 1.02 ± 0.02 with a reduced- $\chi^2 = 1.24$. The fit is therefore satisfactory to a straight line with nearly zero slope, indicating that the Nhit spectrum of the 6.1-MeV γ is not significantly affected by contribution from bremsstrahlung caused by the 4.3-MeV β decay branch of ^{16}N . The data above 70 Nhit tend toward values showing contribution from the β particle, but referring to the top panel of Figure 4.8 emphasizes the small contribution to the Nhit spectrum in this region.

4.7 Spectrum of Phototube Hits

4.7.1 Nhit Spectrum Variation by Source Location

With the understanding of the ^{16}N Nhit spectrum acquired in the previous section we turn to the study of this spectrum as a function of position within the D_2O volume. The privileged position at the detector's center is taken as the reference.

The ^{16}N chamber location was varied on a 1 meter grid in the x - z plane in the D_2O volume. The geometry of the AV was simplified to exclude belly plates. Simulations featured 10,000 decays at each location. Each simulation used the same initial random number seeds. The resulting Nhit spectra have two significant features. The main feature is a peak with centroid of approximately 46 and width 10.5 Nhit (a sample spectra appears in Fig. 4.9). A secondary feature caused by the interactions of γ -rays and β particles with the steel of the source chamber appears at low energy. This is discussed below. The main feature of the spectrum is of interest for SNO ^{16}N calibration.

The analysis to determine the centroid of the main Gaussian feature was conducted by performing a χ^2 minimization. The Physics Analysis Workstation [108] analysis software package was used to fit the histogram. The range of the histogram fit was adjusted for each spectrum to produce the best fit based on the ratio of χ^2 per degrees of freedom (ndf). The adjustment was made to exclude the low energy feature from

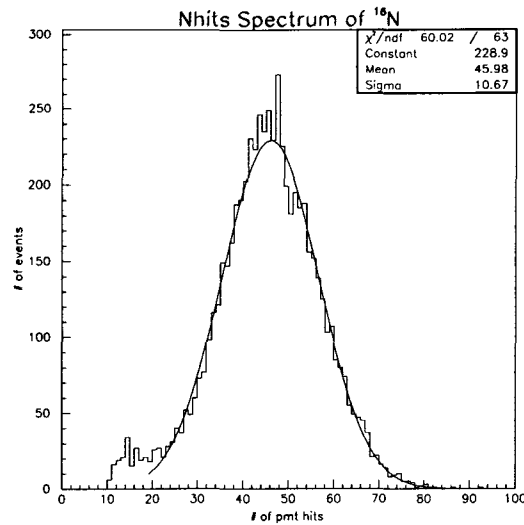


Figure 4.9: Nhit spectrum from 10000 ^{16}N decays. An asymmetric range is used to fit the main feature to a Gaussian distribution, which is represented by the solid line.

the fit (Fig. 4.9). In most cases the result of the fit was a χ^2/ndf within the range 0.95-1.05. The values presented for the width of the peak need to be interpreted with the understanding that the fit limits were adjusted to exclude the low energy feature. This is adequate to allow comparison of spectra fit by the same method, but does not provide an exact determination of the width. The results are presented in Table 4.5.

The left column (Vertical Position) denotes the vertical position of the source chamber with respect to the equator of the acrylic vessel. The digits above the remaining columns (Horizontal Position) denote the horizontal position relative to the SNO vertical axis. The mean value of Nhit is 46.5 ± 1.0 when considering all positions except those very near the neck of the AV chimney. The value of Nhits rises as the source chamber is moved away from the center of SNO to a distance of 3–4 meters, then begins to decrease again at greater displacements. The region in the immediate vicinity of the chimney neck shows a significant reduction in the value of Nhit, 7.8% lower than the value at the center of SNO, and 10.7% lower than the maximum value in the D_2O .

Vertical Position (m)	Horizontal Position (m)											
	0		1		2		3		4		5	
	Nhit	σ	Nhit	σ	Nhit	σ	Nhit	σ	Nhit	σ	Nhit	σ
5	42.4	11.8	43.5	11.0	44.2	10.6						
4	45.5	10.9	46.0	10.9	45.8	10.8	45.8	10.4				
3	46.8	10.4	46.5	10.5	46.8	10.7	46.4	10.5	46.3	10.3		
2	46.9	10.5	47.0	10.5	47.0	10.6	47.3	10.5	46.7	10.5	46.2	10.7
1	46.2	10.3	46.8	10.5	47.2	10.4	47.3	10.4	47.4	10.3	46.5	10.8
0	46.0	10.7	46.4	10.7	46.9	10.5	47.0	10.7	47.4	10.6	46.7	10.5
-1	46.7	10.7	46.7	10.5	46.8	10.5	47.3	10.8	47.3	10.5	46.6	10.5
-2	47.1	10.6	47.0	10.7	47.5	10.8	47.5	10.6	47.1	10.7	45.9	10.6
-3	47.5	10.8	47.4	10.9	47.4	10.7	47.0	10.5	46.6	10.5		
-4	47.1	10.6	47.5	10.4	47.2	10.7	46.6	10.7				
-5	46.6	10.7	46.6	10.6	46.2	10.6						

Table 4.5: Results for ^{16}N simulation points throughout the SNO D_2O volume. The Nhit value appears to the left and the standard deviation σ appears to the right. Each simulation featured approximately 7,000 events. The uncertainty in Nhit is \pm

4.7.2 Geometric Anisotropy

The optical properties of the detector are influenced by the geometric anisotropy resulting from water pipes inside and belly plates outside the acrylic vessel. The water piping has yet to be included in the geometry, but the belly plates are available. A simulation featuring oppositely directed γ -ray beams originating from a position away from the detector center was performed to illustrate the affect of geometric anisotropy. The γ -ray energy was 6.1 MeV. They were generated at $(x,y,z) = (0,300,300)$ cm with directions $\theta = 0.8$ ($0.8 + \pi$) and $\phi = \pi/2$ ($3\pi/2$). These parameters select a short and a long path length to test attenuation. In addition, the short path length directs light away from the belly plates, while the long path length allow light to traverse the acrylic vessel equator. These parameters are depicted in Figure 4.10. This study is meant to be illustrative rather an analytic assessment of the issue.

The effect of the geometric anisotropies on the ^{16}N Nhit response was studied with the inclusion of belly plate geometry. This study illustrates the SNO detector response to the ^{16}N source chamber, and is complementary to the previous study, which considered the anisotropic distribution of γ -rays leaving the source. The cham-

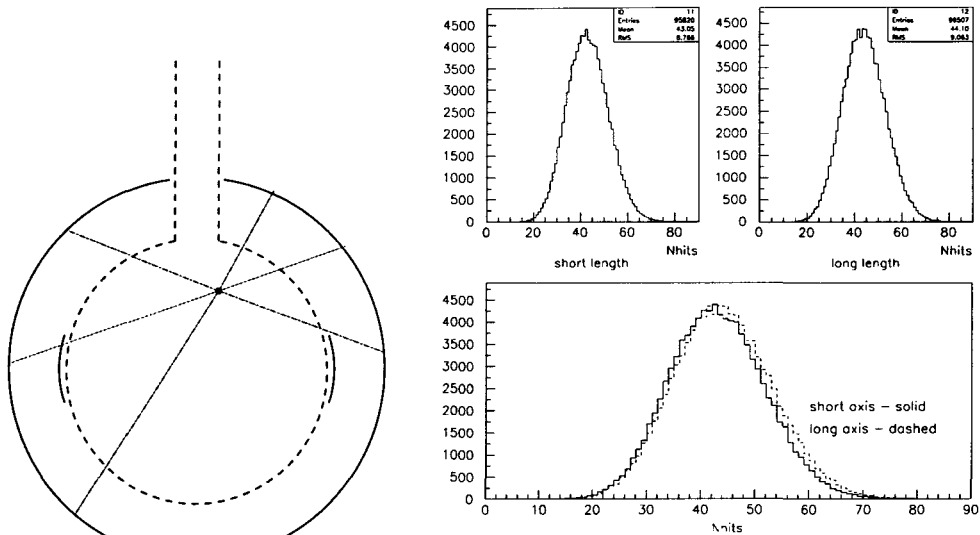


Figure 4.10: Oppositely directed γ -ray beams were simulated to illustrate the effect of geometric anisotropy on Nhit spectra. The simulation parameters appear on the left. The Nhit spectra appear on the right.

ber was located on each major axis of the detector with a 1 meter spacing. The x -axis is oriented to point equidistant between belly plates, while the y -axis points through the center of a belly plate. The locations were varied in the range 0 to +5 meters on the x - and y -axes, and -5 to +5 meters along the z -axis.

These results are depicted in Figure 4.11. The general result from the previous study holds: Nhit as a function of radius increases to a maximum near 3 meters and decreases at 5 meters to nearly the same value as at the origin.

The variation of Nhit with radial displacement can be understood with reference to the thesis work of M. Lay [112]. The performance of the PMT light concentrators shows a dependence on the angle of incident light. A spherical mirror was used to obtain a source of collimated light. A PMT with light concentrator was prepared to allow the angle of incidence to vary. Lay plots the concentration factor versus incident angle, and this value shows a maximum for angles between 20-40 degrees

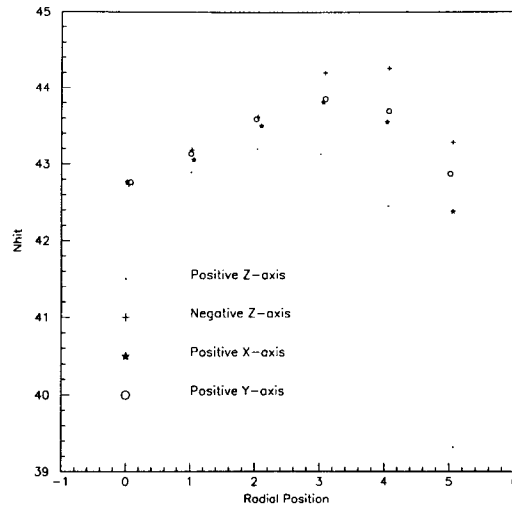


Figure 4.11: The variation of N_{hit} with respect to displacement along the major axes of SNO. The +X axis points between two belly plates, while the +Y axis points directly at a belly plate.

which is approximately 4% greater than the value for normally incident light. The concentration factor decreases sharply for angles greater than 50 degrees, and reaches zero at 57 degrees.

The ^{16}N chamber is a nearly isotropic source of γ -rays. Interactions between high-energy γ -rays and e^- will generally preserve the direction of the γ -rays. One would then expect the distribution of Čerenkov photons resulting from ^{16}N γ -rays to be well approximated by an isotropic distribution.

The variation of incident angle at the face of an arbitrary PMT with ^{16}N chamber position is most simply studied by defining an axis through the ^{16}N chamber position and the center of the PSUP. In this case, the incident angle at the PMT face is simply calculated from a triangle with vertices at the PMT face, the ^{16}N chamber and the center of the PSUP. Results from this calculation are shown in Figure 4.12. The value of N_{hit} should rise as a source is displaced from the origin of the PSUP. In fact, according to the results of the PMT concentrator study, the center of the PSUP

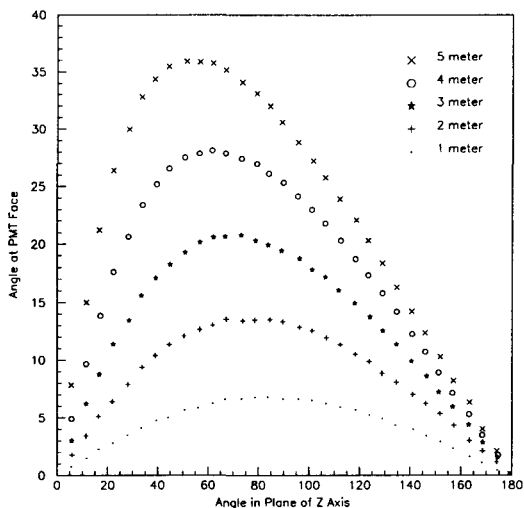


Figure 4.12: The incident angle at the PMT face is plotted for several different displacements of the ^{16}N chamber along the axis defined by ^{16}N chamber position and the center of the PSUP.

is the spot which should generate the least N_{hit} response. Since the incident angle stays well below 50 degrees for displacements of 5 meters, the N_{hit} response should continually increase with increased radial position. However, the simulation shows that N_{hit} values turn down again for large displacements. This is due to increased scattering and attenuation as more Čerenkov photons strike the AV at large angles.

4.7.3 Gamma Ray Emission Isotropy

The γ -ray attenuation will be essentially independent of the azimuthal emission angle due to high symmetry in the source chamber. The γ -ray absorber distribution is strongly asymmetric as a function of polar angle (θ). SNOMAN simulations were conducted to determine how the asymmetric source chamber influenced the isotropy of the γ -ray flux into the D_2O . A quantitative prediction of the flux is important for planning how to use the source. The polar angle of the emitted γ -ray is obtained by SNOMAN simulation. Recall that only events which successfully generate Čerenkov

light are recorded in the SNOMAN simulations. Representing the γ -ray attenuation by polar angle results in a comparison of events into unequal volumes. The available solid angle, $d\omega$, associated with each division of polar angle, θ , was calculated according to $d\omega = \cos \theta_{\text{initial}} - \cos \theta_{\text{final}}$ for comparison against the Monte Carlo data.

A SNOMAN simulation produced 200,000 6.129-MeV γ -rays from within the source chamber scintillator volume, however, the source chamber media was replaced by D_2O to produce an unbiased reference sample. A second simulation featuring 200,000 events describing the 4.3-MeV β decay branch of ^{16}N (a 6.1-MeV γ -ray coincident with a β particle from a 4.3-MeV β spectrum) was performed with the source chamber located at the center of the detector. The manipulator carriage assembly was included in the simulation because it contributes to attenuation. The acrylic vessel belly plates were not included because they contribute to the detector geometric anisotropy.

The results are shown in Figure 4.13. The available solid angle, $d\omega$, is plotted as a reference. The isotropy is very high without the source chamber, as expected. The anisotropy due to the chamber is evident in the source chamber simulations.

A calculation was performed to quantify the degree of anisotropy. The fractional deviation of the simulation results from the available solid angle, $d\omega$, are obtained. The results are plotted on the vertical axis of Figure 4.14, while polar angle, θ , is plotted in radians on the horizontal axis. Results in complete agreement with the solid angle would generate values of unity for all polar angles.

The γ -ray simulation without the source chamber (crosses) shows fractional deviations of just a few percent. The data from the simulation including the source chamber is presented with two sets of conditions: events with N_{hit} greater than 30 (stars), and all events (open circles). The simulations suggest that the source chamber imposes a severe anisotropy for polar angle values less than 0.5 radians, suppressing the relative flux at these angles by 25% or greater. The γ -ray flux may be considered

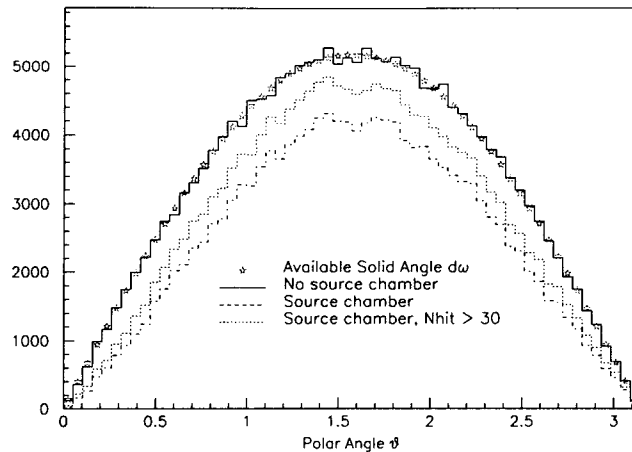


Figure 4.13: Polar angle distributions resulting from 6.129-MeV γ -ray events. The Monte Carlo generation angle is plotted for simulations with and without the source chamber.

isotropic in the range 1-2.2 radians, with moderate, yet symmetric, anisotropy over the range 0.5- π radians. Calibration runs should therefore be carried out 15-20% longer than the time required to attain the desired statistical uncertainty when the data will be evaluated for event position and direction.

4.8 Trigger Efficiency and Yield

Ideally, SNO will be triggered only for those ^{16}N decays that emit a 6.1-MeV γ -ray. The ^{16}N decay scheme is, however, too complex to reliably determine γ -ray energy from β particle energy alone. Therefore our goal is to maximize the trigger efficiency for all ^{16}N decays, and rely on isolating the 6.1 MeV response using other analysis tools.

The trigger efficiency is affected by β particle energy, scintillator photon production and light collection at the PMT, and the PMT threshold. For low β particle energies the photon yield from the plastic scintillator shell decreases such that the

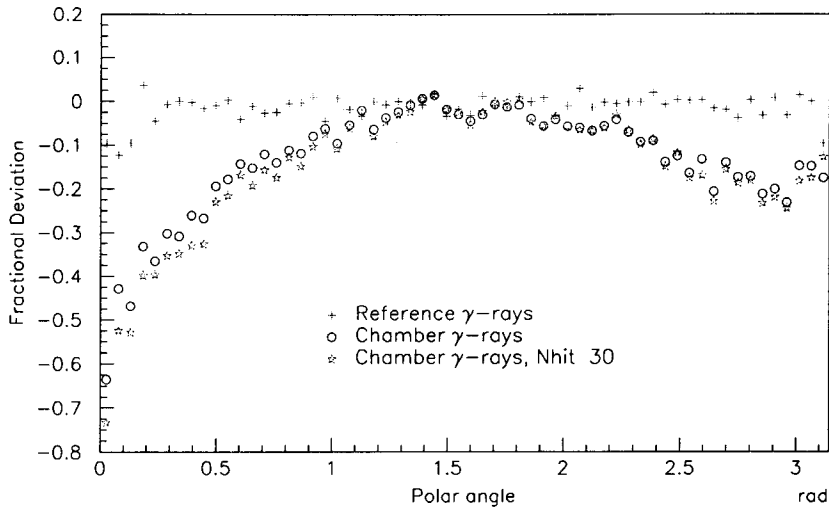


Figure 4.14: The γ -ray isotropy represented as a fractional deviation from the available solid angle. Results from simulations with and without the source chamber are depicted.

probability for the PMT to produce a signal is less than unity. Plastic scintillators require about 100 eV electron energy per photon. Scintillation light is emitted isotropically and the cylindrical shell geometry enhances photon absorption losses, because reflections from the scintillator and steel surfaces will increase the photon path length in the scintillator. The typical PMT has a 30% efficiency for detecting photons, so only one in three photons which reach the PMT are detected. If we make a conservative estimate and assume only 1 in 10 emitted photons reach the PMT, 30 photons are required to obtain a signal. Therefore, approximately 3 keV is a minimum energy deposition to have a single-photoelectron (spe) signal from the PMT. However, a single-photoelectron signal is not sufficient to trigger SNO, as it would be overwhelmed by the noise signal from the PMT (~ 1000 events s^{-1} .) Setting the PMT discriminator threshold high enough to suppress the PMT background signals might raise the minimum e^- energy by a factor of 5, to 15 keV. Fortunately, 99% of β particles from a 4.3-MeV endpoint energy β -decay will have energies exceeding this

limit. The efficiency for triggering with the ^{16}N source is therefore expected to be very high.

A trigger efficiency study was conducted as part of the underground commissioning activities. The signal from the ^{16}N source chamber was used to trigger a nearby 12.7×12.7 cm NaI detector. Background and run coincidence spectra were obtained and analyzed to determine the γ -ray flux in the NaI detector. Corrections for finite NaI detector geometry, total γ -ray branch intensity and estimates of detector efficiency in the range 6 – 7 MeV were applied. The result was a $95 \pm 2\%$ trigger efficiency and an ^{16}N decay rate in the chamber greater than 300 decays per second.

4.9 Run Plan

The calibration goal is to obtain an Nhit spectrum not only for source position, but also emitted γ -ray direction. The Nhit spectrum has been shown to reflect γ -ray interactions in the D_2O , essentially uninfluenced by light from ^{16}N β particle interactions. Simulated results predict the mean Nhit variation with source position will be a few percent. Additionally, the calibration event distribution at a given source point is isotropic to within 15-20% for polar angles greater than 0.5 radians.

The attenuation studies indicate 50% of ^{16}N decays will lead to 6.1-MeV γ -rays interacting in the D_2O . The maximum operating rate for full energy calibration events is therefore approximately 150 per second. There are 82 accessible source positions for calibration based on a 1×1 meter grid arranged in vertical planes defined by the directions toward an AV belly plate and between AV belly plates. This grid is depicted in Figure 4.15.

The number of calibration events required at each source point is compared with the subdivision into directions in Table 4.6. One hour per source position is considered. Low statistical uncertainty may be achieved even with a subdivision into 16 directions per source position. This program would require eight twelve-hour shifts

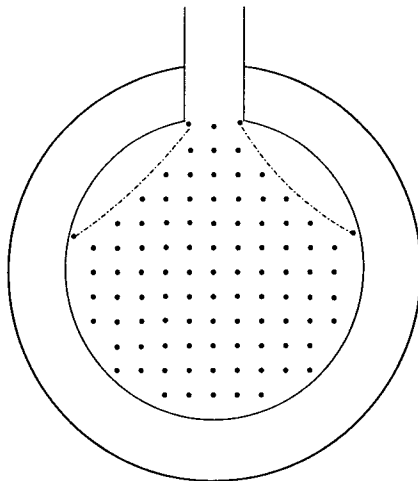


Figure 4.15: The ^{16}N source chamber calibration positions, based on a 1×1 meter grid. The dashed line indicates the source manipulator limit.

to complete. A less intensive calibration may be pursued in consideration of physical limitations on the DT generator lifetime². Two twelve-hour shifts could accomplish this calibration. It is likely that calibrations during detector commissioning would use the less intensive scheme, while the more statistically robust calibration would be performed when the detector had achieved stable operation and low radon backgrounds.

²Tritium and deuterium are exchanged between the target and projectile source during operation. Neutron production efficiencies decrease with time, though the flux is warranted to remain constant for 100 hours.

Directions	Uncertainty (3600 s)	Uncertainty (1000 s)
1	0.14%	0.26%
2	0.19%	0.36%
4	0.27%	0.52%
8	0.38%	0.73%
16	0.54%	1.03%

Table 4.6: Statistical uncertainty per direction resulting from calibration for one hour per source point with 150 s^{-1} 6.1-MeV γ -rays.

4.10 Conclusions

In this chapter the method for conducting energy calibration with ^{16}N has been presented. The interaction between the source chamber and the ^{16}N decay products has been described. Monte Carlo simulations have been performed to show that γ -ray attenuation will have a systematic effect on the the centroid of the Nhit spectrum, lowering the value by 2.3%. Simulations also indicate that β -particles from ^{16}N β -decay will not appreciably affect the Nhit centroid or width. It will be useful to perform independent simulations of bremsstrahlung production from these moderately low-energy electrons.

The γ -ray isotropy of the source is high, though mainly due to attenuation for polar angles less than 0.5 radians. There is a moderate anisotropy which supresses the γ -ray flux by about 15-20% in the remaining polar angle range, which requires additional time at each calibration position to attain sufficient statistical accuracy for most polar angles.

The anisotropy of the SNO detector response to the ^{16}N source as a function of source position has been described, and suggests that mapping the detector response on a 1×1 meter grid is necessary, since the response has a local minimum at the center of the acrylic vessel, rises to a maximum at a radial displacement of 3-4 m, and decreases for larger radial displacements.

The systematic uncertainty created by γ -ray attenuation caused by the source chamber material has been estimated by Monte Carlo. A proposal to deduce the affect experimentally is made in the next chapter. The Nhit response variation as a function of source position is statistically significant to a few $\times 10^{-3}$. This is a characteristic of the SNO detector imposed by finite optical scattering and absorption lengths and anisotropies in the detector itself. The ^{16}N source was developed to map these variations.

5. Systematic Uncertainty of ^{16}N Energy Calibration

The SNO detector Nhit response to 6.1-MeV γ -rays from ^{16}N is affected by two factors. The source container attenuates γ -rays so as to draw the centroid of the Nhit distribution toward lower values. Additionally, the ^{16}N β -decay features a 7.1-MeV γ -ray in approximately 8% of decays. The intensity of this γ -ray is only known to about 10% [117]. The affect of attenuation may be studied by comparison of ^{16}N data with that from an unattenuated γ -ray source. An experiment to establish the relative intensity of 7.1- and 6.1-MeV γ -rays with improved uncertainty has been performed, which will lead to decreased ^{16}N energy calibration uncertainties.

5.1 Unattenuated γ -rays

High-energy γ -rays are required to perform energy calibration in SNO. The methods for producing high-energy γ -rays that are practical in the underground laboratory are the use of short-lived radioactive isotopes, such as ^{16}N , and from the deexcitation of nuclei following neutron capture. The second method requires a neutron source and neutron-capture γ -ray target that may be deployed in the heavy water.

A calibration source has been considered that would feature neutron capture on natural-abundance nickel, that provides a large cross section and high-energy γ -ray cascades. A neutron source, surrounded by a small volume of material suitable to moderate the neutrons to thermal energies, would be enclosed by a few-kilogram mass of nickel. The liability for such a source is that even with an effective moderator, many more neutrons would escape the source to capture on deuterium in the surrounding water than would capture on the nickel. Neutron capture on deuterium releases a single 6.25-MeV γ -ray, that overlaps the Nhit signal from nickel neutron-capture γ -rays. In addition, standard neutron sources, such as ^{244}Cm - ^{13}C , use (α, n) reactions that leave the final nucleus in an excited state that deexcites by emitting high-energy γ -rays (in this case, ^{16}O , emitting a 6.13-MeV γ -ray).

The ideal calibration source would emit low-energy neutrons and also produce very few γ -rays. The decay of ^{17}N by β^- to ^{17}O with $t_{1/2} = 4.13$ s provides a suitable neutron source. More than 95% of the ^{17}N β -decay strength populates levels in ^{17}O that are unbound with respect to neutron decay. The resulting monoenergetic neutrons are emitted with energies (intensities) shown in Table 5.1. Of the remaining branches, 2.18-MeV (0.34%) and 0.814-MeV (3.34%) γ -rays are emitted. These energies are below 2.225 MeV, the photodissociation energy for deuterium, therefore, the only neutrons introduced to the D_2O will be from the ^{17}N β -decay. This isotope is intended for use in measuring the neutron detection efficiency of SNO. Deuterium provides the unattenuated γ -ray calibration source target.

Branch	Energy (MeV)
50.1%	1.171
38%	0.383
6.9%	1.700
0.6%	0.884

Table 5.1: The ^{17}N β -decay neutron branch intensities and energies.

5.1.1 ^{17}N Neutron Source

Production of ^{17}N is achieved using the same facility as that for ^{16}N described in Section 4.1. The ^{17}N will be produced as a gas and transported to a source chamber with plastic scintillator and PMT to generate triggers for SNO. In the case of ^{17}N , the trigger will not be in time with the γ -ray signal, since the mean thermalization time for neutrons with these energies is measured in tens of milliseconds. However, for production rates lower than 10 neutrons per second, the time between events will be sufficient to accurately identify the neutron-capture γ -ray events associated with source triggers.

The reaction $^{17}\text{O}(n,p)^{17}\text{N}$ is produced using 14-MeV neutrons from the DT generator. The cross section has been measured to be 26.1 ± 5.8 mb [118]. The cross section for the reaction $^{17}\text{O}(n,d)^{16}\text{N}$ was measured to be 5.6 ± 1.9 mb. Thus even with a 100% ^{17}O -enriched gas to serve as the target, our production facility will create ^{16}N along with ^{17}N . Fortunately, the γ -rays from ^{16}N β -decay will be in prompt coincidence with the source trigger. The two classes of events, leading to γ -rays with nearly identical energy, may be separated in the analysis. The anticipated production rate is approximately 10-50 events per second using a target enriched to 50% in ^{17}O .

The beauty of using ^{17}N for energy calibration is that the Nhit spectral shape for the unattenuated γ -rays resulting from ^{17}N β -decay is obtained at the same time as the Nhit spectral shape for the attenuated ^{16}N γ -rays. Next we examine how to determine the systematic uncertainty in the attenuated spectrum from the unattenuated spectrum.

5.1.2 ^{17}N Neutron-Capture γ -rays

The ^{17}N β -decay generates a delayed-coincidence between the trigger signal (β) and the neutron signal (neutron-capture γ -ray). The ^{17}N event therefore features two distinct triggers in the SNO data stream. The first is provided by the source, and is of the type EXT. The second is a Nhit trigger resulting from the Čerenkov light produced by the neutron-capture γ -ray. The proximity in time of these two triggers is analyzed to determine if a neutron capture event has occurred. The neutron detection efficiency is determined from the ratio of delayed-coincidence events to the number of neutrons emitted into the D_2O .

The EXT trigger class will also feature ^{16}N events. The prompt $\beta - \gamma$ coincidence has a 72% total branch intensity. The prompt-coincidence events will be readily identified in the off-line analysis. The ground state branch will not have a coincident γ -ray, but its contribution may be deduced from the measured $\beta - \gamma$ rate. The

remaining EXT triggers will be due to ^{17}N decay, with 95% of these events emitting only a neutron.

The time delay imposes constraints on the operation of the source. The mean time delay is about 20 ms between neutron emission and subsequent capture on deuterium. The spectrum of delay times is determined by the cross-section for neutron capture as a function of energy, and the number of times the neutron scatters before capture. The neutron-capture cross-section generally has an inverse dependence on the neutron velocity. The total and capture cross-sections for deuterium are plotted up to 20 MeV in Figure 5.1. The capture cross-section is very small compared to that for scattering. The neutrons engage in elastic scattering with the deuteron, which is essentially at rest with respect to the neutron, favoring large energy and momentum transfer in each collision. The great majority of ^{17}N neutrons will therefore scatter to low energies prior to capture, ensuring that the capture event occurs after the 400 ns trigger window opened by the EXT trigger has elapsed.

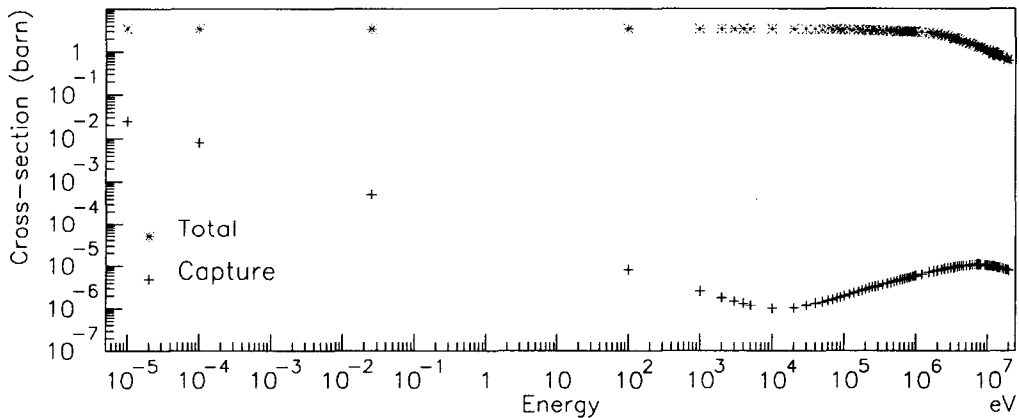


Figure 5.1: The total and capture cross-sections for neutrons by deuterium below 20 MeV.

The rate of capture on deuterium for a particular neutron source emission rate will be somewhat diminished by captures on protons and, to a smaller extent, oxygen in

the D₂O. The likelihood for capture on specific nuclei in the SNO D₂O is determined by the cross-sections for thermal neutron capture and the isotopic abundances. The cross-sections for neutron capture on deuterium, ¹⁶O, ¹⁷O and hydrogen are presented in Figure 5.2. The cross-section for ¹⁶O is low in comparison to that for ¹⁷O, deuterium and hydrogen, particularly for neutron energies above 50-100 keV.

Consideration of the cross-sections illustrates the requirement for very highly-enriched deuterium. The enrichment process also serves to enhance the ¹⁷O abundance by $\leq 50\%$ compared to natural abundances [116]. The relative abundance of target material in the SNO D₂O is given in Eq. 5.1:

$$2 : 1 : 1.3 \times 10^{-3} : 5 \times 10^{-4} (\text{deuterium} : ^{16}\text{O} : ^{17}\text{O} : \text{p}). \quad (5.1)$$

The amount of neutron captures on the small fraction of hydrogen impurity in the D₂O is amplified by the high neutron capture cross-section (332 mb) for thermal neutrons. Neutrons, while not very likely to encounter ¹⁷O, will have a higher cross-section to capture on ¹⁷O compared to ¹⁶O at all energies¹.

A SNOMAN simulation was performed to judge the relative rate of neutron captures to deuterium and oxygen isotopes. The numbers are summarized in Table 5.2. Approximately 42% of neutrons emitted are captured on deuterium. A much higher percentage of neutron captures occur on ¹⁷O compared to ¹⁶O than is understood from the above discussion. The enhanced capture is due to the reaction ¹⁷O(n,α)¹⁴C that has a thermal neutron cross-section of 0.235 b, that is three-orders of magnitude larger than the (n,γ) cross-section for ¹⁶O.

The 42% predicted probability for neutron capture onto deuterium must be considered when selecting the calibration period. The total number of neutron captures exceeds the number of simulated neutron events because of secondary neutron cap-

¹The abundance of ¹⁸O is altered also in the enrichment process. The neutron capture cross-section is nearly identical to that for ¹⁶O, and no high-energy γ-rays are emitted, so it is neglected in this discussion.

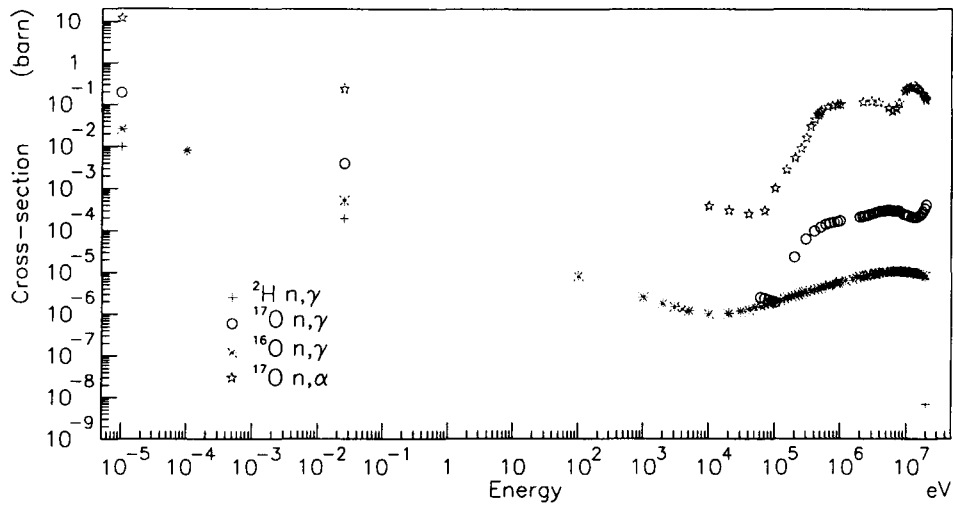


Figure 5.2: The neutron-capture cross-sections are presented for deuterium (^2H), ^{16}O and ^{17}O below 20 MeV. All plots represent n,γ cross-sections, except for n,α on ^{17}O , that is designated with stars.

ture resulting from photodissociation of deuterium by primary neutron capture γ -rays. The neutron rate and/or length of calibration will be adjusted accordingly to attain the desired statistical accuracy. The importance of using D_2O with high isotopic purity is clear when considering the neutrons lost to hydrogen impurities.

Isotope	Events	Percentage
^1H	2793	27.9%
^2H	4132	41.3%
^{16}O	758	7.6%
^{17}O	2338	23.4 %
total	10,021	100.2%

Table 5.2: The percentage of neutrons emitted into the D_2O that capture on the isotopes present in pure D_2O .

The previous section discussed in detail the amount of neutrons capturing on oxygen isotopes. The resulting γ -ray cascades will have total energy of 4.14 MeV

and 8.04 MeV for ^{16}O and ^{17}O respectively, shared between 2 or 3 γ -rays. These events will not affect the peak shape obtained from neutron capture on deuterium, (greater than 99% of neutrons capturing on ^{17}O lead to α particle rather than γ -ray emission), however, a note of caution is in order: the isotopic content of the ^{17}N source chamber must be well characterized, and ideally not include isotopes that emit high-energy neutron-capture γ -rays. The stainless steel source chamber described in the previous chapter is not ideal for these neutron capture studies because Ni, Cr and Fe have thermal neutron cross-sections ranging between 1-10 b. These isotopes also emit high-energy γ -rays in the range 7-10 MeV. Simulation predicts that 25% of neutrons would capture on the stainless steel source chamber used for ^{16}N energy calibration. Analysis to discriminate between neutron capture on deuterium and on the source chamber is possible by fitting the Čerenkov production position, however, this causes further losses in yield.

5.1.3 Gamma Ray Peak Shape

The ^{16}N Nhit spectrum has three major components: the 6.1- and 7.1-MeV γ -ray peaks and a broad feature peaked near the low-energy tail and with its own high-energy tail to about 60 Nhits. The broad feature results from γ -rays that scatter, and bremsstrahlung produced, in the source chamber. Once the single γ -ray Nhit peak shape is known, the ^{16}N Nhit spectrum will be decomposed to reveal the response to both the 6.1- and 7.1-MeV γ -rays.

A fit to characterize the simulated peak shape for the ^{17}N β -decay sources was performed. An Nhit spectrum was obtained for 200,000 simulated neutrons released from the D_2O source chamber scintillator volume, while the source chamber media was defined as D_2O . The peak is moderately well described by a fit to a Gaussian distribution with $\chi^2/\text{ndf} = 2.4$, as shown in the upper left panel of Figure 5.3. An improved fit with $\chi^2/\text{ndf} = 0.996$ (lower left panel) is obtained to the function shown

in Eq. 5.2 that is the product of a Gaussian distribution with an empirically selected function.

$$par(1) * exp(par(2) * [(Nhit - par(3))/par(4)]^2) * (1 + par(5)cos(Nhit/par(6))) \quad (5.2)$$

The variable $par(5)$ determines the magnitude of correction and $par(6)$ specifies the frequency of the cosine correction. The modified Gaussian function is plotted against the data in the right hand panel of Figure 5.3.

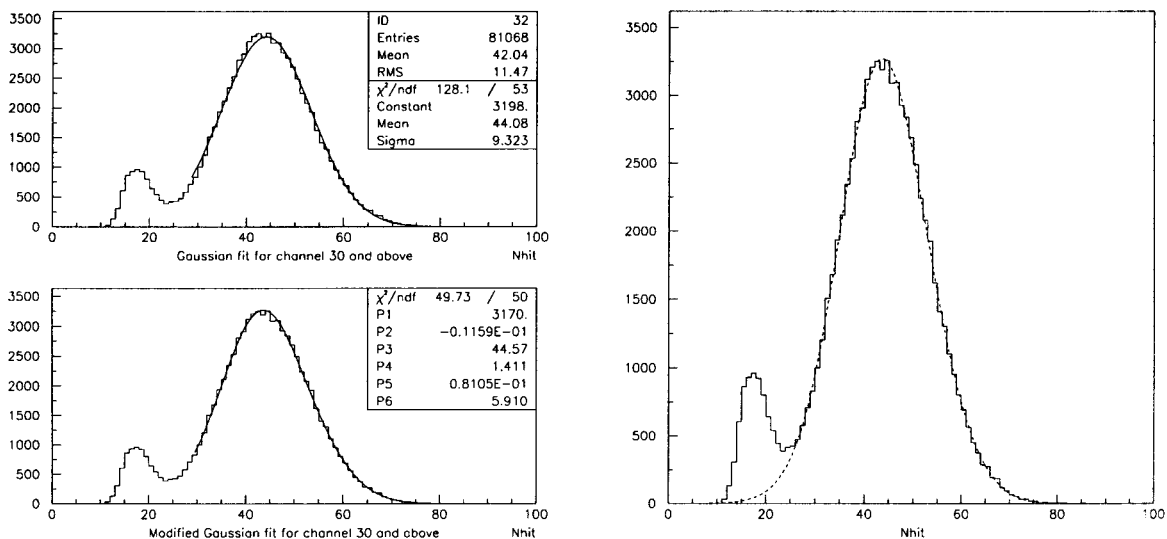


Figure 5.3: The results of a fit to the monoenergetic, unattenuated γ -ray from neutron-capture on deuterium, showing the number of events plotted against Nhit. Channels 30 and above are included in the fits, shown in the left panel. The corrected function is then plotted over the full Nhit range along with the data in the right panel.

5.1.4 Fitting ^{16}N Nhit Spectrum

The fit parameters characterizing the unattenuated γ -ray peak shape may be applied to the ^{16}N Nhit spectrum to determine the relative contribution of the 6.1-

and 7.1-MeV γ -rays, however, the influence of attenuated ^{16}N γ -rays on the Nhit spectrum must first be determined. Figure 5.4 shows the Nhit contribution from full energy γ -rays and from those that have been scattered in the source chamber. This data fits to a third-order polynomial, and is removed to produce a corrected spectrum due to the unattenuated γ -rays.

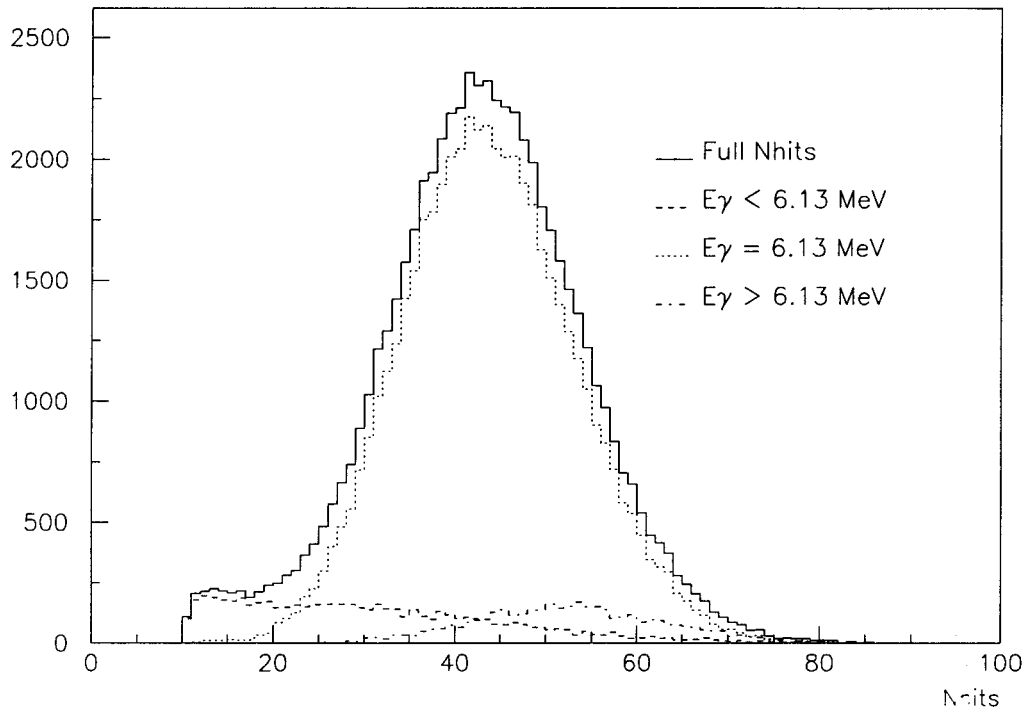


Figure 5.4: The ^{16}N Nhit spectrum (solid line) decomposed for contributions from full energy 6.1- and 7.1-MeV γ -rays, and from γ -rays and β -particles that interact in the source chamber.

The fit to two modified Gaussian functions is carried out by fixing the modification function parameters and the Gaussian widths. The height and centroid of the Gaussians are allowed to vary. The goodness of fit achieved is 1.12, and the fitted spectrum is shown in Figure 5.5. The fit reports 6.96 ± 0.35 Nhit separate the centroids of the two Gaussians. The energy difference between the two γ -rays is 0.987 MeV, therefore the number of PMTs hit per MeV is 7.05 ± 0.35 .

This technique is promising, provided a high accuracy determination of the deuterium neutron-capture γ -ray Nhit spectrum is obtained. However, it will be difficult to reduce the systematic errors below 1%, due to the poor energy resolution of SNO, which makes it impossible to fully resolve the 6.1- and 7.1-MeV γ -rays from ^{16}N . Nevertheless, pursuing this measurement will help to understand systematic influences on the ^{16}N Nhit spectrum from source chamber γ -ray attenuation and also provide additional verification of the SNOMAN Monte Carlo.

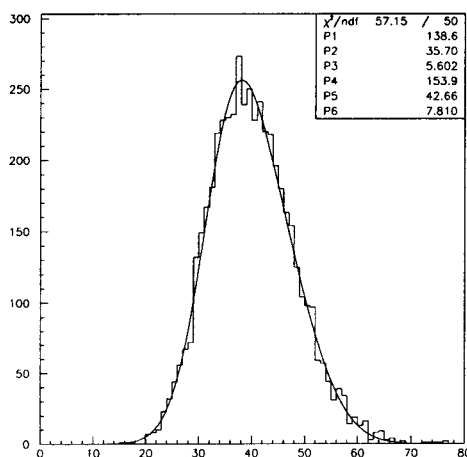


Figure 5.5: The ^{16}N Nhit spectrum corrected for γ -rays scattered by the source chamber. The fit is to two Gaussian distributions.

5.1.5 Analysis Considerations

The primary goal of ^{17}N is to determine the neutron efficiency. With minor considerations an accurate determination of the unattenuated single γ -ray Nhit spectrum may be obtained. Application of this spectral shape to the ^{16}N energy calibration analysis will help determine not only the 6.1-MeV γ -ray calibration more accurately, but also enhance our ability to separate the 7.1-MeV γ -ray contribution, possibly with sufficient accuracy to provide a second calibration point in this sensitive energy calibration range.

The radial distribution of the ^{16}N and ^{17}N Čerenkov events will differ. The direct production of γ -rays within the source resulting from ^{16}N decay causes most of the Čerenkov light to be generated within one radiation length (approximately 50 cm) of the source chamber. Compton scattering and pair production will create electrons and positrons moving generally in the direction of the incident γ -ray, which is away from the source chamber. In the case of neutron capture, the neutrons will diffuse away from the source chamber prior to capturing on deuterium, though they will make a random-walk through the D_2O , rather than take a straight-line path like the γ -rays. The emission of neutron-capture γ -rays following capture will be isotropic. Figure 5.6 presents simulated radial locations for ^{16}N and ^{17}N events.

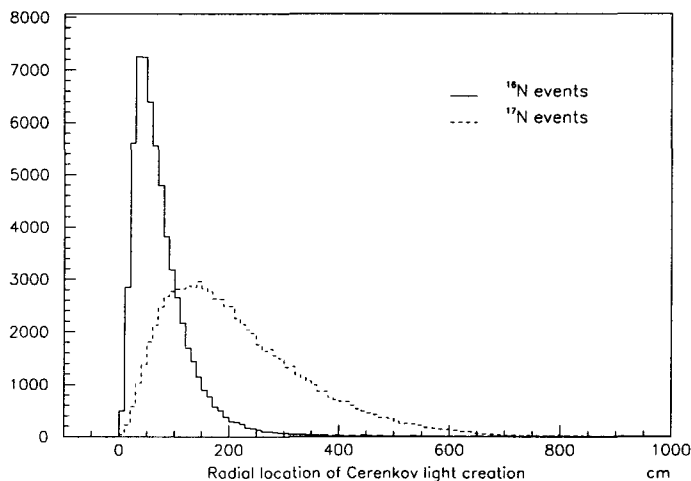


Figure 5.6: The simulated radial distribution of Čerenkov light vertices from ^{16}N and ^{17}N in pure D_2O . The source chamber is not present in the ^{17}N simulation.

At present, the event fitters which calculate the production vertex and emission direction for Čerenkov light have a positional accuracy of about 20 cm. This is sufficient to allow for a sampling of ^{17}N calibration events as a function of position. This is distinct from the ^{16}N case, where the source chamber is moved to map the SNO response. Since the ^{17}N neutrons capture at a mean distance of about 1.75

m from the source chamber, and the mean distance for γ -ray interactions is 0.5 m, calibration with the source at the center of the detector provides for a broad sampling of the detector volume.

An important consideration is how to obtain the data to best achieve the above goals. The ^{17}N γ -rays will be emitted much further from the source than the ^{16}N γ -rays, introducing uncertainties into the analysis of the Nhit centroid as was shown in the previous chapter. The solution is to take data in the following manner. Six measurements should be obtained with the source located at a distance of 1.75 meters from the center of the detector. The source should be located along the major axes of the detector. The data from the six locations will be analysed and those events fitting within 1 m of the center of the acrylic vessel will be combined and compared with the ^{16}N γ -ray Nhit spectrum. In addition to the fit by position, the data will be fit for direction. The data fitting in the target region may be studied for anisotropies that reveal how much scattering of light occurs from the source chamber. Finally, this group of six source chamber positions provides a high neutron flux distributed throughout the D_2O to a radius of 4 m, from which neutron detection efficiency will be calculated.

This procedure not only removes the systematic influence associated with neutron-capture γ -ray events away from the center of the detector, but it also allows the removal by analysis of γ -ray events arising from neutron capture on the steel of the source chamber through fitting the event vertex. SNOMAN simulation suggests that about 25% of neutrons emitted in pure D_2O will capture on the Fe, Cr and Ni in the source chamber. Gamma-ray energies (in cascades and singles) decidedly not equal to 6.25 MeV will result. The results of these simulations also suggest that neutron capture on the material of the source chamber should be carefully considered in the neutron detection efficiency analysis.

5.2 The 6.13- and 7.12-MeV γ -ray Relative Intensity

The analysis of ^{16}N data has two goals:

1. Verification of the SNOMAN simulation
2. Determining an absolute energy calibration

The strength of ^{16}N as a calibration source is that more than 90% of γ -rays are emitted at 6.13 MeV. However, the majority of the remaining γ -rays are emitted at 7.12 MeV. SNO is incapable of resolving these two γ -rays. The Table of Isotopes (TOI) [117] specifies that the β -decay to the 7.12-MeV excited state in ^{16}O has an intensity of 4.9 ± 0.4 . This 8% uncertainty in the 7.12-MeV γ -ray intensity carries forward to the uncertainty in the relative intensity of the 6.13- and 7.12-MeV γ -rays. The relative intensity determines the mean γ -ray energy that will be associated with ^{16}N calibrations: $E_{mean}^{\gamma} = 6195.91 \pm 84.19$ keV. This would be the major systematic uncertainty on the ^{16}N absolute energy calibration. It also affects the uncertainty in performing Monte Carlo verification. As a result of this realization, an experiment to reduce this uncertainty was performed.

5.2.1 Experiment

The 88" cyclotron at Lawrence Berkeley National Laboratory (LBNL) was used to produce high-energy neutrons for the production of ^{16}N . A beam of 40-MeV deuterons impinged on a thick Be metal target. The spallation of the deuterons produced neutrons with approximately half the incident kinetic-energy of the deuterons. The low Z of Be metal minimized the attenuation of the neutron flux while also acting to stop all of the protons in the target. The highly forward scattered 14+ MeV neutrons then passed through a cylindrical acrylic cell (inner radius and height both 1") enclosing 3.14 in.³ of water. The activity resulting from $^{16}\text{O}(n,p)^{16}\text{N}$ reactions was transported via a water hose from Cave 0 to the atrium just outside Cave 1, located

25 m distant. A 85% efficient high purity Germanium (HPGe) γ -ray detector was used to register decays from an acrylic water cell with dimensions identical to that used as the target. The water flow was one gallon per minute. Singles spectra were obtained using the NOMAD data acquisition system from EG&G ORTEC. Four runs were performed and the source to detector distance was varied along with attenuation properties and the source geometry. Table 5.3 shows the parameters of interest:

Run	Source	Distance	Attenuation
1	Water Cell	3.5"	3.5" polyethylene
2	Water Cell	3.5"	none
3	Water Cell	7"	none
4	Water Line	7"	none

Table 5.3: Source characteristics of the ^{16}N runs.

5.2.2 Analysis

Our goal is to determine the relative intensities of the 6.13- and 7.12-MeV γ -rays. It is therefore necessary to know the Ge detector efficiency at 7.12 MeV. In general terms, the efficiency is determined by the intrinsic ability of the detector to capture the full-energy from a γ -ray. Since γ -ray interactions in matter are stronger for high-density materials, detector efficiency increases with electron density, which is linked with proton number. The ratio of protons in iodine and germanium nuclei is about 5/3, accounting for the greater efficiency of NaI(Tl) detectors compared to Ge detectors. The much better energy resolution afforded by the use of a high-purity Ge detector is required for this experiment.

The geometry between the source and detector also influences the efficiency. The solid angle subtended by the detector with respect to the source is generally used to define the geometry. This assumption implies equal probability of detection for γ -rays

entering any region of the detector. For a cylindrical detector, such as used in this experiment, that assumption is not true, but it is consistent for both the calibration source and the experimental source. The absolute efficiency is therefore given by the product of the intrinsic efficiency and the geometric efficiency: $\epsilon_{\text{abs}} = \epsilon_{\text{intr}}\epsilon_{\text{geom}}$.

The γ -ray counting rate, R , at the detector is related to the γ -ray source intensity, I , by $R = I\epsilon_{\text{abs}}$. Since our goal is to determine the relative γ -ray intensity, consider the ratio of the counting rates at two energies:

$$\frac{R^1}{R^2} = \frac{I^1\epsilon_{\text{abs}}^1}{I^2\epsilon_{\text{abs}}^2} \quad (5.3)$$

Measuring the counting rate from a source or sources with known γ -ray intensity allows the determination of the efficiency at one energy relative to another. The geometric efficiency can be considered the same for γ -rays with similar energy. Even if the geometric efficiency is not the same, taking the ratio in Eq. 5.3 removes the need to specify the geometric efficiency at all.

This technique was employed in two ways to determine the relative efficiency. The first involves extrapolating from efficiencies determined with lower energy γ -rays from calibrated sources by fitting the efficiency over a broad energy range. The second involves Monte Carlo simulation of the detector efficiency constrained by data from calibration sources.

5.2.2.1 Low-Energy Calibrated Sources

The detector efficiency relative to 2.598-MeV γ -rays was obtained by filling a water cell with a solution containing ^{56}Co . Counting was performed using the same geometries (3.5" and 7" source-detector distance) as for the ^{16}N source water cell. The ^{56}Co γ -ray energies, their absolute intensities as a percentage of decays, the measured intensities at 7.0" and the relative efficiency normalized to the 2.598-MeV line are shown in Table 5.4 for those γ -rays that appear in greater than 5% of decays.

Energy (MeV)	Intensity (%)	peak area	eff($E/2.598$)
0.846	99.933	2446265	1.848
1.037	14.13	312398	1.669
1.175	2.239	52149	1.759
1.238	66.07	1366659	1.562
1.360	4.256	84548	1.499
1.771	15.49	247107	1.205
2.015	3.029	46071	1.148
2.034	7.771	118618	1.153
2.598	16.96	224624	1.000
3.202	3.13	35565	0.858
3.253	7.62	86717	0.859
3.272	1.78	20302	0.861

Table 5.4: ^{56}Co γ -ray energies and intensities (given as the percentage of decays in which the γ -ray is observed). The observed peak area and detector efficiency relative to 2.598 MeV is shown for the 7" geometry. The intensities are known with less than 0.3% uncertainty, with the exception of the 3.253-MeV γ -ray, that has 3% uncertainty.

The area under the full-energy peak was obtained for each γ -ray using the Maestro software package. The peak areas were given equal weight and fit to a function, shown in Eq. 5.4, commonly used to calibrate germanium detector efficiency, ϵ , above 200 keV [119].

$$\epsilon = a_1 \exp(-a_2 E) + a_3 \exp(-a_4 E) \quad (5.4)$$

The germanium detector efficiency at 6.1 MeV was determined in a similar fashion. The ^{16}N data was analyzed to obtain the peak area for the 2.741-, 6.129- and 7.117-MeV γ -rays. The relative efficiency between the 6.129- and 2.741-MeV γ -rays was calculated directly from the peak areas, and determined to be $42.96 \pm 3.26\%$. The fit parameters obtained from the ^{56}Co efficiency calculations were used to calculate the detector efficiency at 2.741 MeV relative to 2.598 MeV. The detector efficiency at 6.128 MeV was then obtained relative to 2.598 MeV, and found to be $44.40 \pm 3.37\%$. A new fit to Eq. 5.4 was performed including the efficiency at 6.129 MeV. The fit

parameters were used to calculate the efficiency at 7.115 MeV, and that efficiency relative to 6.129 MeV was determined to be $85.35 \pm 7.42\%$.

The relative intensity of the 7.115-MeV γ -ray to the 6.129-MeV γ -ray was found to be $7.596 \pm 0.664\%$. This value is consistent with the TOI, but the systematic uncertainty is no better, and our goal is not accomplished. The systematic uncertainty in the relative efficiency is dominated by the uncertainty in the 2.741-MeV γ -ray intensity: 0.82 ± 0.06 , or 7.3%. If an independent measurement of this γ -ray intensity is made, this analysis may be repeated to provide the high accuracy relative intensity for the 7.1-MeV γ -ray relative to the 6.1-MeV γ -ray.

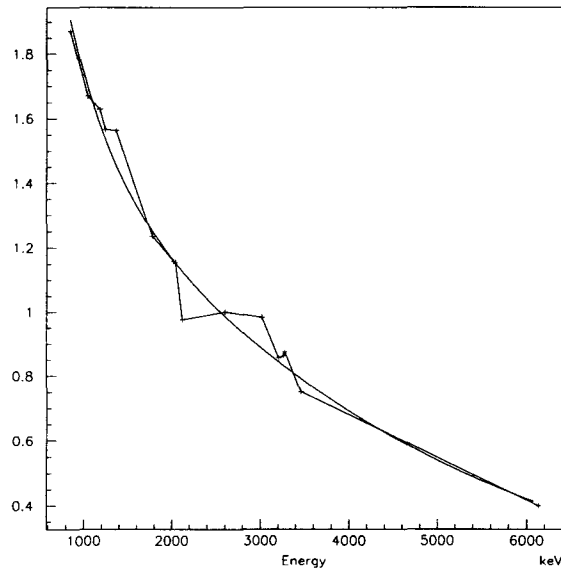


Figure 5.7: The Ge detector efficiency relative to the 2598 keV γ -ray, as determined from the ^{56}Co and ^{16}N water cell sources.

The present data can be used to determine the Ge detector efficiency without relying on the 2.7-MeV γ -ray from ^{16}N . Simulation of γ -ray transport was used to predict the Ge detector efficiency while considering the water cell geometry and the γ -rays of interest from ^{16}N β -decay. The accuracy of the simulation will be checked using the data from ^{56}Co β -decay.

5.2.2.2 Simulation with GEANT

The Ge detector was simulated by M. Hindi using the GEANT Monte Carlo simulation. This package was obtained from the CERNLib library [120] of high-energy physics analysis software produced and maintained at CERN. The relevant dimensions to describe the detector and the water cell were applied. Simulations of 100,000 6.13 and 7.12-MeV γ -rays were performed separately. The decays were generated randomly in the volume of the source and constrained to be emitted in the 2π hemisphere which contained the detector. The restriction on solid angle was to reduce the time required for the simulation. Back scattering of a γ -ray in the source volume that was initially directed away from the detector would reduce the γ -ray from full energy, and therefore these events would not contribute to the full energy peak, nor to the escape peaks, and thus would have no impact on the determination of the relative efficiency. Comparing the events in the full energy peaks of the two simulations the relative efficiency was found to be $83.8 \pm 0.27\%$.

The accuracy of the GEANT calculations was estimated by the following comparison. The liquid source of ^{56}Co was counted in the same geometry as the ^{16}N water source. The detector response to γ -rays with the ^{56}Co energies was simulated. Each γ -ray was simulated to 0.3% statistical uncertainty. The 2.598-MeV line was selected as the reference, and relative intensities were determined for all other lines. The relative intensities for simulation and data are plotted as a function of energy in the top panel of Figure 5.8. The percent deviation of the simulated values from the data is shown in the lower panel. Calculations to lower energy are overestimated, while those to higher energy are underestimated.

A correction to the efficiency change of $-16.2 \pm 0.32\%$ estimated for 7.12 MeV relative to 6.13 MeV may be obtained from the ^{56}Co comparison. Consider the percent deviation between simulation and data for ^{56}Co as a function of change in efficiency (Figure 5.9. Increase in efficiency is toward lower energy, while decreasing

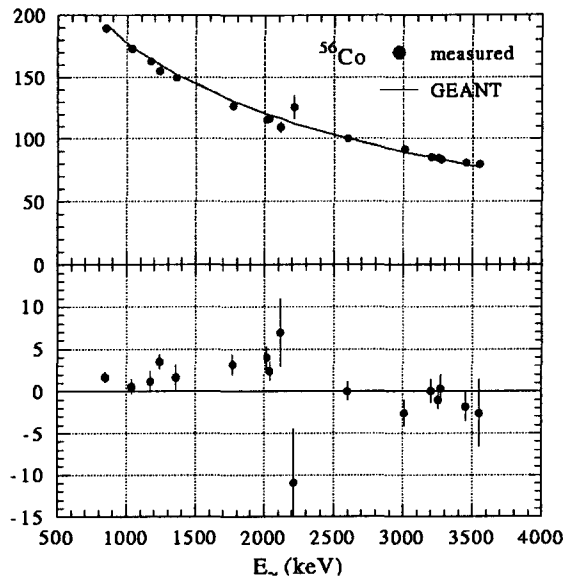


Figure 5.8: Top panel: Relative efficiency as a function of energy from ^{56}Co data and GEANT simulation. Bottom panel: Percent deviation of simulated efficiencies from data as a function of energy.

efficiency is toward higher energy. The ^{56}Co data suggest that for a -16.2% change of efficiency, the simulation overestimates by 0.4% . The efficiency change is therefore $-15.8 \pm 0.15 \pm 0.30\%$, where the first uncertainty is statistical and the second is related to the overestimate. The overall efficiency change is $-15.8 \pm 0.35\%$, providing a relative efficiency of $84.2 \pm 1.86\%$.

The relative intensity, $R_{6.1}^{7.1}$, may now be calculated. The results for the $3.5''$ and $7''$ geometries along with an average are presented in Table 5.5. The uncertainty in $R_{6.1}^{7.1}$ is 1.7% , a factor of 4 improvement over the value in the TOI.

Distance	Relative Intensity (%)
$3.5''$	$7.730 \pm 0.185\%$
$7''$	$7.700 \pm 0.184\%$
Average	$7.715 \pm 0.131\%$

Table 5.5: The relative uncertainty of the 7.1- and 6.1-MeV γ -rays from ^{16}N β -decay resulting from the GEANT Ge detector efficiency Monte Carlo.

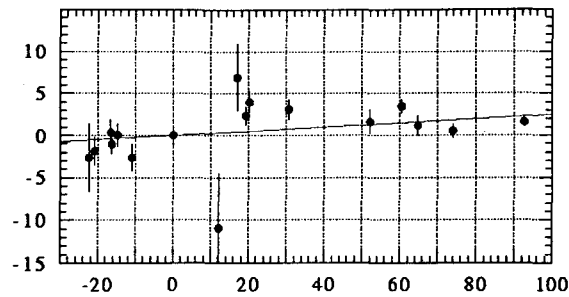


Figure 5.9: Percent deviation of simulated efficiency from data as a function of change of efficiency.

5.2.2.3 Simulation with MCNP

A further check on the simulated result is obtained through use of an independent simulation code. The MCNP [121] code produced by Oak Ridge National Laboratory was used because a simulation of the Ge detector used for this experiment was already well calibrated at low-energy due to the efforts of R. Donohue, D. McDonald and A. Smith at LBNL. The efficiencies calculated at 6.129- and 7.115-MeV are 0.1015% and 0.08668%, respectively, with 0.5% statistical uncertainty: no estimate of the systematic uncertainties are provided. The relative efficiency is therefore $85.31 \pm 0.60\%$. This result confirms the value obtained from the GEANT simulation, where we have included an estimate of the systematic errors.

5.2.3 Results

The relative efficiency of the Ge detector was obtained using two methods. The result using the fit and extrapolation from the low-energy calibration was consistent with the TOI. Unfortunately, it did not improve on the uncertainty reported in the TOI. The second technique was to estimate the detector efficiency using Monte Carlo simulations. The GEANT simulation package was used to find a result uncertain to approximately 2%, that is a factor of 4 improvement over the result in the TOI. The GEANT determination was verified by other researchers with an independent Monte

Carlo simulation using MCNP. The final estimate of the relative intensity, $R_{6.1}^{7.1}$, was averaged over the two experimental source-detector distances to provide:

$$R_{6.1}^{7.1} = 7.715 \pm 0.131\% \quad (5.5)$$

The mean γ -ray energy from the weighted average of the 6.13- and 7.12-MeV branches from ^{16}N β -decay is therefore $6.199 \pm 0.12 \text{ MeV}$.

5.3 Summary

In the previous chapter we found by simulation that attenuation by the source chamber material shifted the ^{16}N Nhit spectrum centroid to lower values by 2.3%. A direct measurement of this affect is not possible using the existing stainless steel source chamber, however, the source chamber's influence may be inferred by comparison with neutron-capture γ -rays from ^{17}N . Not only are the attenuation effects eliminated, but by fitting the Čerenkov light production vertex and direction, the light scattering from the source chamber may also be quantified.

The experiment to measure the relative intensity of 6.1- and 7.1-MeV γ -rays with high precision leads to a weighted average of γ -ray energy emitted by the ^{16}N source. The ^{17}N neutron-capture γ -ray Nhit spectrum provides the response of the SNO detector to a mono-energetic, unattenuated 6.25-MeV γ -ray. While it may not be possible to fit the composite ^{16}N spectrum with high accuracy to functions representing the 6.1- and 7.1-MeV γ -rays, making an independent measurement at an energy matching the weighted average is very desirable. The measurement not only enhances our energy calibration, but provides additional information to verify the SNOMAN Monte Carlo, thus satisfying the two goals of energy calibration.

6. Low Energy Calibration of SNO with ^{24}Na

All particle energy detectors have a threshold below which no useful signal may be obtained. The properties of the detector itself lead to an intrinsic threshold, while specific the operating environment may impose thresholds at greater energy. The emission of scintillation light from Tl dopant atoms following ionization in the bulk material caused by radiation is the basis for the signal from a NaI(Tl) detector. The energy required in NaI(Tl) to produce a photon is 25 eV. Under most, if not all, circumstances environmental influences create many events which surpass this intrinsic threshold to establish an effective threshold.

An additional characteristic for energy spectroscopy is to know the relation between particle energy and output signal over the range of energies which are to be measured. If the response is known to be linear, then the response may be calibrated by making measurements at two energies. If the response is unknown, or known to be non-linear, then the response must be determined regularly throughout the energy range of interest.

The PMTs in SNO will be operated to detect single photons. This approaches the intrinsic threshold for a PMT, therefore many physical processes which occur in the local environment will lead to events in the detector. All processes which are not the result of solar neutrino or supernovae neutrino interactions constitute the detector background. As a result, there will be an effective threshold below which it will be impossible to separate signal from background. Radioactive decays will generate β particles and γ -rays with combined energy up to 5 MeV. These particles will produce Čerenkov light. Since the majority of the radioactive contaminants are in the AV and the PSUP, most of these background events will occur outside a radius of 550 cm and their contribution will be reduced during analysis.

It is known that SNO will have a minimum energy sensitivity to solar neutrinos due to radioactive backgrounds. The contribution from radon (^{222}Rn , $t_{1/2} = 3.8d$)

will be a transient background, while ^{238}U , ^{232}Th and ^{40}K will present a steady background. The threshold for SNO is expected to be near 5.5 MeV. If the initial radon load provides a large contribution to the background rate, the threshold may drop somewhat after the first 40 days of operation following radon sealing.

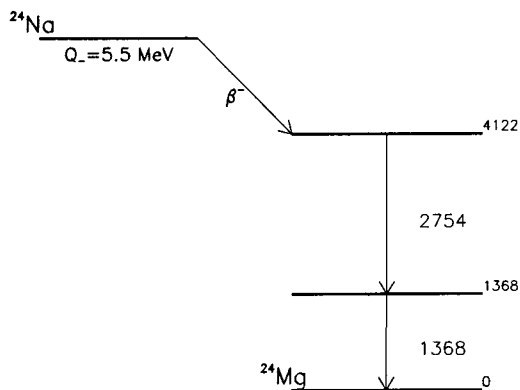
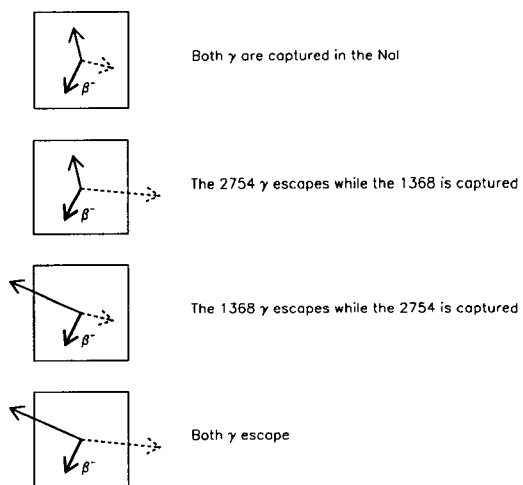
An activated NaI(Tl) detector will be used to provide energy calibration below threshold. The energy signal from the β decay of ^{24}Na inside the NaI(Tl) crystal will be used to trigger SNO to look for light from the coincident γ -rays. This energy calibration allows for the understanding of detector response below the effective threshold signal, leading to more accurate analysis for events near threshold. In addition, the source provides a means to directly assess the detector response to low energy γ -rays associated with radioactive backgrounds. Knowledge of the response of SNO at these energies will be important when this collaboration addresses the issue of deviation of the shape of the charged current spectrum.

6.1 Investigation of ^{24}Na in NaI

The use of an activated NaI detector as a means to calibrate the Sudbury Neutrino Observatory (SNO) at energies below 5 MeV has been discussed and investigated previously [122]. A detailed analysis of spectra obtained from an activated 7.62×7.62 cm NaI detector in coincidence with a 30×30 cm NaI annulus is provided.

6.1.1 Theory

NaI is an inorganic crystal consisting of the isotopes ^{23}Na and ^{127}I . The isotopes ^{24}Na and ^{128}I may be created through thermal neutron activation, and the $t_{1/2}$ are 15 hours and 25 minutes, respectively. The decay of ^{24}Na (Figure 6.1) is by means of β^- decay ($Q_- = 5.5$ MeV) nearly always followed by the emission of two prompt γ -rays with energies 2.754 and 1.368 MeV (γ_{2754} and γ_{1368}). The maximum energy of the β^- is 1.390 MeV, and it is expected that the β^- will not escape the NaI detector.

^{24}Na Decay SchemeFigure 6.1: The decay scheme of ^{24}Na .Escape of γ from NaI CrystalFigure 6.2: Schematic of coincidence detection of ^{24}Na .

It is expected that the prompt γ -rays will be detected in one of four ways (Fig. 6.2):

1. Both γ -rays will deposit full or partial energy in the activated NaI detector.
2. The γ_{2754} will escape and the γ_{1368} will deposit full or partial energy in the detector.
3. The γ_{1368} will escape and the γ_{2754} will deposit full or partial energy in the detector.
4. Both γ -rays will escape.

The signal from the activated detector will be used to trigger the SNO detector to look for Čerenkov photons produced by the emission of either or both of the ^{24}Na γ -rays. The possibility of partial energy deposition in the activated detector exists, but with judicious selection of gating in the analysis these events will not adversely affect the calibration.

6.1.2 Procedure

A BICRON 7.62×7.62 cm NaI detector was covered by a plastic bag and surrounded by burlap bags filled with polyethylene beads in a shielded enclosure. Two 56 mCi ^{241}Am - ^9Be neutron sources were placed in the enclosure on opposite sides of the bag. Neutrons result from the reaction $^9\text{Be}(\alpha, n)^{12}\text{C}$, facilitated by ^{241}Am α decay. Each source provided a neutron flux into 4π of approximately 1.5×10^5 neutrons/second. The sources were 30 cm removed from the detector. The detector was irradiated with neutrons for 24 hours.

The activated detector was then placed inside an annular 30×30 cm NaI detector and coincidence counting was performed using the activated detector signal to trigger the annular detector. The LBL Starburst/CHAOS data acquisition system [123] was used to obtain data over a period of 3 days. A series of three ten-minute spectra

were taken to demonstrate the decay of ^{128}I during the first half hour of counting, and additional spectra taken over approximately 24 hours were obtained to assess the decay characteristics of the ^{24}Na .

6.1.3 Analysis

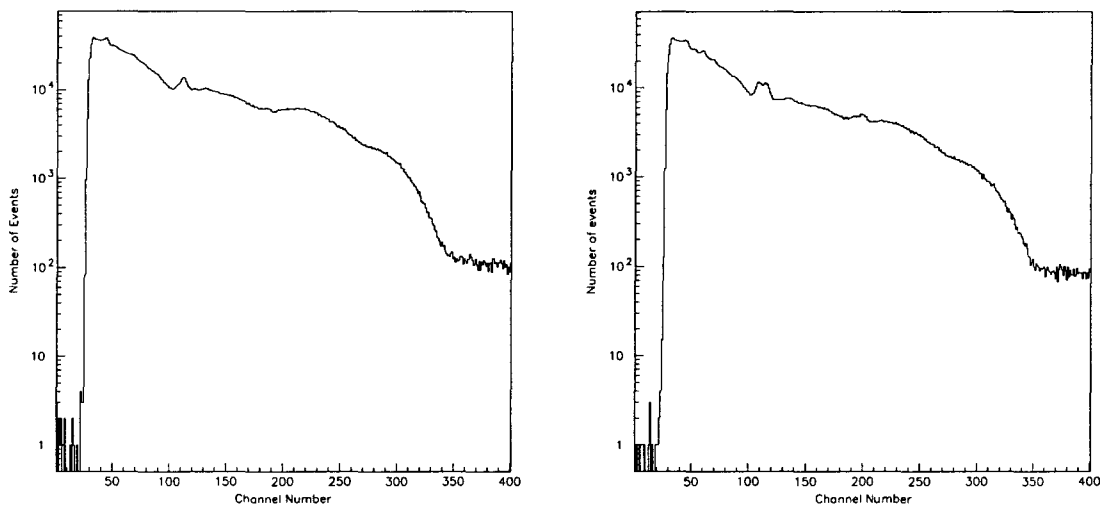


Figure 6.3: Neutron activated NaI energy spectra. The peak at channel 112 is due to ^{40}K . Left panel: ^{241}Am - ^9Be neutrons thermalized by polyethylene beads. Right panel: ^{241}Am - ^9Be neutrons.

The spectrum obtained from the activated NaI detector is shown in the left panel of Fig. 6.3. Four distinct β spectra appear, and are associated with the four energy deposition modes. Comparison with the spectrum from the earlier study (right panel) shows that the single peaks in the spectrum at energies of 1.368 and 2.754 MeV (channel 120 and 200, respectively) are removed. These peaks in the earlier spectrum are due to decays in which the beta energy is not deposited in the activated detector, and only one gamma deposits energy in the activated detector. This situation occurred because there was no attempt to moderate the neutrons emitted from the ^{241}Am -Be neutron source during the earlier investigation. The neutrons are emitted at energies

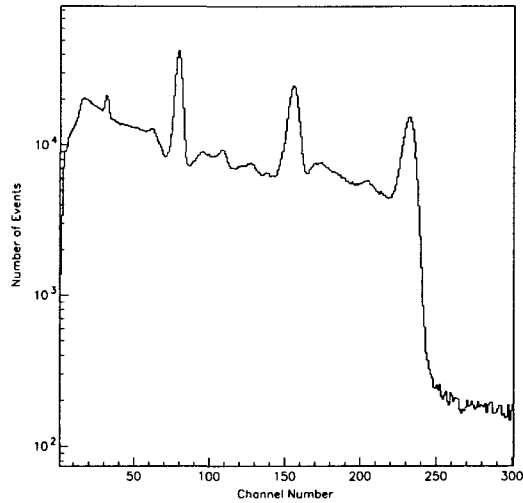


Figure 6.4: Spectrum of NaI Annulus in coincidence with Activated NaI detector.

up to 11 MeV, and the cross-sections of (n,x) reactions on the material of the detector covering and the reflective coating located between the crystal and the cover which may lead to production of ^{24}Na . The detector covering contains aluminum, while the reflective coating is a layer of magnesium oxide packed between the crystal and the cover. Reactions of particular interest are $^{24}\text{Mg}(n,p)^{24}\text{Na}$, and $^{27}\text{Al}(n,\alpha)^{24}\text{Na}$. For neutron energies of 5 MeV these reactions have cross-sections two orders of magnitude greater than that for $^{23}\text{Na}(n,\gamma)^{24}\text{Na}$. The decay of ^{24}Na in the detector cover or the reflective coating will likely not allow the β particle to deposit energy in the detector, leading to the observation of single energy γ -escape peaks. These are not desirable, as these would be untagged γ -rays in the SNO D_2O .

The spectrum from the NaI annulus clearly shows the γ -rays which escape the activated detector (Fig. 6.4). Gates were established on the peaks of the annulus spectrum to determine which features in the activated spectrum were associated with the emission of the γ_{1368} , γ_{2754} or both γ -rays. Gates were also set on the energy spectrum of the activated detector and optimized by consideration of three criteria:

1. The ratio of counts in the full energy peak in the annulus to the total triggers in the activated detector gate.
2. The ratio of counts in the full energy peak in the annulus to the total counts in the gated annulus spectrum.
3. The ratio of the full energy peak in the gated annulus spectrum to other full energy peaks.

These criteria lead to the selection of the following gates in the activated detector and provide ratios of γ -ray peaks for use in SNO calibration shown in Table 6.1.

calibration peak	competing peak	ratio calibration/ competing peak	peak/ triggers	peak/ total	energy of gate (MeV)
1368	2754	203:1	.284	.328	2.85-3.27
2754	1368	4.2:1	.265	.276	1.59-2.15
4122	1368	1.2:1	.110	.138	0.69-0.97
4122	2754	1.4:1	.110	.138	0.69-0.97

Table 6.1: Selection criteria results for energy gates.

These results suggest that a very high signal to noise ratio will be attainable for calibration of SNO with the γ_{1368} (fig. 6.5). Lower signal to noise ratios are attainable for calibration to the γ_{2754} and the sum peak. The ratios presented rely on the full peak efficiencies of the NaI annulus. It is expected that the full peak efficiency for SNO will be higher. SNO will also provide a true 4π detector geometry. The annulus achieves 93% of 4π for the activated NaI detector, but it also presents short paths for full energy deposition due to its finite geometry, which will not be the case in SNO. Therefore, the ratio of signal to noise presented above should be considered a very conservative lower limit.

The method of NaI activation by thermal neutrons may be used to produce event rates on the order of 0.1-10 events per second for neutron sources similar to those used

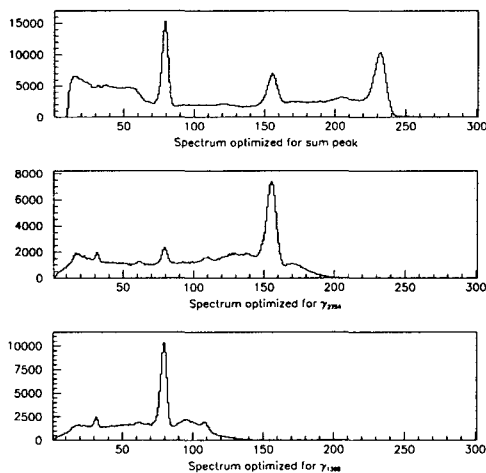


Figure 6.5: Escape peak spectra resulting from optimized gating. Channel number is displayed on the abscissa.

in this experiment. The time during which the NaI detector is exposed to the thermal neutron flux will determine the intrinsic event rate, but in this case an exposure time of approximately 24 hours results in 0.9 events per second detected in the sum peak, 1.3 and 2.3 s^{-1} for 2.754 and 1.368 MeV peaks. The efficiency of the NaI annulus to detect full energy peaks in the range of 1-3 MeV is high, but not 100%, therefore these rates should be considered as lower bounds for the geometry and neutron activation scheme used in this experiment. Also, a neutron source of greater intensity may be better suited to irradiation of a calibration source for SNO.

6.1.4 Additional considerations

I have asserted that the response of SNO to the individual ^{24}Na γ -rays can be determined through coincidence analysis using the activated NaI(Tl) energy spectrum. Simple energy cuts are not sufficient to isolate the response of the γ -rays. The distribution of the ^{24}Na nuclei in the crystal affects the likelihood of γ -ray interactions in the crystal. Both issues are discussed below.

6.1.4.1 Gates

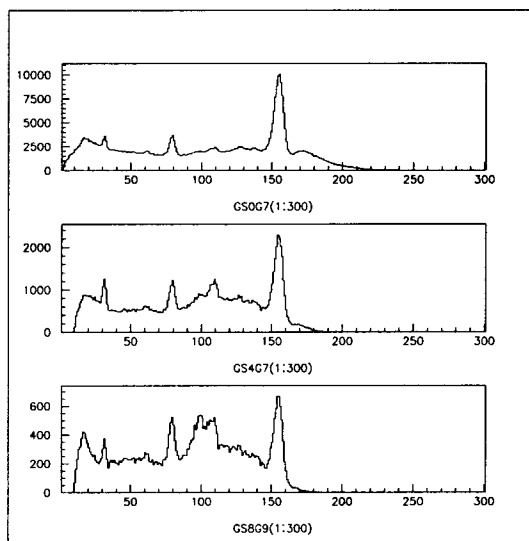


Figure 6.6: Comparison of spectra of NaI Annulus for gates of decreasing width. The designations GS*G# denote vector identifiers for the displayed spectra within PAW. Channel number is displayed on the abscissa.

The selection of gate widths in the activated spectrum has been investigated for the purpose of optimizing the ratio of signal-to-noise for the three ^{24}Na γ -ray peaks. It was assumed that restricting the width of gates would allow for the best signal-to-noise ratio. An investigation of narrow gates on the order of 10 channels in width indicates that there is a lower limit below which the ratio worsens. The reason is as follows: the dominant mode of interaction for a 1-3 MeV γ -ray in a NaI crystal is multiple Compton scattering, therefore, part of the energy of one γ -ray may be deposited in the activated detector, while the remainder of the energy is deposited in the surrounding annulus. The energy may be shared in any ratio. Thus the events which fail to deposit full energy in the annulus are spread over a broad energy region. When one selects a wide gate in the activated detector, one is investigating a large number of Compton events spread across the energy spectrum in the annulus. However, a narrow gate selects a very specific energy range, which in turn selects a

small energy range for Compton scattered events in the annulus. This leads to the appearance of an additional peak in the annulus due to Compton scattered events at a specific energy. This peak can rival the full energy peaks in intensity when narrow gates are selected (Fig. 6.6). Since we wish to isolate the full energy peaks as well as possible, overly narrow gates are best avoided. If there were a means to remove the full energy peaks from the annulus spectrum entirely, we could use narrow gates in the activated detector to provide a tunable calibration source through most of the energy range of the γ -ray.

This result suggests that the most straightforward application of the ^{24}Na source in SNO would use a very small NaI crystal. This would minimize the deposition of γ -ray energy in the crystal and maximize the energy deposition in the D_2O . There should then be a strong signal in SNO associated with the sum peak of the two escape γ -rays, and nothing else. This scenario was simulated and the results are provided below in section 6.2.3. The above results indicate, however, that even when partial energy deposition occurs in the activated NaI detector, very useful signal-to-noise ratios for the single γ -ray lines may be realized. The results of simulations involving larger crystal sizes are also presented below.

6.1.4.2 *Distribution of Activated Nuclei*

The distribution of ^{24}Na nuclei in the NaI(Tl) crystal is important when considering the likelihood for γ -ray attenuation. The linear distance a neutron travels through a material prior to capture is called the diffusion length. The method specified by Segré [124] has been used to estimate the diffusion length, L , in NaI.

$$L = \left(\frac{\lambda\Lambda}{3}\right)^{\frac{1}{2}} \quad (6.1)$$

The mean free path for scattering, λ , and absorption, Λ , are considered in a random walk analysis to derive Eq. 6.1. A value of 5.7 cm is obtained, using scattering and

absorption cross-sections for Na and I from [125] and a value of 3.667 g/cm^3 for the density of NaI crystal [113]. This is on the order of the diameter of the NaI crystal used in this investigation. It is important to use a detector with a crystal of dimension comparable to or less than the thermal neutron diffusion length if the goal is to achieve a uniform distribution of activated nuclei throughout the crystal. Finally, to emphasize the sum peak relative to the individual γ -ray peaks, a crystal with dimensions small compared to the attenuation length of a 1.368 MeV gamma in NaI(Tl) is necessary. The length to attenuate a beam of 1.368 MeV gammas by 50 percent, as given in [114], is approximately 3.3 cm.

6.2 Simulation of SNO Response to ^{24}Na Calibration

The response of SNO to the activated detector has been simulated using SNO-MAN. The size of the NaI(Tl) crystal has been varied to study the response of SNO to differing fluxes of the γ -rays emitted from the decay of ^{24}Na .

6.2.1 Calibration Source

For these simulated experiments the calibration source is composed of a cylindrical NaI crystal and a PMT enclosed within a cylindrical shell of stainless steel. The dimensions of the NaI were varied from $3/4'' \times 3/4''$ to $4'' \times 4''$ to assess the effect of crystal size on the escape spectra of ^{24}Na .

6.2.2 Simulation Scheme

The purpose of the simulation was to study the response of SNO to the ^{24}Na source to determine which of the transitions of ^{24}Na decay may be used as calibration points for SNO. The size of the NaI detector was varied and the Nhit spectrum studied to assess the usefulness of each γ -ray line. Each simulation involved 10^5 ^{24}Na decays. The simulations were conducted with the detector at the center of the D_2O volume.

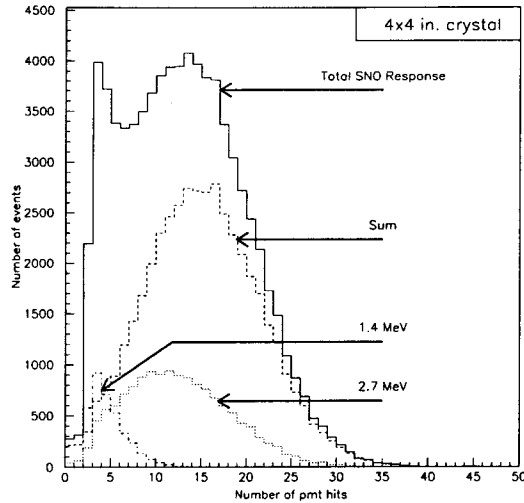


Figure 6.7: Spectra resulting from SNOMAN simulation of $4'' \times 4''$ NaI crystal. Energy cuts have been used to produce the three spectra which appear with dashed lines.

6.2.3 Simulation Results

The response of SNO to γ -rays from the decay of ^{24}Na in a $4'' \times 4''$ NaI detector is shown in Figure 6.7. The response to γ_{1368} is at much lower N_{hit} than the response to γ_{2754} . This is explained by considering that every γ -ray must lose a minimum amount of energy to lead to production of Čerenkov light. Thus, the γ_{1368} loses a larger fraction of energy than does the γ_{2754} , leading to the greater difference in N_{hit} response. Also, as noted earlier in Section 3.2, the production of Čerenkov photons by γ -rays is not a linear process below about 5 MeV. The transfer of energy from γ -ray to e^- is effected through either Compton scattering or e^+e^- production. In the case of Compton scattering, approximately $m_e c^2/2$ is lost. In fact, most Compton scattering will not result in maximum energy transfer. In the case of e^+e^- production, $2m_e c^2$ is required to form the particle pair. In addition to energy transfer losses, there is also the Čerenkov threshold energy to consider. An e^- must have kinetic energy exceeding .261 MeV to produce Čerenkov photons in D_2O .

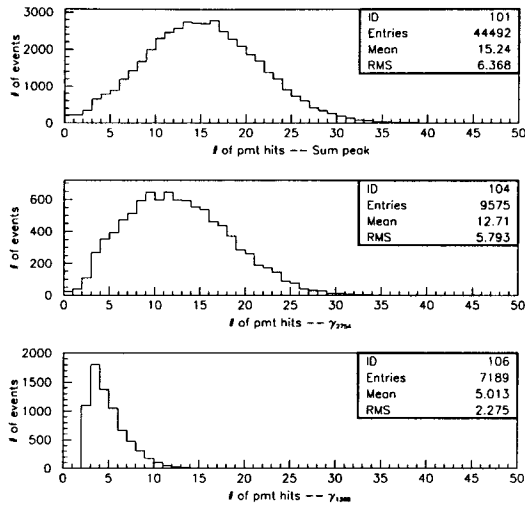


Figure 6.8: Individual spectra resulting from SNOMAN simulation of $4'' \times 4''$ NaI crystal.

Taking these effects together, interactions involving γ_{1368} may only lead to Čerenkov photon production for Compton scattering interactions. At most .902 MeV of e^- kinetic energy will be available for Čerenkov production. The response to the γ_{1368} shows a mean Nhit of 4.5. This provides a ratio of 5.0 Nhit/MeV. In the case of γ_{2754} , both e^+e^- production and Compton scattering processes may lead to Čerenkov photon production, but Compton scattering will be dominant. The response to the γ_{2754} shows a mean of 12.7 Nhit for an available kinetic energy of 2.25 (1.21) MeV for Compton scattering (e^+e^- production). This leads to an Nhit/MeV ratio of 5.6. Both of these ratios may be compared to the ratio for 6.1 MeV γ -ray from ^{16}N , which is 8.9 Nhit/MeV. Finally, the case when both γ_{1368} and γ_{2754} deposit energy in SNO results in a mean Nhit of 15.7. This case clearly must be considered as simply the sum of the responses of SNO to the individual γ -rays, and not as a calibration point representing a single 4.1 MeV γ -ray.

Four sizes of cylindrical NaI crystal were used in the initial simulations, with diameter and height as listed: $4'' \times 4''$, $3'' \times 3''$, $2'' \times 2''$ and $3/4'' \times 3/4''$. The Nhit spectrum

resulting from the simulation of these detectors is provided in Fig. 6.9 for reference. Three line spectra depicting three energy cuts are shown for each simulation. The cuts are made on the spectrum of energy deposited in the NaI crystal. This information is produced by the EGS4 package within SNO. The cuts are similar to those described in Section 6.1.3 and are intended to separate the SNO response to the individual γ -ray and the sum peak.

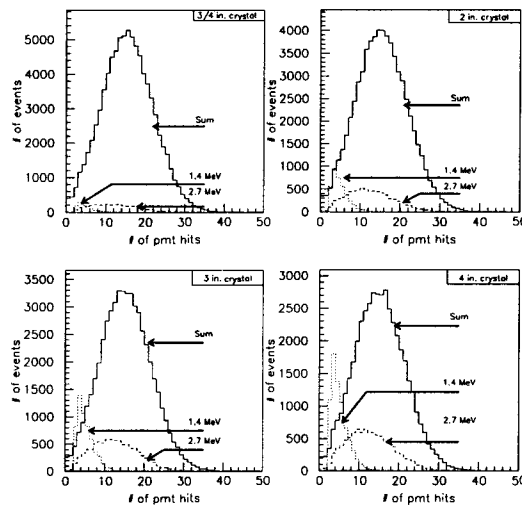


Figure 6.9: Simulated SNO response to four sizes of NaI crystal. The spectra appearing in each plot are the result of energy cuts on the activated NaI spectrum. As crystal size increases, the SNO response to the individual γ -rays grows.

An additional simulation was performed involving a cylindrical NaI detector of dimension $3'' \times 6''$. The volume is near to that of the $4'' \times 4''$ crystal (695 vs. 824 cm^3). Detectors based on crystals of this size have been available as a standard geometry. The gated spectra resulting from this simulation are shown in Fig. 6.10. The spectra are comparable in shape and number of events to those of the $3'' \times 3''$ and $4'' \times 4''$ detectors.

A summary of the simulation results for the sum of γ_{1368} and γ_{2754} is presented in Table 6.2. Data are presented in both the case of a broad energy gate and an optimal

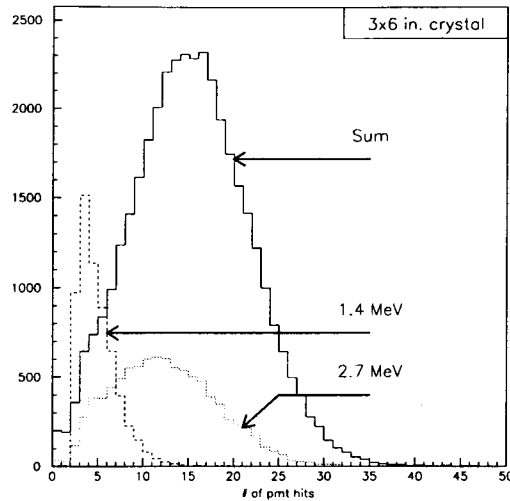


Figure 6.10: Simulated SNO response to 3'' \times 6'' cylindrical NaI crystal.

energy gate in the Activated NaI detector. The mean, an estimate of full width at half maximum and the number of events per 10^5 ^{24}Na decays are provided for each calibration point. Similar data from the γ_{2754} and the γ_{1368} calibration are presented in Table 6.3 and Table 6.4, respectively.

Crystal Size	Broad Gate				Optimal Gate			
	peak	width	number	energy	peak	width	number	energy
3/4''	15.53	16	84528	0.-1.4	15.60	16	77041	0.-1.0
2''	15.39	16	65713	0.-1.4	15.64	15	54960	0.-1.0
3''	15.30	15	53947	0.-1.4	15.61	15	43695	0.-1.0
4''	15.24	16	44492	0.-1.4	15.57	16	35157	0.-1.0
3'' \times 6''	14.91	16	47439	0.-1.4	15.3	16	29965	0.-0.8

Table 6.2: Summary of simulation data for sum of ^{24}Na γ -rays. The mean,FWHM, the number of events per 10^5 ^{24}Na decays and the range of energies (MeV) in the activated NaI energy gate are presented.

Note the low value of the peak for the 3/4'' crystal size and γ_{2754} in Table 6.3. This is because for such a small crystal neither the γ_{1368} nor γ_{2754} is strongly attenuated.

Crystal Size	Broad Gate				Optimal Gate			
	peak	width	number	energy	peak	width	number	energy
3/4"	10.44	13	7896	1.4-2.8	12.21	17	3610	1.4-1.8
2"	10.90	16	17755	1.4-2.8	12.52	15	7512	1.4-1.8
3"	11.21	18	22360	1.4-2.8	12.62	15	8930	1.4-1.8
4"	11.38	18	24783	1.4-2.8	12.52	17	14173	1.4-1.8
3 × 6"	11.32	15	23022	1.4-2.8	12.57	15	9162	1.4-1.8

Table 6.3: Summary of simulation data for ^{24}Na γ_{2754} . The mean, FWHM, the number of events per 10^5 ^{24}Na decays and the range of energies (MeV) in the activated NaI energy gate are presented.

The signal reflects a trigger on Compton scattered γ_{2754} within the crystal. The Nhit response is then to the scattered γ -ray and the γ_{1368} that was emitted in coincidence. A hard cut on the NaI energy spectrum is necessary to produce a clean signal, leading to a small number of useful events (7500 events from 10^5 decays).

The shape of the Nhit spectrum for the γ_{1368} is insensitive to the width of the energy gate placed on the activated NaI energy spectrum. The energy gate from 2.8-4.1 MeV produces the same shape as that for any narrower gate within this range. This is true independent of the size of the crystal. The number of γ_{1368} events is then directly determined by the crystal size. A small crystal minimizes the number of γ_{1368} events, while a large crystal maximizes these events.

Crystal Size	Optimal Gate			
	peak	width	number	energy
3/4"	4.84	4	1086	2.8-4.1
2"	4.96	4	3711	2.8-4.1
3"	5.05	4	5668	2.8-4.1
4"	5.01	4	7189	2.8-4.1
3 × 6"	4.98	4	6122	2.8-4.1

Table 6.4: Summary of simulation data for ^{24}Na γ_{1368} . The mean, FWHM and the number of events per 10^5 ^{24}Na decays are presented. The energy range of the gate in the activated NaI detector is 2.8-4.1 MeV.

The preceding discussion is helpful in considering the utility of ^{24}Na as a source of multiple calibration points for SNO. In the assessment of ^{24}Na described in Section 6.1.3 ratios of peaks to background were assessed (Fig. 6.5). It was asserted that the ratios obtained were lower limits. Similar spectra are presented in Fig. 6.8. As seen in these results of the Monte Carlo, SNO clearly distinguishes between the three peaks. With appropriate selection of energy gates in the activated NaI spectrum, the SNO response to these three γ -ray escape energy peaks may be separately obtained.

6.3 Assessment

The feasibility of calibrating SNO for energies below 5 MeV through use of a neutron activated NaI detector has been investigated and quantified. Such a source can be prepared above ground and can be sealed to avoid contamination to the SNO D_2O . Expected counting rates have been provided, but these may be adjusted through the level of activation achieved in, as well as the size of, the NaI detector. Activation of the detector with thermal neutrons should be performed to provide a spectrum free of untagged gamma rays. Arrangements have been made to make use of high intensity beams of thermal neutrons available at Chalk River Laboratories, Ontario, Canada. A count rate of 1,000 Hz may be easily obtained with this source.

SNO responds well to the case when both ^{24}Na γ -ray emerge from the calibration source, regardless of the size of the detector. A peak appears at 15 Nhit. This peak is enhanced by using the smaller NaI size, but remains a main feature in the Nhit spectrum for each crystal size in the study. The larger crystal provides more attenuation of the γ -rays and leads to an enhancement of the signal for the individual γ -rays.

What was not apparent from the previous work [122] is how close together the Nhit peaks for the sum and γ_{2754} spectra would be. Recognizing that SNO is not sensitive to the sum of the γ -ray energy, but rather the sum of the Čerenkov light

produced separately by γ_{1368} and γ_{2754} , leads to the conclusion that the NaI detector ought to be made large enough to attenuate the γ -rays such that reasonable detection rates for the single γ -rays may be obtained. The sum peak may still be assessed in the context of a higher energy γ -ray that undergoes multiple scattering and leads to deposition of approximately 3 MeV of e^- kinetic energy in SNO, but the single γ -ray spectra from the individual γ -rays will be of significant value for specifying the response of SNO to low energy neutrino events.

6.4 The ^{24}Na Source

The activated NaI(Tl) source design needs to accommodate four criteria:

1. Avoid introducing radioactive backgrounds into the D_2O .
2. Avoid altering the optical properties of the D_2O .
3. Be deployed through calibration guide tubes into the region between the AV and PSUP.
4. Produce calibration event rates sufficient to obtain good statistics for all three γ -ray escape conditions within the source's useful lifetime.

The results of the ^{24}Na investigations were applied to these criteria. The selection of source components is described in the following sections. A diagram is shown in Figure 6.11.

6.4.1 NaI(Tl) Detector

A 3×3 in. right cylindrical NaI(Tl) detector was selected. The dimensional restrictions imposed by the calibration guide tubes were a significant factor. Additionally, the Monte Carlo simulation showed that the larger 4×4 in. crystal would not appreciably enhance the individual γ -ray rates compared with the 3×3 in. crystal. A

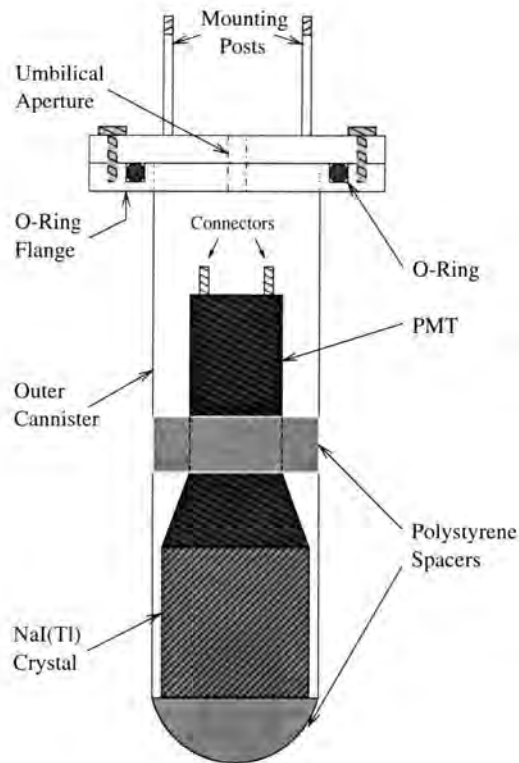


Figure 6.11: Schematic drawing for the NaI(Tl) source D₂O cannister.

BICRON monoline detector, model 3M3/3, was selected. It features an airtight casing to protect the hygroscopic NaI crystal from moisture and mounts the PMT to the crystal as an integral unit. The operating voltage is +1000 volts.

6.4.2 D₂O Container

The D₂O container is to isolate the NaI(Tl) detector from contact with the D₂O. The primary concern is to avoid introducing radioactive contamination inside the acrylic vessel. The container must be reliable and easy to use repeatedly over the life of the experiment.

A thin-walled, stainless steel jacket has been fabricated. It has two major components: a pseudo-hemispherical cap welded to a right circular cylinder and an o-ring flange. The cylinder and cap contain the NaI(Tl) detector. The wall is 1/16 in. thick

to minimize γ -ray attenuation. The o-ring flange is welded to the end of the cylinder and is sealed with bolts. The o-ring is in simple compression, providing a reliable water seal. The cannister was hydrostatically pressure tested to 120 psi, approximately 3 times the maximum pressure in the acrylic vessel.

6.5 *Source Preparation*

The preparation involves four major tasks. The NaI(Tl) detector must be activated, transported to Sudbury, checked for surface radioactive contamination and transported to the underground laboratory. Data will be obtained at various points within the D₂O volume with both small and large NaI(Tl) crystals.

The NaI(Tl) detector will be activated at the Steacie Institute for Materials Science at Chalk River. This facility provides a well-regulated thermal neutron beam and a rotating table to provide for uniform irradiation of the detector. The neutron flux is high ($\sim 10^8 \text{ cm}^{-2}\text{s}^{-1}$), but more importantly, it is reproducible. The exposure time can be adjusted to achieve a desired activation level within 10 % uncertainty based on a sample irradiation performed in December 1998.

The detector will be handled only with latex gloves to avoid placing salt and oils on the surface prior to irradiation. Additionally, it will be double-bagged in plastic to avoid surface contamination while inside the reactor building. The detector will be activated one day prior to shipment. The ¹²⁸I activity will diminish to a negligible level overnight. Depending on the ²⁴Na activation level, the detector may be classified as a radioactive source, or it may be considered to be below the threshold for such classification. In either event, procedures at Chalk River allow for a SNO scientist to courier the activated detector to Sudbury.

The detector will be unbagged at Laurentian University in Sudbury, and the surface tested for contamination. The surface will be cleaned with Alconox, rinsed with ethanol followed by distilled water, and double-bagged again for transport under-

ground. Testing above ground will not be completely conclusive, because radioactive backgrounds above ground would mask small levels of activity disruptive to SNO operations and calibrations. It does serve to identify gross contaminations, which can be assessed prior to delivery to the underground laboratory.

Installation of the NaI(Tl) calibration source requires insertion into the stainless steel cannister. Connections to a signal cable and a cable to provide high voltage will be made prior to sealing the cannister. Deployment within SNO will proceed as described for the ^{16}N source, using the calibration manipulator control computer.

6.6 Calibration Procedure

The procedure for calibration will be similar to that described for the ^{16}N source. A grid of calibration points will be followed. The variation of SNO response to the ^{24}Na source is expected to be smaller than that for the ^{16}N source. Initial calibration measurements will likely be made on a coarse grid. A finer grid, similar to that for ^{16}N , will be sampled when the detector operation is regarded as stable.

The small and large NaI(Tl) crystals will be used to measure different ^{24}Na signals. The small crystal is suited to the γ -ray sum response, as γ -ray attenuation will be very low. An activation to 1,200 ^{24}Na decays per second 48 hours following irradiation provides a count rate to achieve statistical uncertainties of 1% per point per 8 directions on an 82 point grid in 26 hours. Sufficient activity would remain in the source (400 decays per second) to repeat the measurements (test systematics dependent on source rate), or to perform calibrations between the AV and PSUP to study background signals. The source rate will remain above 10 decays per second 152 hours post irradiation, or 104 hours post initiation of this sample calibration scheme.

The large crystal is used to determine the individual γ -ray response. The ^{24}Na source signal will be passed through a fast discriminator to set a threshold which

excludes the sum events. In this way, the single γ -ray signals may be enhanced without overwhelming the data stream with sum events. The sum events will contribute to the calibration background, but that spectrum will be measured by triggering the detector at a fixed interval and therefore the analysis will not be compromised.

7. SNO Detector Commissioning

Initial detector operation was conducted while the detector was dry, during a period referred to as “Air Fill”. Commissioning activities included initial electronics calibrations to establish time and charge coefficients, relative timing, and the single photoelectron response for each channel, acrylic vessel optical attenuation and cavity background measurements. The results of the latter topic were expected to reflect the radon level in the air; radioactivity in the acrylic vessel, PSUP and the PMTs; radioactivity from the cavity walls; and, high energy muons. Simulation of Nhit spectra for these event classes had predicted a monotonically decreasing event rate as a function of increasing energy, with only a very few events exceeding 50 Nhit, and those due only to high energy muons.

Of course, the entire point of building SNO is to fill it with water and study the solar neutrino signal. A brief account of the early operation of the filled detector and a preliminary assessment of the Nhit, PGT and ^{16}N Nhit spectra is provided in the final sections of this chapter.

7.1 Air Fill

Commissioning data were obtained using three trigger classes:

- Nhit trigger, when the detector records the events exceeding an Nhit threshold,
- ESUM trigger, events exceeding a global charge sum threshold, and,
- Pulsed Global Trigger (PGT), events resulting from triggering the detector at a fixed rate.

A sample of the Nhit spectrum resulting from each of these three trigger types is shown in Figure 7.1. The PGT rate was 5 Hz, the threshold for Nhit was 30, and the threshold for ESUM was -175 mV, corresponding to about 17 photoelectrons. The

data spans 53 minutes of elapsed time. The Nhit trigger spectrum is displayed in the upper panel, and events exceed the threshold 75 times per second. The three spectra are compared in the lower panel. The ESUM trigger events occur approximately once per second, covering the range from zero to 600 Nhit, although this figure stops at 200 Nhit to better show the features of the three spectra.

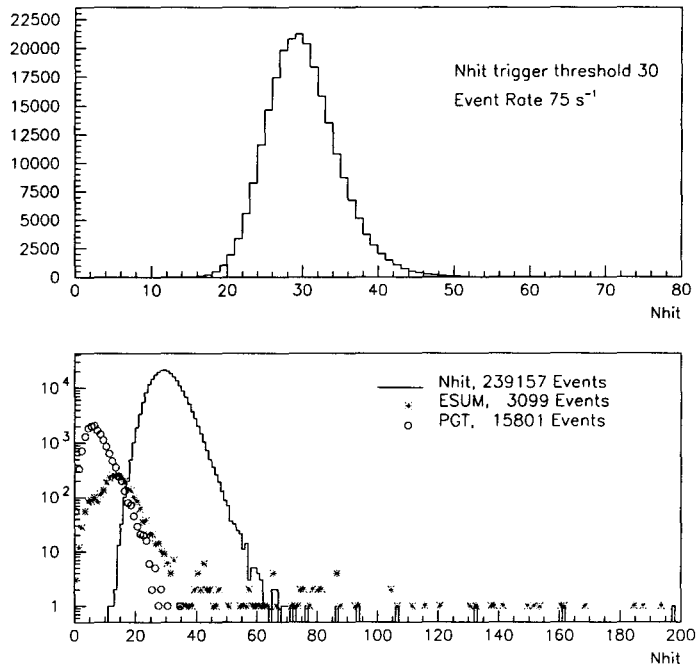


Figure 7.1: Nhit spectra resulting from Nhit, ESUM and PGT triggers. Data from the Nhit trigger appear in the top panel, while data from all three triggers appear in the bottom panel in a logarithmic scale.

There are many more events than expected above the background threshold endpoint value (near 70 Nhit in Fig. 7.1). Muon events only should create Nhit above the threshold in an air-filled detector. Either our understanding of the muon flux at the SNO site was woefully wrong, or an unknown process was responsible for these events. Additionally, the background threshold endpoint occurs at significantly higher value than predicted. This result brings into question our understanding of

the processes causing the majority of background events, or our ability to predict the light generation and transport in the detector.

7.2 *Anomalous PMT Performance*

The events with large numbers of N_{hit} were quickly attributed to anomalous PMT behavior. There are two reasons for this conclusion:

- Muons may create appreciable Čerenkov light only by interacting in the acrylic vessel. Muons will move through the acrylic in straight lines due to their very high (GeV) energies. There is very little acrylic available along any straight line track through the detector, therefore Čerenkov light production from muons is generally limited to a few hundred N_{hit} , and,
- Most high N_{hit} events featured a particular time signature. The earliest PMT shows a very high charge, sufficient to cause both the low and high ESUM triggers to fire. Additionally, as shown in Figure 7.2, there is a peak 70 ns following the “hot” PMT, which equals the time required for light to cross the PSUP diameter (~ 50 ns) plus 20 ns. This peak is consistent with a PMT cluster on the opposite side of the detector from the “hot” PMT.

The evidence from the time spectra led to the supposition that light was being emitted from PMTs and observed in the detector. These events were therefore named “flashers”. It was necessary to perform an analysis to verify the flasher hypothesis. The analysis would then be applied to identification of these anomalous events to remove them from consideration as neutrino events.

7.2.1 Flasher Analysis

A geometric analysis was performed to confirm that flashers emitted light. The criteria for identification were based on the relative location of PMTs in the peaks

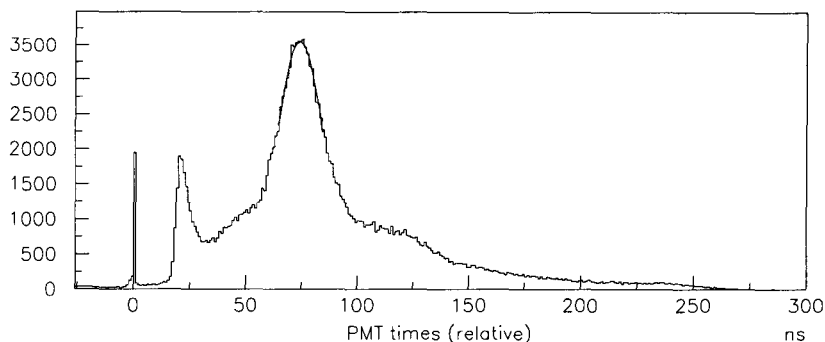


Figure 7.2: Anomalous event timing. The timing is relative to the PMT with maximum charge in the event.

from the relative timing study. Light emitted from a PMT will reflect from the acrylic vessel and be recorded in nearby PMTs. Light will also be transmitted across the detector. The straight line paths for reflected and direct light are 5 and 17 meters, respectively. The travel times are 16 and 56 ns.

The peak widths suggest that flasher light emission occurs over an extended period. The peaks are broad, about 10-20 ns in width. For comparison, this is larger than the light emission times for the laser ball and LED optical calibration sources by a factor of 5-10.

Analysis to confirm the light emission hypothesis considered relative PMT positions, and is illustrated in Figure 7.3. The PMT charge was searched within an event to identify candidate flashers. Thresholds for charge values indicating extremely large numbers of photoelectrons (>20) were used to identify candidate flashing PMTs. The time and position of all other PMTs in the event were calculated relative to the candidate PMT. The position is represented as $\cos\theta$, where θ is the polar angle between the candidate and other PMTs in the event, defined with respect to the center of the AV. The distribution of PMT time relative to the candidate flasher vs. polar

Flasher ID Technique

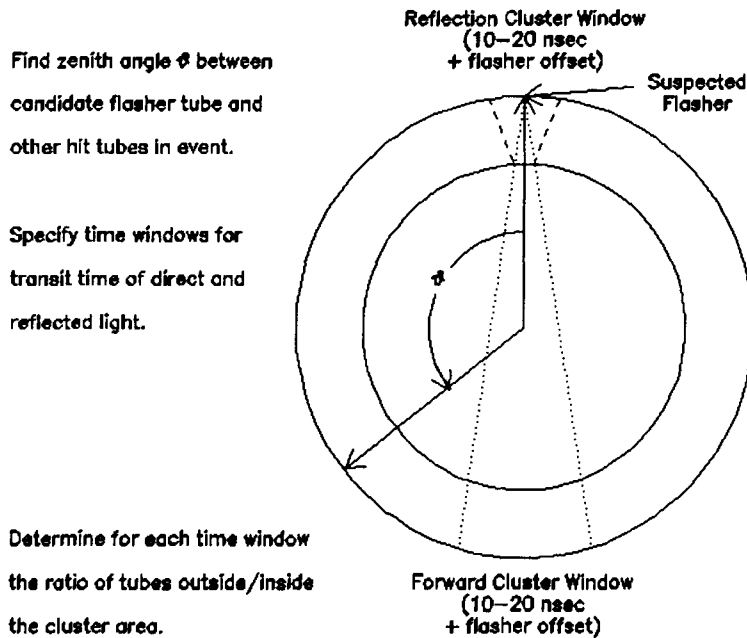


Figure 7.3: Geometric time and position method to identify flasher events.

angle distribution reveals PMT clusters for both light reflected from the AV near the flasher ($\cos\theta \sim 1$) and for light transmitted through the AV to the opposing PMTs ($\cos\theta \sim -1$). The good agreement between the relative positions and times supports the light emission hypothesis.

A quantitative measure describing how well a candidate flasher event satisfies the geometric criteria is presented in Eq. 7.1:

$$S_{cl} = \frac{N_o}{N_i} \times \frac{d\theta}{d\Omega}. \quad (7.1)$$

Comparing the PMT hits within selected geometric areas, N_i , to PMT hits outside those geometric areas, N_o , during the same time window allows a quantitative measure of the cluster strength, S_{cl} . The ratio is applied separately to the reflected and the direct light time windows. The scale factor $d\theta/d\Omega$ accounts for the disparate surface area inside and outside the selected region. High strength is reported as ratio values

tending to zero, while values near unity indicate an even distribution of PMT hits throughout the detector during the time interval of interest. The relative times and angles for a typical flasher event are presented in Figure 7.4.

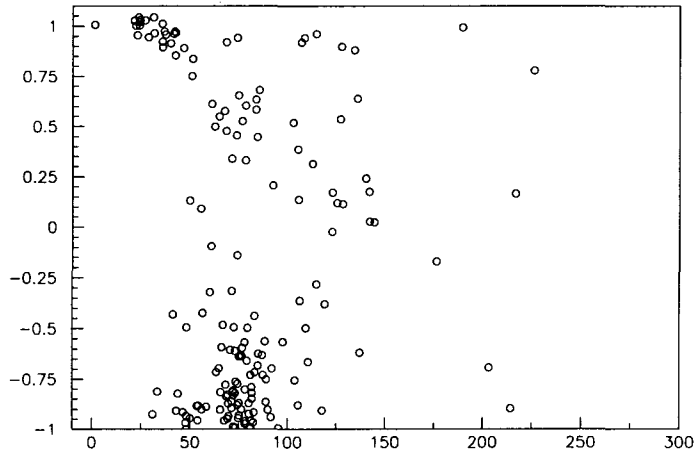


Figure 7.4: Flasher relative time and angle relations. The PMT cluster at 75 ns and $\cos \theta = -1$ represents light emitted from the high-charge PMT that traverses the detector. The cluster between 25 and 50 ns and near $\cos \theta = 1$ is light reflecting from the acrylic vessel. Angles are measured with respect to the center of the detector. $\cos \theta = 1$ represents the high-charge PMT.

7.2.2 Multiple Flasher Candidates

Flashing PMTs have not been reported in the literature. There have been private communications between SNO collaborators and scientists conducting other experiments which have revealed that flashers are common when operating a PMT to observe single photoelectrons. Experience is therefore limited in characterizing flasher pathology. Flasher events occasionally feature more than one candidate PMT. In this case, the cluster strength may be assessed to decide between candidate flashers.

The geometric analysis to identify flasher candidates was applied to Run 567 from May 1998. Recall that there are three ADCs that determine the charge from each PMT: high-gain long-integration time (pmthl), high-gain short-integration time

(pmt_hs) and low-gain long-integration time (pmt_lx). The multiple candidates arise when the high charge test identifies more than one PMT, typically with high values in different ADCs. A total of 4565 candidate flashers were considered. The geometric technique identified the appropriate candidate for 92% of the events by applying the ratio 0.1 as a threshold. While 100% efficiency is desired, better than 90% efficiency greatly reduces the workload for scanning events manually.

7.2.3 Blind Flashers

The geometric technique has been shown to clearly identify flasher events with high accuracy. Unfortunately, the anomalous PMT behavior also exhibits a perverse manifestation: flashers which do not emit light. Strictly speaking, this is not true. If a flasher flashes, it emits light. The difficulty occurs when the time structure of events in the detector leads to the occurrence of a flasher near the end of a previous trigger window. The flasher is then out of time with PMTs that see the light from it. These events were dubbed “Blind Flashers”. The geometric technique described above fails for this class of events. These events therefore look similar to a Čerenkov cone and can be difficult to distinguish from solar neutrino events.

The technique employed to identify blind flashers is familiar from our consideration of ^{17}N β -decay events. A delayed coincidence is sought, but in this case the time scale of the delay is very short, and dictated by the transit time in the detector, which is about 50 ns. This characteristic delayed coincidence sticks out like a sore thumb, and neatly addresses the problem of blind flashers.

There do occur some events where the flashing PMT actually fails to generate any signal at all, or the signal fails to be registered. In this case, the analysis must rely on establishing a good Čerenkov ring, and judging whether the number of Nhits in the event is appropriate for consideration as a solar neutrino event.

7.3 Backgrounds

The resolution for the background threshold endpoint discrepancy was not obvious. Initial thinking was shaped by Monte Carlo predictions for the amount of light which could be produced by γ -rays in the acrylic vessel. Predictions indicated such γ -rays would not produce sufficient light to match the endpoint, therefore the rates of the background processes were investigated. Calculations and simulations were performed to investigate the pileup of radon decay events. Pileup refers to the case when two separate events occur within the resolving time of the detector. The individual signals are then summed together rather than being recorded as distinct events. There were questions as to the amount of light produced by α particles causing the air to scintillate. There were concerns about pileup from radiative backgrounds in the AV, PSUP and PMTs. The fact that the endpoint problem was underdetermined was finally confronted and the decision to perform a limited energy calibration using ^{16}N was reached.

7.4 Energy Scale

Energy calibration was not initially considered a high priority for air fill because only the acrylic vessel provided a medium in which Čerenkov light would be produced. Additionally, there would be a poor tagging efficiency because only about 10% of γ -rays would interact in the acrylic. Many ^{16}N calibration events would trigger the detector at arbitrary times relative to Nhit and ESUM triggers. Obtaining an accurate calibration was considered unlikely and unnecessary. The finding of background events which were not readily attributed to known physics processes changed our thinking regarding the utility of running a γ -ray source in the empty detector. Calibration activity would be conducted to obtain data from a known event class with which to compare the Nhit background data.

The acrylic vessel is not well suited to provide for γ -ray interactions to produce Čerenkov light. The wall thickness is small compared to the attenuation length for γ -rays in acrylic, therefore few γ -rays will interact. Additionally, those e^- resulting from the γ -ray interactions may exit the acrylic. The lost energy makes the event useless for energy calibration, however, useful information may still be extracted. Determination of the energy scale for γ -ray interactions is completely insensitive to the limitations imposed by acrylic vessel optical and geometric properties. The goal was to see what signal is produced by 6.1 MeV γ -rays. A flat spectrum with a high-energy tail was observed, allowing the upper limit to the Nhit spectrum from the ^{16}N source to be established. This result provides a reference against which to judge the signal from γ -rays in the SNO cavity.

7.4.1 Calibration Measurement using ^{16}N in Air

The ^{16}N source chamber was operated at five positions within the acrylic vessel: +600, +250, 0, -250 and -500 cm on the vertical axis. Data was obtained for one hour at the central position and 20 minutes at the other four positions. The ^{16}N source signal was used to generate an external asynchronous trigger (EXTASY). The pulsed global trigger (PGT) was set to 100 Hz, similar to the ~ 300 decay per second ^{16}N trigger rate. The Nhit and ESUM triggers were disabled.

The Nhit distributions for the two trigger classes are displayed in Figure 7.5. The EXTASY spectrum closely resembles the PGT spectrum at low Nhit. The EXTASY endpoint extends to 65-70 Nhit, in very good agreement with the background endpoint from the Nhit spectra. This result points to the cavity γ -rays as the likely source of events comprising the endpoint region. This possibility had previously been dismissed because simulation had predicted 50% fewer Nhit than were observed.

The ^{16}N Nhit spectrum is obtained by scaling the PGT to match the EXTASY spectrum at the low Nhit peak. The scaled PGT spectrum is then subtracted from

the EXTASY spectrum, and is labeled in Figure 7.5 as EXTASY - PGT. The resulting ^{16}N Nhit spectrum is flat with a high-energy slope. The point at which the spectrum rolls off is noteworthy, as well as the shape of the slope and the end point. Note that the subtraction had little effect on the high-energy slope.

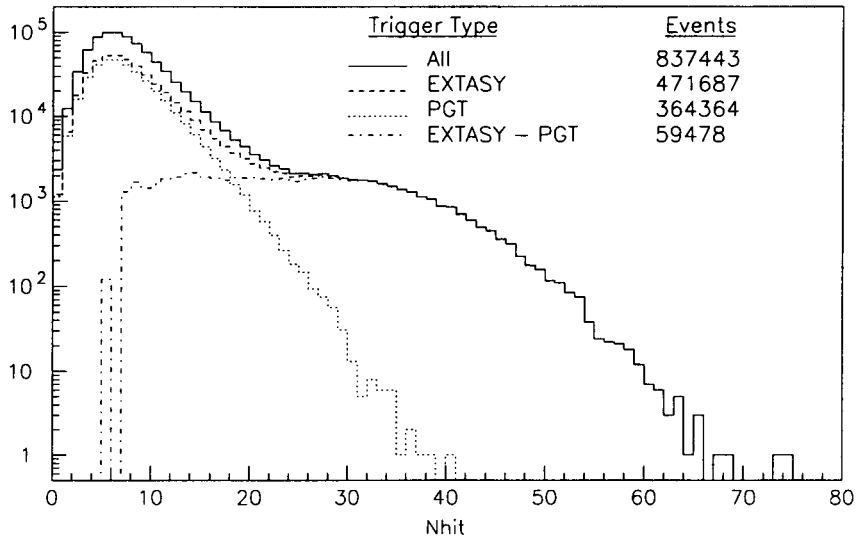


Figure 7.5: Air fill ^{16}N calibration spectra. External asynchronous trigger is depicted by the solid line, while pulsed global trigger spectrum is shown as a dashed line.

7.4.2 γ -rays in the SNO Cavity

Gamma-rays arise from two mechanisms in the rock surrounding the SNO cavity. They are emitted directly when nuclei undergo radioactive decay and they arise from thermal neutron capture. The former case produces mostly γ -rays below 4 MeV, while almost all higher energy γ -rays result from the latter. The rate of γ -rays as a function of energy had been measured in the SNO cavity, as reported in Section 3.3.2.1. A simulated γ -ray spectrum based on this measurement is shown in Figure 7.6. It has been scaled by the factor 1.5 determined necessary to bring the ^{16}N simulated Nhit

spectrum into agreement with the observations. The cavity γ -ray simulation shares the same end point as that from ^{16}N .

This result indicates that light production from the AV is independent of γ -ray energy above 6 MeV. Additionally, this result indicates that the influence of γ -rays in the cavity on the Nhit spectrum is limited to the area below the high-energy tail with end point approximately 70 Nhit.

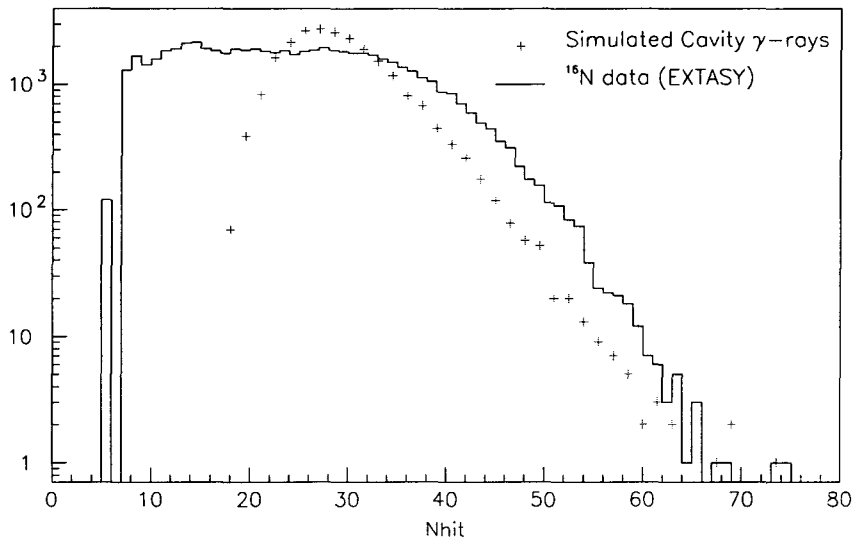


Figure 7.6: Simulated Nhit spectrum due to cavity γ -rays.

7.5 Water Fill

The detector water fill was completed at the end of April, 1999. Water fill commissioning drew from the experience gathered during the air fill commissioning period and focused primarily on the verification and calibration of the electronics and data acquisition. These activities include identification and replacement of faulty components, debugging software and initial studies of detector backgrounds. The commissioning period is expected to last six months.

The detector Nhit spectrum was studied with the ^{16}N β -decay source, using a variety of trigger classes and conditions. The data presented in this section is very preliminary. The observatory was operating with preliminary electronics and optical calibrations. Modifications to electronics hardware were frequent, requiring the high voltage supplies to be lowered and raised on a small segment of the PMTs daily. The data obtained with the ^{16}N source and described here is not optimized and is not intended to represent a final statement concerning SNO energy calibration. It is intended to provide evidence that the ^{16}N source works as described in the preceding chapters.

7.5.1 PGT Spectrum

During the air fill period, the Pulsed Global Trigger spectrum represented a large amount of light per random sampled event compared to triggered events. That was because the PGT spectrum was sampling from events reflecting the Čerenkov interactions in the empty detector. The PGT spectrum during water fill will again be sensitive to the random distribution of light in the detector, but the Čerenkov interactions due to cavity γ -rays is greatly reduced by the H_2O shielding. The expectation is that the PGT spectrum will mainly sample from the random coincidences due to PMT noise, generating an Nhit spectrum well described by a Poisson probability distribution.

The PGT spectrum as sampled during May 1999 appears in Figure 7.7. The peak is at 2Nhit, and the data is compared to a Poisson distribution. The reduced- χ^2 is minimized for a distribution describing the probability that two events are observed ($\chi^2=51.6$), but the fit is poor. The PGT spectrum is therefore not well described by a Poisson distribution only. Another process seems to be enhancing the events in the range 1-3 Nhit, so that the assumption that PGT samples mainly from random PMT coincidences is not justified by this data.

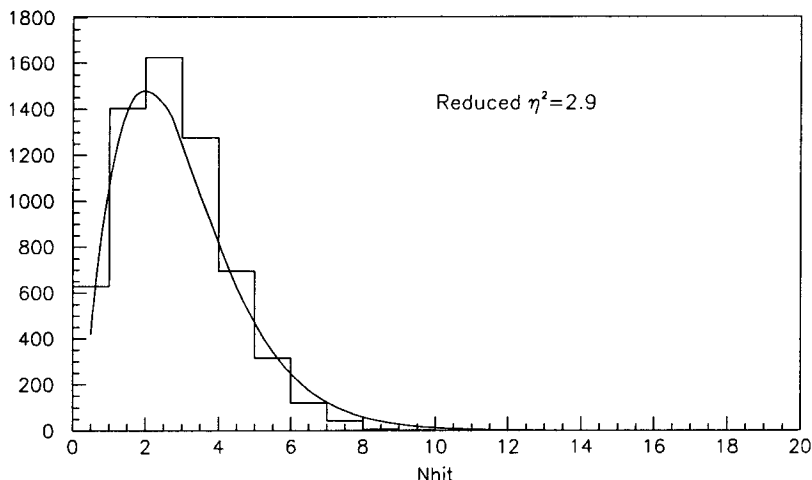


Figure 7.7: The Nhit spectrum from the Pulsed Global Trigger (PGT). The trigger rate is 5 Hz and no other triggers are associated with these events. The fit to a Poisson distribution for 2 events is included.

7.5.2 Preliminary ^{16}N Energy Calibration

A preliminary energy calibration was performed using the ^{16}N source during late May 1999. Two hours of data, representing about 2.1×10^6 ^{16}N decays in the source chamber, was accumulated with the source positioned at the center of the AV. Additional data was obtained for the source chamber positioned on the AV vertical axis, at 1, 2, 3, 4, 5 and 6 m above the center for about 1 hour each. The data for the source at the center of the AV, Run 3606, is analyzed for the Nhit spectrum centroid and standard deviation, and compared with Monte Carlo.

The trigger conditions must be considered when evaluating the Nhit spectrum. The following triggers were used during Run 3606: Nhit100 High, EXT synchronous and PGT. The Nhit100 High trigger monitors the number of PMTs that have generated a signal during a moving 100 ns trigger window. The threshold was set at 30 during this run. The EXT synchronous trigger takes the ^{16}N source chamber PMT signal and directly triggers SNO when the Global Trigger 500 MHz clock next incre-

ments (every 20 ns). This trigger is therefore susceptible to a 20 ns jitter: the trigger may occur exactly in time with the clock, or it may come just after a clock increment, and the trigger is not issued until 20 ns later. The window to readout the event is 400 ns in duration. The data will now be considered by trigger class.

A major objective for the ^{16}N source is to trigger SNO in-time with the ^{16}N β -decay. The umbilical line that delivers ^{16}N to the source chamber is itself a source of ^{16}N β -decay. Triggering on those ^{16}N decays occurring in the source chamber should provide a data set that does not contain decays from the umbilical.

The general SNOMAN time fitter is used to determine the Čerenkov vertex position for all events. The EXT trigger events are considered separately. The resulting fit positions are shown in Figure 7.8. All data in the top panel, EXT triggered data in the bottom. The triggering technique is successful.

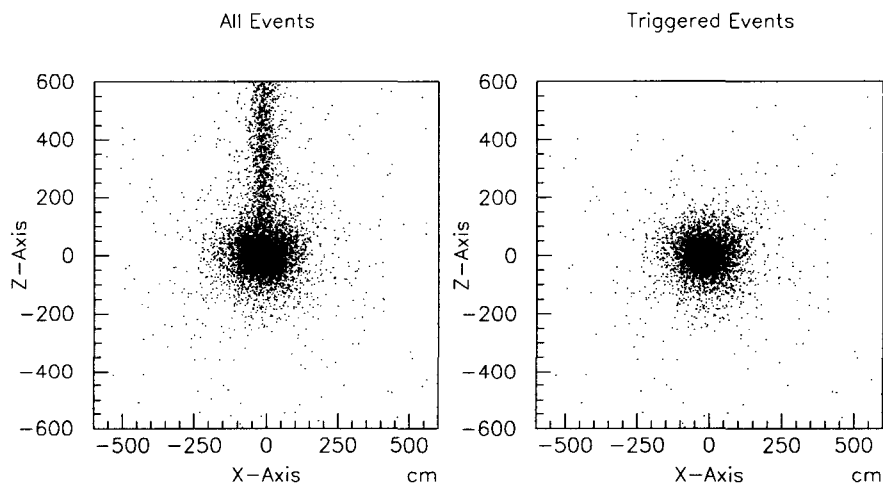


Figure 7.8: The effectiveness of the ^{16}N triggered source is demonstrated. Čerenkov light production vertices are reconstructed from the data. Left: All events - the umbilical is clearly imaged. Right: Triggered events - only source chamber decays are imaged.

7.5.3 Comparison with Monte Carlo

The requirement for an accurate particle transport Monte Carlo simulation of the SNO detector has been made previously in this work by the author. The N_{hit} distribution obtained with the source chamber is compared to that predicted by SNO-MAN and presented in Figure 7.9. Two features deserve comment: The centroid and width of each distribution. The centroid is found by fitting the central 25 channels to a Gaussian distribution. The difference between the centroid values is 20%. The statistical uncertainty in this parameter is less than 1%, therefore this is a large disagreement. The full width at half maximum (FWHM) is consistent between the distributions, suggesting that a systematic shift of the spectrum is being observed, rather than a process that only affects some of the events. The latter type of process would broaden the data distribution compared to the Monte Carlo.

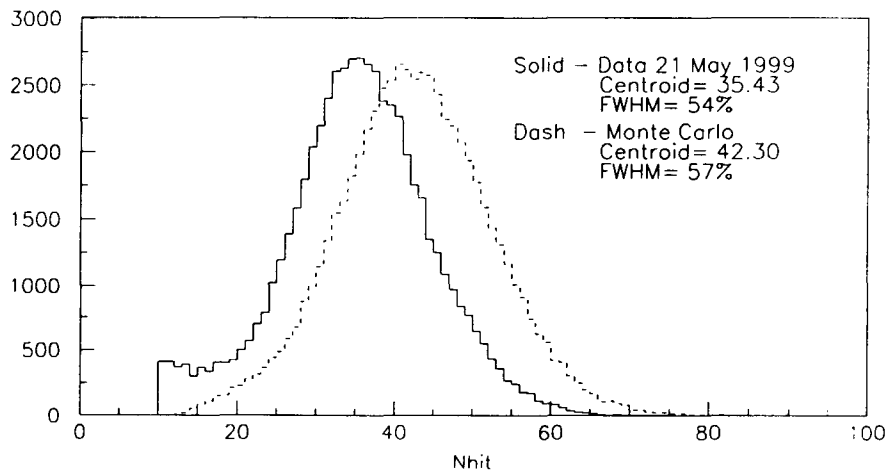


Figure 7.9: The N_{hit} spectra from May 1999 is compared to the results of Monte Carlo simulation.

Processes that would systematically shift the N_{hit} distribution would involve optical photon generation and/or transport. Additionally, the PMT efficiency must be

determined and compared with the value of 29% used in the Monte Carlo. Finally, the PMT thresholds may induce a systematic shift. All of these considerations emphasize the disclaimer presented at the beginning of this section: This data is preliminary and only serves to demonstrate that the triggered source works. Meaningful energy calibration will be possible only after more extensive electronic and optical calibrations have been obtained.

7.6 Summary

The initial commissioning period for the SNO detector was used to investigate the performance of many detector subsystems. The electronics and optical calibrations were directly useful even in the empty detector. The ^{16}N β -decay calibration source proved useful despite the severe limitation posed by an empty detector. The energy scale of the empty detector was determined. The observed backgrounds were accounted for by the rate of γ -rays emitted from the cavity walls.

The ^{16}N β -decay source was used to perform preliminary energy calibration. The work revealed that the timing of the source relative to the PMT array needs to be improved. However, data obtained from the untriggered source allows a useful preliminary determination of the Nhit spectrum due to ^{16}N γ -rays.

8. Conclusions

Neutrinos are a subject of intense scrutiny by researchers involved in cosmology, high-energy physics, stellar physics and nuclear physics. Their importance is tied to the possibility that the neutrino rest mass is non-zero. The desire for concordance between experimental observations in the above mentioned disciplines and fundamental theoretical descriptions of neutrinos that extend the standard model of electroweak interactions has led to the construction of the Sudbury Neutrino Observatory. The neutral-current interactions between solar neutrinos and deuterium make possible a definitive measurement of the total ^8B solar neutrino flux that is independent of neutrino flavor.

The interpretation of the total ^8B flux is enhanced by a properly normalized comparison with charged-current data also obtained from SNO. The charged-current data will be studied to determine the energy spectrum of the ^8B ν_e . An accurate energy calibration is crucial to obtain not only the total charged-current flux, but also to assess the energy spectrum shape against that observed for e^- emitted during ^8B β -decay in the laboratory. The spectral shape will be analysed for deviations from the laboratory shape that may provide evidence for particular neutrino oscillation mechanisms. These results will be interpreted to attain mass differences between the neutrino flavor eigenstates.

The Sudbury Neutrino Observatory has operated in a commissioning phase since early March, 1998. The ^{16}N β -decay energy calibration source has been used in an empty detector to provide an energy scale and allow attribution of background events to specific classes. The source has recently been used to make preliminary energy calibration in the filled detector. The demonstration that this primary energy calibration source works reliably has been heartening to the entire collaboration. The iterative process of full detector calibration, featuring electronics; optical transport and PMT efficiency; energy calibration; and, Monte Carlo verification is underway.

The calibration process will expand to include additional energy calibration sources, including the low-energy ^{24}Na source. Not only will this source provide energy calibration at 2.7- and 1.4-MeV γ -ray energy, but the rate of photodissociation of deuterium by the 2.7-MeV γ -rays will be used to accurately determine the neutron detection efficiency that is so important to the neutral-current measurement. The successful performance of the ^{16}N source and the associated detector operations and analysis efforts bode well for the long-term successful operation of this neutrino observatory.

Bibliography

- [1] W. Pauli, in *Rapp. Septieme Conseil Phys.*, Solvay, Brussels (Gautier-Villars, Paris, 1934), 1933. English translation contained in: L.M. Brown, *Physics Today*, **31**, 9, (1978).
- [2] E. Fermi, *Ricercha Scient.*, **2**, 12 (1933).
- [3] F. Perrin, *Comptes rendues*, **197**, 1624 (1933).
- [4] E. Fermi, *Z. Physik*, **88**, 161,(1934).
- [5] G. Gamow and E. Teller, *Phys. Rev.*, **49**, 895, (1936).
- [6] T.D. Lee and C.N. Yang, *Phys. Rev.*, **104**, 254, (1956).
- [7] C.S. Wu, E. Ambler, R.W. Hayward, D.D. Hopps and R.P. Hudson, *Phys. Rev.* **105**, 1413 (1957).
- [8] R.L. Garwin, L.M. Lederman and M. Weinrich, *Phys. Rev.* **105**, 1415 (1957).
- [9] J.L. Freidman and V.L. Telegdi, *Phys. Rev.* **105**, 1681 (1957).
- [10] J.L. Freidman and V.L. Telegdi, *Phys. Rev.* **106**, 1290 (1957).
- [11] E.C.G. Sudarshan and R.E. Marshak, *Phys. Rev.* **109**, 1860 (1958).
- [12] R.P. Feynman and M. Gell-Mann, *Phys. Rev.* **109**, 193 (1958).
- [13] S.L. Glashow, *Nucl. Phys.* **22**, 579 (1961); S. Weinberg, *Phys. Rev. Lett.* **19**, 1264 (1967); A. Salam, *Elementary Particle Theory; Relativistic Groups and Analyticity, Proceedings of the Eighth Nobel Symposium*, ed. N. Svartholm (Almqvist and Weksell, Stockholm, 1968).
- [14] F. Reines and C.L. Cowan, *Phys. Rev.*, **90**, 492 (1953).
- [15] F. Reines, C.L. Cowan, Jr., F.B. Harrison, A.D. McGuire and H.W. Kruse, *Phys. Rev.*, **117**, 159 (1960).
- [16] F. Reines and C.L. Cowan, *Physics Today*, **10**, 12 (1957).
- [17] M. Goldhaber, L. Grodzins and A. Sunyar, *Phys. Rev.*, **109**, 1015 (1958).
- [18] R.G.H. Robertson, T.J. Bowles, G.J. Stephenson, Jr., D.L. Wark, J.F. Wilkerson and D.A. Knapp, *Phys. Rev. Lett.*, **67**, 957 (1991).
- [19] V. M. Lobashev, *Progress in Particle and Nuclear Physics*, **40**, 337 (1998).
- [20] K. Hirata *et al.*, Kamiokande Collaboration, *Phys. Rev. Lett.*, **58**, 1490 (1987).
- [21] W. D. Arnett and J. L. Rosner, *Phys. Rev. Lett.*, **58**, 1906 (1987).

- [22] G.J. Feldman and R.D. Cousins, *Phys. Rev. D*, **57**, 3783 (1998).
- [23] A.P. French, *Newtonian Mechanics*, New York, W.W. Norton & Company, Inc., 1971.
- [24] Georg G. Raffelt, *Stars as Laboratories for Fundamental Physics*, Chicago & London: The University of Chicago Press, (1996).
- [25] J.V. Jelley, *Čerenkov Radiation and its applications*, New York: Pergamon Press, Inc., 1958.
- [26] R. Davis, Jr., *Phys. Rev. Lett.*, **12**, 303 (1964).
- [27] B.T. Cleveland, T. Daily, R. Davis, J.R. Distal, K. Lande, C.K. Lee, J. Ullman and P.S. Wildenhain, *Ap.J.*, **496**, 505 (1998).
- [28] P.A. Čerenkov, *Dokl. Akad. Nauk, SSSR*, **2**, 451 (1934).
- [29] P.A. Čerenkov, *Phys. Rev.*, **52**, 378 (1937).
- [30] I.M. Frank and Ig. Tamm, *Dokl. Akad. Nauk, SSSR*, **14**, 109 (1937).
- [31] K.S. Hirata *et al.*, Kamiokande Collaboration, *Phys. Rev. Lett.*, **65**, 1297 (1990); K.S. Hirata *et al.*, Kamiokande Collaboration, *Phys. Rev. D***44**, 2241 (1991), *Phys. Rev. D***45**, 2170E (1992).
- [32] Y. Fukuda *et al.*, Kamiokande Collaboration, *Phys. Rev. Lett.*, **77**, 1683 (1996).
- [33] Y. Fukuda *et al.*, Super-Kamiokande Collaboration, *Phys. Rev. Lett.*, **81**, 1158 (1998).
- [34] Y. Fukuda *et al.*, Super-Kamiokande Collaboration, *Phys. Rev. Lett.*, **82**, 2430 (1999).
- [35] J.N. Abdurashitov, *et al.*, SAGE Collaboration, *Physics Letters*, **B328**, 234 (1994). check
- [36] J.N. Abdurashitov, *et al.*, SAGE Collaboration, *Phys. Rev. Lett.*, **77**, 4708 (1996).
- [37] P. Anselmann *et al.*, Gallex Collaboration, *Physics Letters*, **B285**, 376 (1992).
- [38] P. Anselmann *et al.*, Gallex Collaboration, *Physics Letters*, **B342**, 440 (1995).
- [39] P. Anselmann *et al.*, Gallex Collaboration, *Physics Letters*, **B327**, 377 (1994).
- [40] J.N. Bahcall, *AstroPhys. J.*, **467**, 475 (1996).
- [41] E.G. Adelberger *et al.*, *Rev. Mod. Phys.*, **70**, 1265 (1998).
- [42] J.N. Bahcall, *Physics Letters*, **B436**, 243 (1998).

- [43] N. Hata and P. Langacker, *Phys. Rev. D* **52**, 420 (1995) .
- [44] Karsten M. Heeggar and R.G.H. Robertson, *Phys. Rev. Lett.*, **77**, 3720 (1996).
- [45] R. Ulrich, *AstroPhys. J.*, **162**, 993 (1970).
- [46] J.W. Leibacher and R.F. Stein, *Astrophysics Lett.*, **7**, 191 (1971).
- [47] C.L. Wolff, *AstroPhys. J.*, **177**, L87 (1972).
- [48] D.O. Gough, J.W. Leibacher, P.H. Scherrer and J. Toomre, *Science*, **272**, 1281 (1996).
- [49] W. Däppen, *Proceedings of International Astronomical Union Colloquium No. 147: The Equation of State in Astrophysics*, Edited by Gilles Chabrier and Evry Schatzman, Cambridge: Cambridge University Press, p. 368 (1994).
- [50] J. Harvey *et al.*, *Science*, **272**, 1284 (1996).
- [51] *The First Results from SOHO*, *Solar Physics*, **175**, (1999).
- [52] W.J. Chaplin, Y. Elsworth, R. Howe, G.R. Isaak, C.P. McLeod, B.A. Miller and R. New, *Mon. Not. R. Astr. Soc.*, **280**, 849 (1996).
- [53] E. Fosset, *Solar Physics*, **133**, 1 (1991).
- [54] C. Iglesias and F.J. Rogers, *AstroPhys. J.*, **464**, 943 (1996).
- [55] A.V. Gruzinov and J.N. Bahcall, *AstroPhys. J.*, **490**, 437 (1997).
- [56] B.W. Phillipone, A.J. Elwyn, C.N. Davids and D.D. Koetke, *Phys. Rev. Lett.*, **50**, 412 (1983).
- [57] B.W. Phillipone, A.J. Elwyn, C.N. Davids and D.D. Koetke, *Phys. Rev. C*, **28**, 2222 (1983).
- [58] B.W. Phillipone, A.J. Elwyn, C.N. Davids and D.D. Koetke, *Phys. Rev. C*, **25**, 2174 (1982).
- [59] M. Junker *et al.*, The LUNA Collaboration, *Phys. Rev. C*, **57**, 2700 (1998).
- [60] E. Anders and M. Grevasse, *Geochim. Cosmochin. Acta.*, **46**, 2363 (1989).
- [61] S.Y.F. Chu, L.P. Ekström and R.B. Firestone, *WWW Table of Radioactive Isotopes*, database version 2/28/99 from URL <http://nucleardata.nuclear.lu.se/toi/>.
- [62] G. Rech, Y.D. Chan, M.R. Dragowsky, R.-M. Larimer and E.B. Norman, *Phys. Rev. C*, submitted for publication (1999).
- [63] J.N. Bahcall, *Phys. Rev.*, **128**, 1297 (1962).

- [64] I. Iben, Jr., K. Kalata and J. Schwartz, *AstroPhys. J.*, **150**, 1001 (1967)/
- [65] R.P. Feynman, *Statistical Mechanics*, Reading, MA: Addison-Wesley, Chap. 2, 1990.
- [66] W.C. Haxton, *Annu. Rev. Astron. Astrophys.* **33**, 459 (1995).
- [67] B. Pontecorvo, *Zh. Eksp. Teor. Fiz.*, **33**, 549 (1957).
- [68] B. Pontecorvo, *Sov. Phys. JETP*, **6**, 429 (1958).
- [69] Chung Wook Kim and Aihud Pevsner, *Contemporary Concepts in Physics, Volume 8: Neutrinos in Physics and Astrophysics*, Chur, Switzerland: harwood academic publishers, p. 417, 1993.
- [70] B. Kayser, *Phys. Rev. D*, **24**, 110 (1981).
- [71] A. Acker, A.B. Balantekin and F. Loreti, *Phys. Rev. D*, **49**, 328 (1994). G.L. Fogli, E. Lisi and D. Montanino, *Phys. Rev. D*, **54**, 2048 (1996).
- [72] The NOMAD Collaboration, J. Altegoer *et al.*, *Physics Letters*, **B431**, 219 (1998).
- [73] John N. Bahcall, *Neutrino Astrophysics*, New York: Cambridge University Press, p. 258, 1989.
- [74] K. Grotz and H.V. Klapdor, *The Weak Interaction in Nuclear, Particle and Astrophysics*, Bristol, Philadelphia and New York: Adam Hilger, p. 304, 1990.
- [75] G.L. Fogli, E. Lisi and D. Montanino, *Phys. Rev. D* **49**, 3226 (1994).
- [76] P. Krastev and S.T. Petcov, *Phys. Rev. Lett.* **72**, 1960 (1994).
- [77] Y. Fukuda *et al.*, The Super-Kamiokande Collaboration, *Phys. Rev. Lett.*, **81**, 1562 (1998).
- [78] S.P. Mikheyev and A.Y. Smirnov, *Sov. J. Nucl. Phys.* **42**, 913 (1985).
- [79] L. Wolfenstein, *Phys. Rev. D* **17**, 2369 (1978).
- [80] J.N. Bahcall, S. Basu and M.H. Pinsonneault, *Physics Letters*, **B433**, 1 (1998).
- [81] The SNO Collaboration, *The Sudbury Neutrino Observatory*, *Nuclear Instruments & Methods in Nuclear and Particle Physics, Section A*, to be submitted for publication.
- [82] K.T. Lesko, *Project Notebook, Sudbury Neutrino Observatory*, Lawrence Berkeley National Laboratory, Rev. B (1998).
- [83] Hamamatsu Photonics, R1408 Technical Data Sheet, (October 1995).

- [84] C.J. Jillings, *A Photomultiplier Tube Evaluation System for the Sudbury Neutrino Observatory*, M.Sc. Thesis: Queen's University at Kingston, (1992).
- [85] W.R. Nelson, H. Hirayama, and D.W.O. Rogers, *The EGS4 Code System*, SLAC-265(1985).
- [86] E.W. Beier, D.F. Cowan, P.T. Kenner, J.R. Klein, F.M. Newcomer, D.S. McDonald, M. Neubauer, R. Van Berg, R.G. Van de Water and P. Wittich, SNO-STR-98-022, *Performance of the Electronics for the Sudbury Neutrino Observatory*, unpublished, 1998.
- [87] Richard James Ford, *Calibration of SNO for the Detection of ^8B Neutrinos*, Ph.D. Dissertation, Queen's University at Kingston, 1998. R. Ford, SNO-STR-96-055, *The nitrogen/dye laser calibration source*, unpublished, (1996).
- [88] D.S. McDonald, *Optical Calibration of the Sudbury Neutrino Observatory using a Sonoluminescence Device*, Ph.D. Dissertation, University of Pennsylvania, expected Fall 1999.
- [89] A. Schülke, K. Lesko, C. Okada, Y.D. Chan, SNO-STR-97-047, *Development of the LED optical calibration sources mounted on the PSUP*, unpublished, (1997).
- [90] M.C. Perillo Isaac, Y.D. Chan, D.L. Hurley, K.T. Lesko, M.E. Moorhead, E.B. Norman, A.R. Smith, D.L. Cluff, D. Hallman, J. Heise and P. Jagam, SNO internal report, SNO-STR-97-007, unpublished, 1997.
- [91] S.M. Brice, *Monte Carlo Analysis of the Sudbury Neutrino Observatory*, Ph.D. Thesis: Oxford University, (1995).
- [92] X. Chen, *Neural Network Analysis of Backgrounds in the Sudbury Neutrino Observatory*, Ph.D. Thesis: Oxford University, (1997).
- [93] H.H. Chen, *Phys. Rev. Lett.*, **55**, 1534 (1985).
- [94] N. Hata, UPR-0605T, unpublished (1994).
- [95] J.N. Bahcall and E. Lisi, *Phys. Rev.* **D54**, 5417 (1996).
- [96] M. Morehead and N. Tanner, *Proposed Procedure for Salt Purification*, SNO-STR-92-088, unpublished, 1992.
- [97] P.J. Doe, J.V. Germani, A.W.P. Poon, R.G.H. Robertson, T.D. Steiger, J.F. Wilkerson, T.J. Bowles, A. Hime, M.M. Fowler, P.M. Thornewell, J.B. Wilhemy and J.M. Wouters, *Construction of an Array of Neutral-Current Detectors for the Sudbury Neutrino Observatory*, SNO internal report, SNO-STR-95-023, unpublished (1995).
- [98] Christopher James Jillings, *The Elastic Scattering Reaction in the Sudbury Neutrino Observatory*, Ph.D. Thesis, Queen's University at Kingston, 1999.

- [99] J.J. Simpson and J.-X. Wang, *Determination of NC/CC Ratio and CC shape During the Pure D₂O Stage*, SNO internal report, SNO-STR-98-001, unpublished (1998).
- [100] J.J. Simpson and J.-X. Wang, *Determination of NC/CC Ratio and CC shape During the Pure D₂O Stage*, SNO internal report, SNO-STR-98-002 (Part II), unpublished (1998).
- [101] Alan Wing Pok Poon, *Energy Calibration of the Sudbury Neutrino Observatory using Monoenergetic Gamma-Ray Sources*, Ph.D. Thesis, University of British Columbia, 1998.
- [102] W. Frati, et. al., *Neutron Free Gamma Calibration Sources*, SNO-STR-92-032, unpublished (1992).
- [103] Sur, B., SNO-STR-93-041, ^{16,17}N : A Calibration Source for SNO, SNO-STR-93-041, unpublished (1992).
- [104] A. Hamer, *Energy Calibration of SNO for measurement of the Charged-Current Neutrino Reaction*, Ph.D. Thesis, Queen's University at Kingston, 1999.
- [105] Bicron Product Description, Appendix B, Premium Plastic Scintillators, Related Materials, Figure entitled *Range of Atomic Particles in Bicron Premium Plastic Scintillators*, p. B8.
- [106] K.I. Roulston and S.I.H. Naqvi, University of Manitoba, Winnipeg, Canada, *Bicron Product Description, (Appendix B: Premium Plastic Scintillators, Related Materials), Gamma-Detection Efficiency of Organic Phosphors*, p. B9.
- [107] C. Michael Lederer and Virginia S. Shirley, Eds., *Table of Isotopes, Seventh Edition*, New York: John Wiley & Sons, Inc. Appendix IV, Fig. 2a, (1978).
- [108] PAW – *Physics Analysis Workstation*, CERN Program Library Q121, 1997.
- [109] H.L. Anderson (Editor-in-Chief), *A Physicist's Desk Reference: The Second Edition of Physics Vade Mecum* Section 9.05.E, reference to Hubbell, Gimm and Overbø, *J. Phys. Chem. Ref. Data* **9**, 1023, (1980).
- [110] Storm and Israel, *Nuclear Data Tables*, **A**, 565 (1970).
- [111] Krane, Kenneth S., *Introductory Nuclear Physics*. New York: John Wiley & Sons, Inc., 1998.
- [112] Michael David Lay, *Creation and Detection of Čerenkov Light in the Sudbury Neutrino Observatory*, Ph.D. Thesis, Wolfson College, Oxford, 1994.
- [113] CRC Handbook of Chemistry and Physics, 52nd Edition, p. B-158.
- [114] J.G. Bellian and R.R. Dayton, *NaI(Tl) Scintillation Detectors*, Bicron Corporation, 1974.

- [115] E.B. Norman, private communication, June 1999.
- [116] Richard Firestone, *Table of Isotopes, Eighth Edition*, p. 21, New York: John Wiley & Sons, Inc., 1996.
- [117] E.B. Norman and B. Sur, *Phys. Rev. C*, **57**, 2043 (1998).
- [118] A.F. Sánchez-Reyes, M.I. Gebrián, J. Baró and J. Tehada, *Nucl. Instr. and Meth.*, **B28**, 123 (1987).
- [119] GEANT Monte Carlo Simulation, Center Experiment Radiologique Nucleair, 1985-1999.
- [120] *MCNP - A General Monte Carlo N-Particle Transport Code* Briesmeister, Judith F. (Ed.), Oak Ridge National Laboratory, LA-12625, March 1997.
- [121] E.B. Norman, I. Zliven, and R.M. Larimer, *Testing a Neutron-Activated NaI Detector as a Low-Energy Calibration Device for SNO*, SNO-STR-93-032, unpublished (1993).
- [122] *Starburst/CHAOS Operators Manual*, Lawrence Berkeley National Laboratory - Nuclear Science Division, unpublished.
- [123] E. Segre, *Nuclei and Particles*. New York: W.A. Benjamin, Inc., 1964.
- [124] Neutron News, Vol. 3, No. 3, pp 29-37, 1992 and <http://ne43.ne.uiuc.edu/n-scatter/n-lengths/>.

APPENDIX

Appendix: The Description of ^{16}N and NaI Sources in SNOMAN

The SNO Monte Carlo simulation (SNOMAN) propagates particles resulting from neutrino interactions in the detector across geometric boundaries between various detector elements. An embedding philosophy is followed to provide clear association of boundaries with geometry regions. For example, the acrylic vessel is described as a solid sphere in the geometry. The D_2O is described as another sphere embedded within the acrylic vessel. The D_2O boundaries are assigned a higher priority than the acrylic vessel boundaries. Generally, any particle that the Monte Carlo attempts to propagate through a boundary will always be handled using the routines for the higher priority region, in this case D_2O rather than the acrylic vessel. More than two regions sharing a common boundary are reliably described using this embedding scheme.

A.1 *The ^{16}N Source Chamber Geometry*

The major features listed below have been included in the Monte Carlo simulation, and are illustrated in Figure A.1. Nine detector elements are defined (the detector element media and numerical priority is presented following the region description):

- CAN – outer container (stainless steel; priority=540)
- RING – annulus which divides the interior of CAN (stainless steel; 541)
- OPT – optical coupling (acrylic; 550)
- GAP – lower chamber gap between CAN and SCINT (air; 543)
- SCINT – plastic scintillator (dark acrylic; 544)
- GAS – volume within scintillator (air; 545)

- INSTR – upper chamber volume (air; 543)
- PMT_E – exterior of PMT (aluminum; 544)
- PMT_I – interior of PMT (vacuum; 549)

The detector elements are embedded in the following manner. The outer container (CAN) has only the annulus (RING) as an interior region. There are three elements embedded within RING: the optical coupling (OPT), the lower chamber volume (GAP) and the instrumentation volume (INSTR). OPT is also embedded within INSTR and GAP to facilitate the handling of the common boundaries. The plastic scintillator (SCINT) is embedded within GAP, and the gas volume (GAS) is embedded within SCINT. Likewise, the exterior of the PMT (PMT_E) is embedded within INSTR and the interior of the PMT (PMT_I) within PMT_E.

The simulation of the source chamber is not complete to the level of including all the nuts and bolts. In fact, while all of the major features are present, there have been simplifications. The actual geometry of the region between the upper and lower chambers is quite complex. For example, the optical coupling is treated as a single, solid cylinder of acrylic, rather than the scheme featuring optical pads and acrylic detailed in Section 4.2. Indeed, mechanical fasteners, gas line couplings and the high-voltage converter have all been omitted. These components were judged to have minor influence on the attenuation of γ -rays escaping the lower chamber. In addition, simulations did not attempt to include the presence of the manipulator, nor any hardware necessary to couple the source chamber to the manipulator, unless specifically noted. The effect of such components on the ^{16}N Nhit spectrum will be studied in future simulations as the design of this hardware is finalized.

The source chamber geometry is intended to make use of all detector elements. If a simpler model of the source chamber is desired, one must work from the outside-in, beginning with CAN. Carefully refer to the description of the relationship between

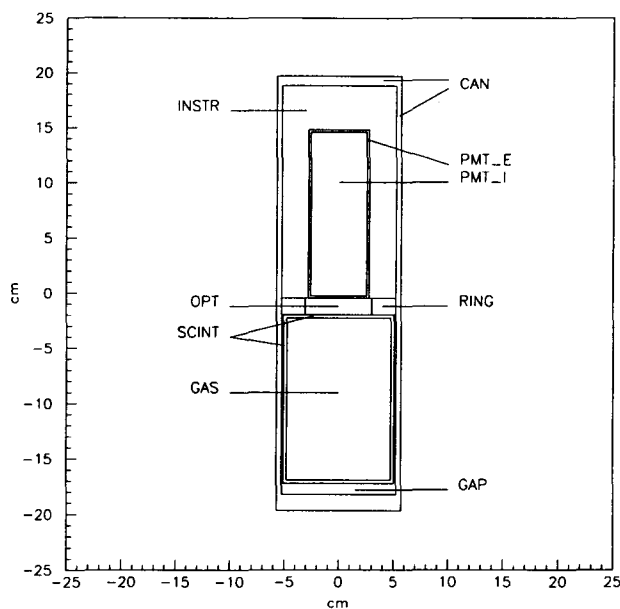


Figure A.1: The geometry regions of the ^{16}N source chamber.

embedded regions when choosing which to disable or enable. The effect of a specific region may also be investigated by setting the media to D_2O or to air, as one desires.

The ^{16}N source chamber geometry is compiled as part of the standard SNOMAN executable program, however, it is not a default feature in the geometry. A data file is read to activate the source chamber in the geometry. Additionally, the default detector element media, size and location are modified using one or more data files. The ^{16}N calibration command file (`calibration_16n.cmd`) has been modified to make the execution of these tasks convenient. A script has been added to the standard set of SNOMAN tools (`run_n16.scr`) to provide for position specification on the command line at the time of program execution.

A.2 Verification of the Geometry

The photon bomb feature of SNOMAN was used to verify that the geometry of the source chamber had been properly specified. This feature was used to generate 500 optical photons from points sampled throughout the source chamber geometry regions. The media for the nine detector elements were set to air and the photon bombs were detonated within each different region. The criteria for a successful geometry was that photons had to propagate through all regions and result in fewer than 1 in 100,000 errors causing an event to terminate. This result was achieved, and a plot mapping the source chamber is shown in Fig. A.2.

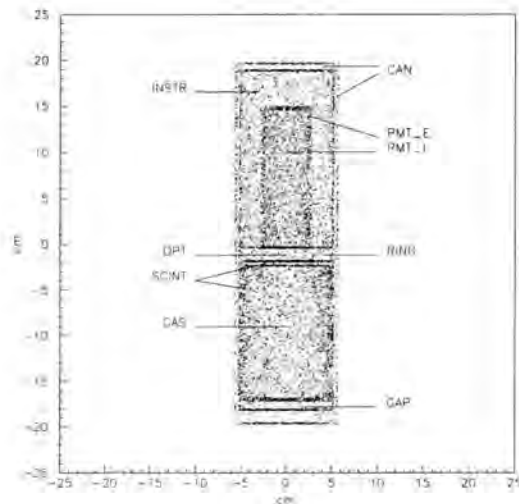


Figure A.2: The ^{16}N source chamber geometry, as illuminated by photon bombs from CAN, SCINT, RING and PMT_E. Each point represents an intersection of a photon propagation path and the boundary of a detector element. By setting all detector elements to air, SNOMAN propagates the photons in straight lines, but it keeps track of all boundary crossings. Plotting the boundary crossings provides a “photon map” of structures within SNO.

A.3 ^{24}Na Source Geometry

The code representing the ^{16}N source chamber required only minor modification to allow simulation of the ^{24}Na source. The primary change to SNOMAN was the inclusion of NaI as a valid media. This required a recompilation of the PEGS4_10.dat file, a data file used to specify media for the EGS4 lepton shower code. It was also necessary to modify the media.dat data file to accommodate the NaI media. The optical properties of NaI in this file are dummy values, borrowed from acrylic, since SNOMAN will have no cause to propagate Čerenkov photons through NaI.

The source consists of a thin cylinder of stainless steel enclosing a source volume, in which the NaI crystal is optically coupled to a PMT. Therefore, changes to or creation of new geometry files were avoided by making use of the structure of the ^{16}N decay chamber. A command file with nomenclature as follows is used to specify the ^{24}Na source geometry:

1. CAN again refers to the outer container of the source
2. RING denotes the interior space of the container
3. GAP represents the container of the NaI detector
4. SCINT is the area filled with NaI
5. INSTR remains the volume within which the PMT resides
6. PMT_E remains PMT_E and PMT_I remains PMT_I
7. GAS and OPT are not used.

The embedding geometry of SNOMAN for this source is as follows. The interior space (RING) is embedded within the exterior container (CAN). The interior is divided in two, with the upper area (INSTR) containing the PMT, which is divided into an

external (PMT_E) and internal region (PMT_I). The lower chamber contains the NaI detector, with no space allowed between the exterior of the NaI and the interior of the container exterior wall. Therefore GAP is used to represent the NaI exterior, while SCINT is used for the NaI interior. The geometry was verified to produce fewer than 1 in 100,000 geometry errors.

The radius and half-height of CAN, RING, GAP and SCINT are varied for each simulation. A wall thickness of 0.1 cm is used for CAN for all simulations. The exterior of the PMT is also taken to have a wall thickness of 0.1 cm. The INSTR and GAP detector elements completely overlap RING, therefore there is no net area for RING in this application. The RING detector element is necessary in this application because of the embedding geometry carried over from the ^{16}N source.